UPSCALING AND MULTISCALE RESERVOIR SIMULATION USING PRESSURE TRANSIENT CONCEPTS

A Dissertation

by

KRISHNA CHAITANYA NUNNA

Submitted to the Office of Graduate and Professional Studies of
Texas A&M University
in partial fulfillment of the requirements for the degree of

DOCTOR OF PHILOSOPHY

Chair of Committee, Michael J. King
Committee Members, Akhil Datta-Gupta
David Schechter
Yalchin Efendiev
Head of Department, Jeff Spath

May 2019

Major Subject: Petroleum Engineering

ABSTRACT

Fluid flow in subsurface petroleum reservoirs occurs on a wide range of length scales and capturing all the relevant scales in reservoir modeling is a cumbersome task. Even with the advent of modern computational resources, reservoir simulation of high resolution fine scale geologic models remain a challenge. Therefore, it is customary to use some kind of upscaling procedure to coarsen the multimillion cell geologic models to a scale feasible for practical reservoir simulation. Existing methods for upscaling of geologic models are based on steady state concepts of flow while the actual flow simulations itself is utilized for the purpose of capturing pressure and saturation transients. However, steady state or pseudo steady state limits may never be achieved for a coarse cell volume during a simulation time step in high contrast low permeability systems introducing a potentially significant bias into an upscaling or downscaling calculation. In this dissertation, a novel formulation is proposed which resolves these dynamic effects using an asymptotic pressure solution.

Three principal research contributions are made in this dissertation. First, a novel construction of transmissibility in 1D is derived using pseudo steady state concepts which has the advantage of localization over steady state methods, when applied for upscaling problems. This construction is general for all grid geometries usually utilized in industry standard reservoir simulation codes (block centered, radial, corner point). A new form of pressure averaging is proposed to effectively convert a 3D pseudo steady state upscaling into a 1D calculation. Second, a pressure transient diffuse source upscaling formulation is

introduced to identify well-connected sub volume that reaches pseudo steady state especially in high contrast systems. The formulation is based on transients approaching pseudo steady state in the upscaling region which can effectively identify the well-connected sub volume that contributes the flow. Third, the pressure transient diffuse source formulation developed for upscaling is extended to the multiscale framework where the large scale changes in pressure are resolved on the coarse grid while the saturations are resolved on the fine scale using downscaled coarse information. Applications are shown for both incompressible and slightly compressible flow.

ACKNOWLEDGEMENTS

First and foremost, I am indebted to my advisor Dr. Michael J. King for his academic guidance and financial support throughout my graduate school. During my stay at Texas A&M University, I learned a lot from him and have grown into appreciating his research insight even more as I complete my PhD. During my first year of working with Dr. King, I found myself struggling to follow and implement his ideas due to my limited knowledge on the subject matter. I found him to be extremely patient and he encouraged me through the process. His teachings have helped me develop a lot more confidence in my research and communication skills.

I also want to express my gratitude towards Dr. Akhil Datta-Gupta who was my motivation to join the MCERI research group. When I found myself at a crossroads towards the end of my Master's program, the support from him and my advisor steered me to pursue my PhD degree. I am grateful to my committee members Dr. David Schechter and Dr. Yalchin Efendiev for their insightful comments and encouragement, their prospective incented me to widen my research from various perspectives. I especially gained much needed mathematical insight into my research after discussions with Dr. Efendiev. I am also thankful to the helpful suggestions provided by Dr. Eduardo Gildin who served as a substitute in my final exam.

My sincere thanks to Dr. Robello Samuel from Halliburton, who was my mentor and supervisor during my first internship in the industry. He helped me gain a lot of practical insight to understand the industry which led to many opportunities coming my

way. I would also like to thank Dr. Sathish Sankaran, my internship supervisor at Anadarko Petroleum Corporation. Both my projects with him allowed me to experience and understand development aspects of unconventional reservoirs. His support and mentorship played a big role in my full time positon opportunity with Anadarko.

Thanks to all my colleagues from MCERI for their valuable and insightful participation in our research discussions. I especially would like to thank Chen Li who introduced me to a whole new side of Chinese cuisine and gave me good memories of college station.

I would like to thank my best buddy Jay Kumar Perneedi for being my emotional support through all ups and downs since my childhood. I would also like to thank a very special person in my life Neha Bansal. She was a constant source of support and encouragement through all the challenges in both my professional and personal life.

Last but not the least, I would like to thank my parents for their unconditional love all these years. They have been through a tough time during my graduate studies in the US and this accomplishment would not have been possible without their endless support.

CONTRIBUTORS AND FUNDING SOURCES

Contributors

This work was supervised by a dissertation committee consisting of Professors Michael J. King (advisor), Akhil Datta-Gupta, and David Schechter of the Department of Petroleum Engineering and Professor Yalchin Efendiev of the Department of Mathematics.

All the other work for the dissertation was completed independently by the student.

Funding Sources

This work was made possible by the financial support of Energi Simulation (formerly Foundation CMG) through the Texas A&M chair in Robust Reduced Complexity Modeling with Dr. Eduardo Gildin and the support of the members of the Model Calibration and Efficient Reservoir Imaging (MCERI) joint industry project at Texas A&M University.

TABLE OF CONTENTS

Page

LIST OF FIGURES

Page

LIST OF TABLES

Page

CHAPTER I

INTRODUCTION: UPSCALING

Reservoir simulation is a widely used tool for qualitative and quantitative forecast of fluid flow in subsurface formations. The simulation itself is made possible through the numerical solution of mass conservation equations in the form of partial differential equations. Fluid flow in subsurface petroleum reservoirs occurs on a wide range of length scales from micrometer pore scale to macro reservoir scale (Dagan 2012). Capturing all the relevant scales in the macro scale reservoir modeling is a cumbersome task and is usually limited by the availability of computational resources. Building geologic models with millions of grid blocks is a commonplace in the oil and gas industry. Even with the advent of modern computational technology, reservoir simulation of these fine scale geologic models remain a challenge especially with the industry moving towards scholastic workflows to quantify the uncertainty in performance predictions. The stochastic workflows require simulations of multiple realizations of reservoir models which adds significant computational overhead. Therefore, it is customary to use some kind of upscaling procedure to coarsen the high resolution geologic models to a scale feasible for practical reservoir simulation. While quantities like porosity and geometry which are additive, may be upscaled using simple volume weighted averages, upscaling of permeability which is an intrinsic property or transmissibility which includes the permeability as well as the geometry, requires some care. Upscaling techniques may be

classified into single phase and multi-phase methods. The focus of this dissertation is on single phase upscaling methods.

There are number of upscaling methods for permeability (or transmissibility) proposed in the literature ranging from simple analytical averaging methods (Deutsch 1989,King 1989) to advanced flow based upscaling methods (Chen et al. 2003, King and Mansfield 1999). It is well documented in the literature that flow based upscaling methods tend to give better coarse scale descriptions than their analytical counterparts (see Durlofsky and Chung 1990,Christie 1996, Farmer 2002). In flow based upscaling methods, a single phase elliptical partial differential equation (Eq.(1.1)) is solved with a specified set of boundary conditions over the domain Ω to obtain an effective permeability or transmissibility. In Eq.(1.1), $\vec{\vec{k}}$ is the permeability tensor, μ is the fluid viscosity, $p, \vec{u}$ refer to the fluid pressure and Darcy velocity respectively.

$$\nabla \cdot \vec{u} = 0 \text{ where } \vec{u} = -\frac{1}{\mu}\vec{\vec{k}} \cdot \nabla p \tag{1.1}$$

King et al. 1998, Lunati et al. 2001 and Chen et al. 2003 have documented that upscaling for transmissibility being a high resolution property compared to permeability honors the fine scale connectivity information better than the cell based permeability upscaling methods. This is hardly a coincidence since flow simulation eventually relies on inter-cell transmissibilities rather than cell permeabilities to solve for pressure. Since Eq. (1.1) is incompressible, artificial boundary conditions are imposed over Ω to induce flow. Depending on where the boundary conditions are imposed over Ω, the single phase flow

based upscaling methods may be further classified into local, extended local, global, local-global upscaling methods.

1.1 Local Upscaling Methods

In the local upscaling methods, the size of the computational region Ω is restricted to the coarse cell(s) for which the effective property is to be evaluated. The most common type of local upscaling method is illustrated in Figure 1.1 which mimics the laboratory scale core flood permeability measurement experiment with pressure isobars at the inlet and outlet face and no flow side boundary conditions. This type of boundary conditions were first proposed by Warren and Price 1961 and by making the side boundary conditions no flow, crossflow terms are neglected. This calculation is repeated in three principal directions to obtain a diagonal permeability or transmissibility using volumetric pressure averaging of Darcy's equation as shown in Eq. (1.2) for permeability upscaling over domain Ω.

$$\iiint_{\Omega} d^3x \cdot (\vec{u}) = -\frac{1}{\mu} \vec{\vec{k}}^{Eff} \cdot \oiint_{\partial\Omega} d^2x \cdot (\hat{n}p) \tag{1.2}$$

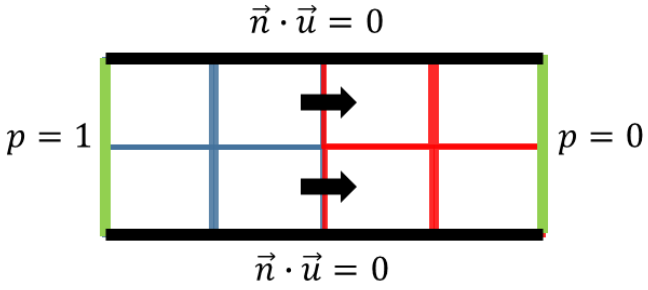

Figure 1.1: Local steady state upscaling with no flow side boundary conditions

Sealed side boundary conditions are strictly valid only when the flow units are mirror images of each other (symmetric) which puts a severe restriction of the general applicability of the boundary conditions to various reservoir models. As noted by Cardwell and Parsons 1945, the use of pressure isobars will bias the answers upwards while the use of sealed side boundaries will bias the results downwards. Whether one bias will dominate the other depends on the geologic environment. Usually, sealed side boundary conditions preserve barriers. However, the whole "core-flood" boundary conditions systematically expand barrier and reduce the continuity of pay (King 2007). Alternatives to sealed side boundary conditions were proposed in the literature, namely linear pressure boundary conditions (Guerillot et al. 1990) and periodic boundary conditions (Durlofsky and Chung 1990). These boundary conditions allow calculation of a full permeability tensor for upscaled models. In linear pressure boundary conditions (Figure 1.2), the pressure gradient still remains constant as is the case with no flow. However, fluid is allowed to leave or enter at any point on the transverse sides of the coarse block. Durlofsky and Chung 1990 and Durlofsky 1991 documented that linear pressure side boundary conditions tend to bias the upscaled permeability (or transmissibility) upwards. They proposed the use of periodic

boundary conditions with imposed flux conservation (Figure 1.3). A variant of this was also proposed by Bøe 1994 which uses a weak formulation of Darcy's law to derive a symmetric and positive definite permeability tensor.

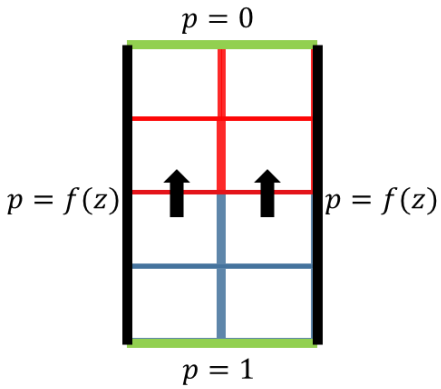

Figure 1.2: Local upscaling in vertical direction with linear side boundary conditions

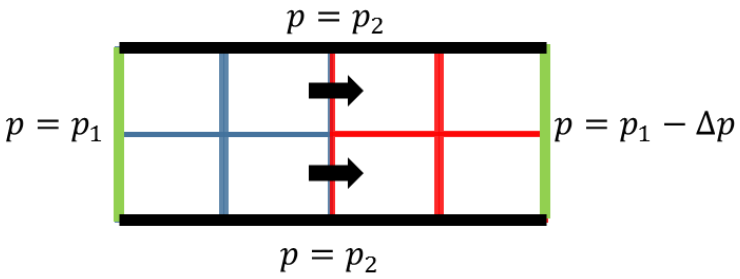

Figure 1.3: Local upscaling with periodic boundary conditions

The use of periodic boundary conditions results in effective permeability greater than or equal to no flow side boundary conditions and always less than linear pressure boundary conditions. Periodic boundary conditions are strictly valid when the coarse volumes are periodic i.e., fine scale heterogeneity in each coarse block must be identical.

Unfortunately the reservoir rocks are seldom periodic. It is clear from the above discussion is that the upscaled effective permeability (or transmissibility) is sensitive to the choice of boundary conditions. This is referred to as the localization effect. To reduce the dependence on local boundary conditions, extended local methods were proposed which will be discussed in the following section.

1.2 Extended Local Upscaling Methods

In extended local methods, the size of the computation region is expanded beyond the coarse blocks by adding a buffer region or skin, and boundary conditions are imposed on the extended domain (Holden and Lia 1992;Gomez-Hernandez and Journel 1994; Hou and Wu 1997; Wu et al. 2002). The extent of the border regions and their effectiveness depends on the geologic environment. For instance Wen et al. 2003 reported very little improvement by using two coarse rings as the skin region compared to one coarse ring. Figure 1.4 shows the set up for extended local upscaling with "core-flood" boundary conditions imposed one coarse ring as skin region. After solving Eq. (1.1) on the extended domain, pressure averaging is performed in the coarse cell(s) of interest to obtain an effective property.

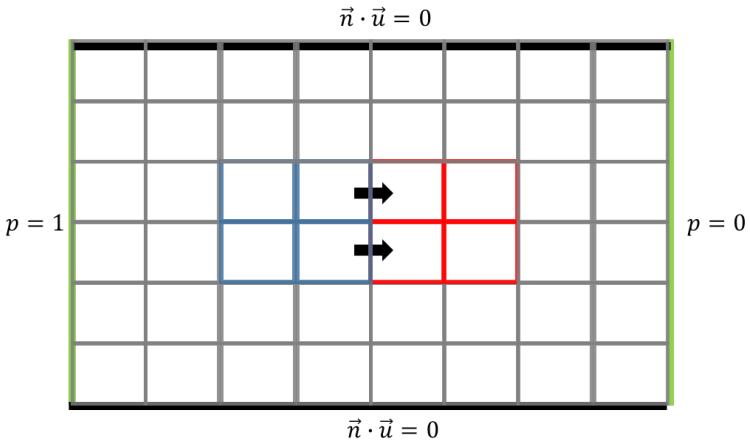

Figure 1.4: Extended local upscaling with no flow side boundary conditions

1.3 Global Upscaling Methods

In global upscaling, the fine scale solution is solved using a specified set of global boundary conditions (e.g. wells) and the upscaled property is evaluated based on the fine scale solution (White and Horne 1987, Holden and Nielsen 2000). Global upscaling methods mostly apply to transmissibility upscaling where the coarse transmissibilities are obtained using the coarse face flux and the bulk volume averaged pressure differences. Once the initial coarse transmissibilities are computed, iterative procedure may be required to remove any negative transmissibilities to a point where both fine and coarse solutions are in agreement. Although very expensive, global upscaling methods can provide accurate coarse scale descriptions. However, once the global boundary conditions change, the same coarse description may not be accurate. So, these techniques rely heavily on the knowledge of the global boundary conditions.

1.4 Coupled Local-Global (Quasi Global) Upscaling Methods

Local-global methods are developed as an intermediary between extended local and global upscaling methods (Chen et al. 2003). These methods take advantage of the global boundary conditions but always solve the global problem on the coarse scale instead of fine scale which significantly reduces the computational overhead. An iterative procedure is employed to derive the boundary conditions for the extended local upscaling problems and effective permeabilities or transmissibilities are evaluated based on the derived boundary conditions. Figure 1.5 shows the set up for local-global transmissibility upscaling with global coarse pressures. These pressure are interpolated on the fine scale resolution and used as boundary conditions to solve for flow at the coarse face of interest. The effective transmissibility is evaluated using Eq.(1.3) where the denominator is the bulk volume averaged pressure differences for the coarse blocks of interest.

$$T^{Eff} = \frac{\mu q_{face}}{\langle p \rangle_{upstream} - \langle p \rangle_{downstream}} \tag{1.3}$$

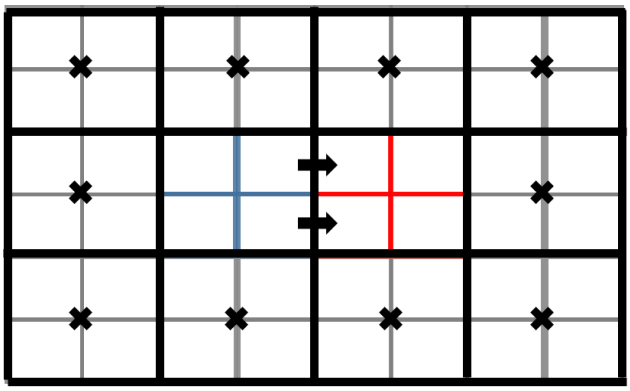

Figure 1.5: Coupled local global upscaling procedure showing global coarse pressures used to solve for flow at the coarse face

The convergence criteria for the iterations is established based on a predefined tolerance for flux and pressure residual between successive iterations. Areas with very low flow are avoided in the iterations to avoid negative transmissibilities. This version was named adaptive local global upscaling (Chen and Durlofsky 2006). Local-global upscaling was successfully tested on many cases with some variations (see Efendiev and Durlofsky 2004;Wen et al. 2006; Alpak et al. 2012 and Alpak 2015). One drawback of the method seems to be the reliance on the knowledge of global boundary conditions. Upscaling of geologic models is typically performed early in the life of a reservoir where there is no access to dynamic well data. In fact, it is performed as a precursor to the future well planning. Therefore, optimizing an upscaling calculation to a specified set of global boundary conditions may not be robust (Fincham et al. 2004).

1.5 Near Well Upscaling Methods

The local and extended local upscaling methods described above are based on the assumption of linear pressure field (constant pressure gradient) for the specified pressure isobars as boundary conditions to drive the local flow. However, the pressure gradients are no longer uniform in the presence of wells. King 2007 proposed a simple algebraic well index calculation using analytic upscaled permeability calculation. Ding 1995 first introduced a near well upscaling procedure using global boundary conditions. Durlofsky et al. 2000 introduced the extended local flow based near well upscaling procedure where uniform pressure boundary conditions are imposed on an extended domain over the coarse block where the well resides. As shown in Figure 1.6, the well and boundary pressures are imposed to be 1 and 0 respectively. Flow from well to the well cell is handled using Peaceman equivalent radius (Peaceman 1978, 1983, 1990). The upscaled well index after solving Eq.(1.1) over Ω is given by Eq. (1.4) where the denominator is difference between well bottomhole pressure and the bulk volume averaged coarse block pressure. The neighboring well block transmissibilities are also adjusted using the obtained pressure field using Eq.(1.3).

$$WI^{Eff} = \frac{\mu q_{well}}{p_{wf} - \langle p \rangle_{coarseblock}} \tag{1.4}$$

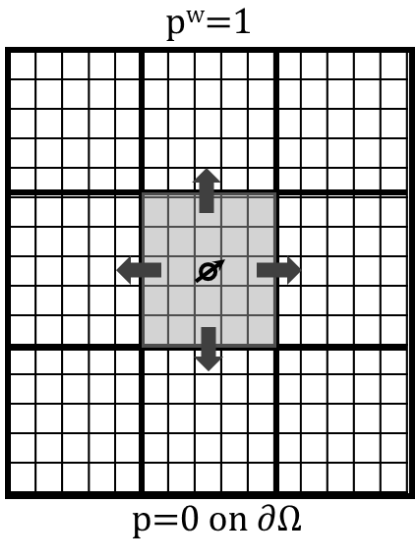

Figure 1.6: Near well upscaling procedure (After Durlofsky et al. 2000)

1.6 Steady State Upscaling: Issues

The recurring issue from the above discussion on steady state upscaling is the impact of local boundary conditions on the upscaled answers. The focus of this dissertation is entirely on improvement of local upscaling methods. Therefore, issues related to the same are discussed henceforth. Figure 1.7 describes three scenarios for a flow at a coarse cell pair with different upstream and downstream boundary conditions. Although, they may have the same face flux, the reference pressure drops for the calculation of transmissibility are different leading to different transmissibilities for the three cases. Steady state upscaling is therefore implicitly coupled to the large scale global boundary conditions. While the quasi global and global upscaling techniques can accurately capture the cross flow terms (transverse pressure gradients) for a specified global scenario, the knowledge of large scale boundary conditions may not be readily available especially early

in the life cycle of a field where upscaling is typically performed in the reservoir modeling workflow (Fincham et al. 2004).

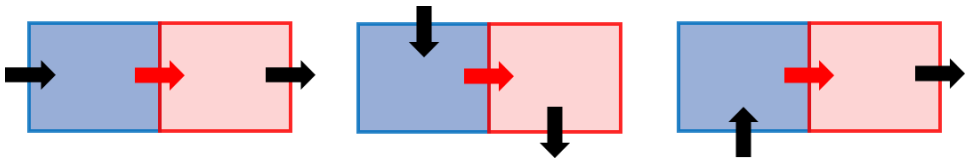

Figure 1.7: Localization issue in steady state local upscaling

King 2007 proposed apriori upscaling errors to determine the quality of an upscaling calculation before performing it (Table 1.1). As per the author, the leading order error for an upscaling calculation is the assumption of pressure equilibrium within a coarse volume which is violated in the presence of disconnected or weakly connected pay. Capturing the reservoir connectivity is important for a local upscaling calculation in order to accurately capture the fine scale flow behavior on the coarser scale. This is particularly important in high contrast systems where the pressure takes a long time to equilibrate in the low permeability volumes. Moreover, the reservoirs themselves have changed in the recent times with new plays in unconventional shale oil/gas in extremely low permeability rock. This change in fundamental mechanisms challenges the historical modeling approaches based upon steady state concepts. New gridding techniques are being proposed to simulate the hydraulic as well as natural fractures (Sun and Schechter 2015).

The second assumption in Table 1.1 relates to the assumption of uniform flux in the direction of flow for two-point steady state upscaling. In the presence of strong cross flow, the upscaled answers may be less accurate for a local steady state upscaling. A local-

global upscaling or multi-point stencil may be required in such cases. However, most of the standard industry tools are built on standard two point flux approximations due to the expensive nature of multi point stencils. While the first two errors in Table 1.1 focus on single phase upscaling errors, the third point explains the multiphase flow errors while coarsening. In the presence of highly correlated heterogeneities, even if there is a perfect single phase upscaling that captures the total velocity, the phase velocities may not be accurate which will be apparent in the frontal advance. In such cases, it is worthwhile considering multiphase upscaling like pseudoization (King and Mansfield 1999;Alpak 2015) or perform multiscale simulation instead so that the multiphase errors are resolved on the fine scale using downscaled pressure and velocities. The third assumption relates to multiphase effects while coarsening which will be discussed in the multiscale simulation section of this dissertation.

Assumption	**Source of Error (Missing Physics)**
Pressure equilibrium within the coarse cell	Disconnected or weakly connected pay within the coarse cell will not be in equilibrium
Fluid velocity is parallel to the pressure drop	Flow may depend on the transverse pressure drop on the coarse grid
Single velocity within a coarse cell	Distribution of multiphase frontal velocities replaced by a single value

Table 1.1: Apriori upscaling errors (King 2007)

1.7 Research Objectives: Upscaling

The motive of this research is to expand upon the current state of the art in local upscaling methods using pressure transient concepts. In the current work, instead of expanding the computational domain to reduce the dependence on the local boundary conditions, we work backwards from the flowing face by setting up a local flow field using source terms derived from pseudo steady state concepts. The upscaling formulation is derived from pseudo steady state concepts (PSS) which removes the explicit dependence of local boundary conditions in a way steady state upscaling does not.

The upscaling work of this dissertation is divided into three main chapters. In chapter two, standard expressions for transmissibility are derived in 1D using a generalized construction. Then, a rigorous relationship is derived in 1D between pore volume averaged steady state pressure drop and the total pseudo steady state pressure drop which is utilized to define transmissibility using pseudo steady state concepts. Extension of the 1D construction to 3D is presented using a novel pressure averaging approach and advantages of using PSS concepts to upscaling are highlighted.

In chapter three, two variations of a local upscaling formulation based on PSS flow is presented. While one formulation is completely localized, the other one is weakly coupled to the upstream and downstream faces. The weakly coupled method is based on a variational formulation which has zero total flux at the inlet and outlet boundaries having a leaky flux at the fine scale resolution. Applications of the PSS upscaling formulations are shown for SPE10 (Christie and Blunt 2001) and an onshore tight gas reservoir model.

In chapter four, a pressure transient diffuse source (DS) upscaling formulation is presented which is an extension of PSS concepts to transient systems. A brief background on the existing literature is reviewed which is required for the development of the diffuse source upscaling approach. Advantages of the proposed formulation for applicability in high contrast systems is highlighted. Applications are shown for 3D SPE10 and tight gas reservoir models. The approach is benchmarked against extended local and local-global upscaling approach in a series of 2D localization tests. Extension of the DS formulation to faulted grids is also shown.

Finally in chapter five, the upscaling work is summarized with key findings from chapter two to five and possible aspects of further research are also highlighted.

CHAPTER II

STEADY STATE AND PSEUDO STEADY STATE TRANSMISSIBILITY

2.1 Introduction

Transmissibility is used to relate pressure drop to fluid flux in flow simulators. It is usually described using steady state (SS) concepts, although its application in flow simulation is to a sequence of pseudo steady state flow calculations. Here, transmissibility is defined using both steady state and pseudo steady state flow concepts in 1D and the conceptual advantages of using pseudo steady state when developing upscaling algorithms is highlighted. A novel pressure averaging procedure is introduced to turn the 1D construction into a 3D PSS transmissibility.

2.2 1D Transmissibility

The 3D diffusivity equation for slightly compressible single phase flow in the absence of gravity and external sources is given by Eq.(2.1). The porosity (ϕ) and permeability (k) are functions of position. Total compressibility $\left(c_t\right)$ and fluid viscosity (μ) are treated as constants. For multiphase flow, the inverse of viscosity will be replaced by the total mobility, $1/\mu = k_{rw}/\mu_w + k_{ro}/\mu_o$ (water-oil example). However, the transmissibility itself will still follow the current construction.

$$\phi c_t \frac{\partial p}{\partial t} + \nabla \cdot \vec{u} = 0 \text{ where } \vec{u} = -\frac{1}{\mu} \vec{\vec{k}} \cdot \nabla p \tag{2.1}$$

For finite difference and finite volume applications, the diffusivity equation is integrated over the domain of each grid block Ω (Rozon 1989). Applying divergence theorem to Eq.(2.1) gives Eq.(2.2) which shows the cell pressure in the discretized equations is the pore volume averaged pressure ($\int_{\Omega} d^3x(\phi p)$) and the flux across the boundaries of each cell $(\vec{n}\cdot\vec{u})$ is expressed with respect to the differences between pore volume averaged pressures. This is the reference pressure drop for the definition of transmissibility although most of the upscaling literature reports the transmissibility evaluation using bulk volume averaged pressures. This is due to the fact that porosity never shows up in the equations when working with purely incompressible steady state flow.

$$c_t \frac{\partial}{\partial t}\int_{\Omega} d^3x(\phi p) + \oint_{\partial\Omega} d^2x(\hat{n}\cdot\vec{u}) = 0 \tag{2.2}$$

Now, pressure solutions in 1D are reviewed for defining and evaluating the two-point expression for transmissibility. The 1D diffusivity equation for slightly compressible flow can be expressed in terms of the cross sectional area ($A(x)$) and the Darcy flux (q) given by Eq.(2.3).

$$\phi A(x) c_t \frac{\partial p}{\partial t} + \frac{\partial q}{\partial x} = 0 \text{ where } q = -\frac{kA(x)}{\mu}\frac{\partial p}{\partial x} \tag{2.3}$$

The Darcy flux ($q(x)$) may be integrated to obtain the pressure profile for both steady state and pseudo steady state (Eq.(2.4)).

$$\frac{\Delta p}{\mu} = \int dx \frac{q}{kA(x)} \tag{2.4}$$

The steady state pressure drop over an interval from x_1 to x_2 given a uniform flux q_f is given in Eq.(2.5).

$$\Delta p_{SS} = \mu q_f \int \frac{dx}{kA(x)} \tag{2.5}$$

If this interval corresponds to a cell with cell faces at x_1 and x_2, then this provides the definition of the cell transmissibility in terms of the normalized pressure drop.

$$\frac{1}{T^{Cell}} \equiv \frac{\Delta p_{SS}}{\mu q_f} = \int_{x_1}^{x_2} \frac{dx}{k(x)A(x)} \tag{2.6}$$

Here, the permeability and the cross-sectional area may both be functions of position. The cell transmissibility is not directly used in flow simulation. Instead the intercell transmissibility is used which references to the pressure difference between the pore volume weighted average cell pressures in adjacent cells. As an intermediate step, the pressure difference between the face pressures and the pore volume weighted cell pressure is calculated, which define the half cell transmissibilities. This average pressure is obtained from the pressure profile that interpolates between the pressure values of p_1 and p_2 at x_1 and x_2, respectively. For steady state flow:

$$p_{SS}(x) = \left(p_1 \cdot \int_{x'=x}^{x_2} \frac{dx'}{k(x')A(x')} + p_2 \cdot \int_{x'=x_1}^{x} \frac{dx'}{k(x')A(x')} \right) \Bigg/ \int_{x_1}^{x_2} \frac{dx}{k(x)A(x)} \tag{2.7}$$

The pore volume weighted average pressure is:

$$\bar{p}_{SS} = \frac{\int_{x_1}^{x_2} dx\phi(x)A(x)p_{SS}(x)}{\int_{x_1}^{x_2} dx\phi(x)A(x)}$$

$$\bar{p}_{SS} = \frac{\int_{x_1}^{x_2} dx\phi(x)A(x)\left(p_1 \cdot \int_{x'=x}^{x_2} \frac{dx'}{k(x')A(x')} + p_2 \cdot \int_{x'=x_1}^{x} \frac{dx'}{k(x')A(x')} \right)}{\left(\int_{x_1}^{x_2} dx\phi(x)A(x) \right) \cdot \left(\int_{x_1}^{x_2} \frac{dx}{k(x)A(x)} \right)} \tag{2.8}$$

The half cell transmisisbilities are defined using the pressure difference between $\bar{p}_{SS}$ and each face pressure.

$$\begin{aligned} \frac{1}{T_1^{Half}} &\equiv \frac{p_1 - \bar{p}_{SS}}{\mu q_f} = \int_{x_1}^{x_2} dx\phi(x)A(x) \int_{x'=x_1}^{x} \frac{dx'}{k(x')A(x')} \Big/ \int_{x_1}^{x_2} dx\phi(x)A(x) \\ \frac{1}{T_2^{Half}} &\equiv \frac{\bar{p}_{SS} - p_2}{\mu q_f} = \int_{x_1}^{x_2} dx\phi(x)A(x) \int_{x'=x}^{x_2} \frac{dx'}{k(x')A(x')} \Big/ \int_{x_1}^{x_2} dx\phi(x)A(x) \end{aligned} \tag{2.9}$$

The sum of the reciprocal of the half cell transmissibilites gives back the cell transmissibility (Eq.(2.6)). In contrast, the sum of the reciprocal of the half cell transmisisbilities for a pair of adjacent cells yields the expression for intercell transmissibility where the shared face pressure cancels out (Eq.(2.10)). Here the left (upstream) cell extends from x_{i-1} to x_i and the right (downstream) cell from x_i to x_{i+1}.

$$\frac{1}{T} \equiv \frac{\bar{p}_{SS}^{Left} - \bar{p}_{SS}^{Right}}{\mu q_f}$$

$$\frac{1}{T} = \frac{\int_{x_{i-1}}^{x_i} dx\phi(x)A(x) \int_{x'=x}^{x_i} \frac{dx'}{k(x')A(x')}}{\int_{x_{i-1}}^{x_i} dx\phi(x)A(x)} + \frac{\int_{x_i}^{x_{i+1}} dx\phi(x)A(x) \int_{x'=x_i}^{x} \frac{dx'}{k(x')A(x')}}{\int_{x_i}^{x_{i+1}} dx\phi(x)A(x)} \tag{2.10}$$

The PSS flux solution follows the 1D form of the diffusivity equation when $\partial p / \partial t$ is uniform in the volume. Therefore, PSS flux varies linearly with pore volume.

$$q_{1,PSS}(x) = q_{f1}\left(\int_{x'=x}^{x_2} dx'\phi(x')A(x') \Big/ \int_{x_1}^{x_2} dx\phi(x)A(x)\right)$$
$$q_{2,PSS}(x) = q_{f2}\left(\int_{x'=x_1}^{x} dx'\phi(x')A(x') \Big/ \int_{x_1}^{x_2} dx\phi(x)A(x)\right) \tag{2.11}$$

Here, the PSS flux is expressed in terms of the flux for each cell face, q_{f1} or q_{f2}. The PSS pressure drops may be obtained by substituting the above PSS flux in Eq. (2.4) and setting the limits from x_1 to x_2 (Eq.(2.12)).

$$\frac{\Delta p_{1,PSS}(x)}{\mu q_{f1}} = \frac{1}{q_{f1}}\int_{x_1}^{x_2} dx \frac{q_{1,PSS}(x)}{k(x)A(x)} = \frac{\int_{x_1}^{x_2} \frac{dx}{k(x)A(x)} \int_{x'=x}^{x_2} dx'\phi(x')A(x')}{\int_{x_1}^{x_2} dx\phi(x)A(x)}$$
$$\frac{\Delta p_{2,PSS}(x)}{\mu q_{f2}} = \frac{1}{q_{f2}}\int_{x_1}^{x_2} dx \frac{q_{2,PSS}(x)}{k(x)A(x)} = \frac{\int_{x_1}^{x_2} \frac{dx}{k(x)A(x)} \int_{x'=x_1}^{x} dx'\phi(x')A(x')}{\int_{x_1}^{x_2} dx\phi(x)A(x)} \tag{2.12}$$

After integration by parts, Eq. (2.12) and Eq.(2.9) come out be equivalent giving a relationship between half cell transmissibilities and the pseudo steady state pressure solutions. The equivalence relationships is that the pore volume average SS pressure drop is equal to the total PSS pressure drop across the volume.

$$\Delta p_{PSS} = \Delta \bar{p}_{SS} \tag{2.13}$$

The intercell transmissibility can now be expressed in terms of normalized sum of PSS pressure drops with q_f being flux across the shared face (face 2 of the left cell and face 1 of the right cell).

$$\frac{1}{T} = \frac{\Delta p_{PSS}^{Left} + \Delta p_{PSS}^{Right}}{\mu q_f} = \frac{1}{q_f}\left[\int_{x_{i-1}}^{x_i} dx \frac{q_{2,PSS}(x)}{k(x)A(x)} + \int_{x_i}^{x_{i+1}} dx \frac{q_{1,PSS}(x)}{k(x)A(x)} \right] \tag{2.14}$$

Notice the largest contribution to the pressure gradient within the integrals of Eq.(2.14) is at the flowing face, where the pressure gradients are identical to the SS solution. At the far cell faces, the normalized flux and the PSS pressure gradient both vanish. Although these two approaches (SS and PSS) have been shown to be equivalent in 1D, they will differ in multiple dimensions. In the context of an upscaling calculation, the advantage of using a PSS approach is highlighted further down the text.

Now, a simple 1D block centered cell pair example (Figure 2.1) is considered to demonstrate the relationship between the SS and PSS solutions. In Figure 2.1, A_1, A_2 refer to the cross sectional areas, $\Delta x_1, \Delta x_2$ are the respective lengths of the upstream and downstream blocks and q_f is the flux across the shared face.

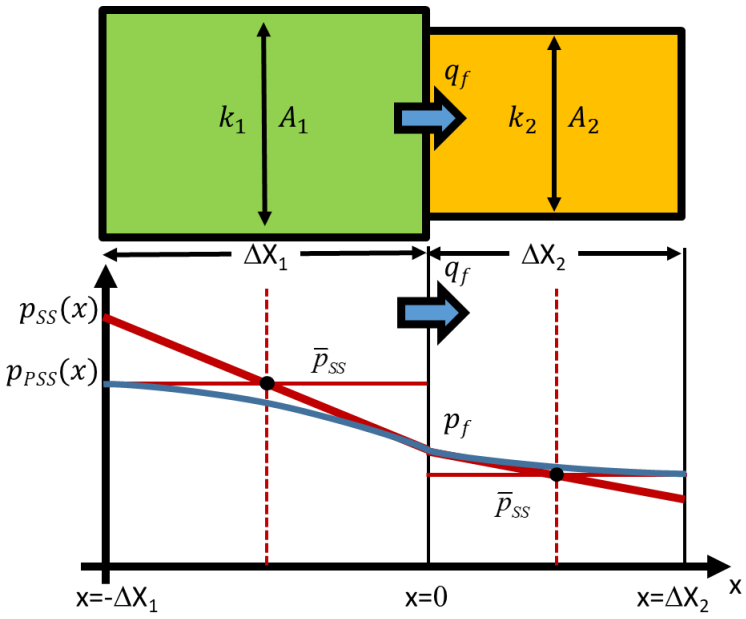

Figure 2.1: Steady state and Pseudo Steady State pressure profiles for a 1D Block centered cell pair

The steady state pressure profile is a piecewise linear function of position. The steady state pressure profile and average pressure in each cell are expressed in terms of the face flux and the face pressure.

$$p_{SS}(x) = p_f - \frac{\mu q_f}{k_i A_i} \cdot x \tag{2.15}$$

$$\bar{p}_{SS} = p_f - \frac{1}{2}\frac{\mu q_f}{k_i A_i} \cdot (\mp \Delta x_i) \tag{2.16}$$

The intercell transmissibility for the cell pair is now given by the difference of the pore volume averaged SS pressure drops (Eq.(2.17)).

$$\frac{1}{T} \equiv \frac{\bar{p}_{SS}^{Left} - \bar{p}_{SS}^{Right}}{\mu q_f} = \frac{1}{2}\frac{\Delta x_1}{k_1 A_1} + \frac{1}{2}\frac{\Delta x_2}{k_2 A_2} \tag{2.17}$$

The steady state pressure profile and the volume weighted steady state cell pressure may also be used to define the "pressure equivalent" position of the cell center, x_c in 1D (Pedrosa and Aziz 1986). This cell center may be used to develop a finite difference formulation for the transmissibility based upon the pressure at x_c.

$$p_{SS}\left(x_c\right) \equiv \bar{p}_{SS} \tag{2.18}$$

This is a general definition that may be used for arbitrary cells. For block centered cells, the pressure equivalent center is at the centroid of the cell, $x_c = \mp\frac{1}{2}\Delta x_i$. This equivalence with the centroid is true of all simplexes (this 1D example, 2D triangular elements, 3D tetrahedral elements) but need not be true in general, as will be shown for radial elements, below.

For PSS flow, the flux varies linearly within each block which gives a quadratic solution for the pressure profile.

$$\begin{aligned} q_{PSS}\left(x\right) &= q_f \cdot \left(1 \pm \frac{x}{\Delta x_i}\right) \\ p_{PSS}\left(x\right) &= p_f - \frac{\mu q_f}{k_i A_i} \cdot \left(x \pm \frac{x^2}{2\Delta x_i}\right) \end{aligned} \tag{2.19}$$

$$\begin{aligned} \Delta p_{PSS}^{Left} &= p_{PSS}\left(-\Delta x_1\right) - p_f = \frac{\mu q_f}{k_1 A_1} \cdot \frac{\Delta x_1}{2} \\ \Delta p_{PSS}^{Right} &= p_f - p_{PSS}\left(\Delta x_2\right) = \frac{\mu q_f}{k_2 A_2} \cdot \frac{\Delta x_2}{2} \end{aligned} \tag{2.20}$$

The PSS pressure drop across the cell gives the same result for the intercell transmissibility as expected (Eq.(2.21)). Notice the PSS flux profile (Eq.(2.19)) naturally follows the finite element RT0 basis function (Raviart and Thomas 1977).

$$\frac{1}{T} \equiv \frac{\Delta p_{PSS}^{Left} + \Delta p_{PSS}^{Right}}{\mu q_f} = \frac{1}{2}\frac{\Delta x_1}{k_1 A_1} + \frac{1}{2}\frac{\Delta x_2}{k_2 A_2} \tag{2.21}$$

In summary, three equivalent ways of expressing the reference pressures to compute the intercell transmissibility for a cell pair are shown in 1D (Eq.(2.22)).

- Pore volume weighted average of the steady state pressure for each cell
- Cell center steady state pressure for each cell
- Pseudo steady state pressure drop across each cell

$$\Delta p_{PSS} = \Delta \bar{p}_{SS} = \Delta p_{SS}^{Center} \tag{2.22}$$

Although equivalent in 1D, these three approaches differ when used as the basis of an upscaling calculation. Of these approaches, the first follows directly from the volume averaged form of the diffusivity equation. The second provides the relationship to a finite difference construction, and provides the definition of a cell center. The last approach is formally equivalent to the first in 1D, but will provide the basis for the upscaling approach developed in this study.

Interestingly, much of the upscaling literature follows a bulk volume averaged form of Darcy's equation either expressed in terms of an effective permeability or the upscaled cell transmissibility, Eq.(2.6). Neither has any dependence upon the porosity, and each may be consistently derived using steady state pressure solutions. In contrast, when developing an upscaling approach for flow based upon transients, a pore volume

weighted average arises, and we also may take advantage of the intrinsic relationship between steady state and pseudo steady state solutions derived above.

2.3 Pressure Averaging

In the above section, an equivalence relationship between PSS and SS definitions of transmissibility was established. To extend this PSS construction to multiple dimensions, a face pressure on a surface needs to be defined if the pressure on the surface is not uniform. The average pressure can be developed from the specification of the total flux across the surface. Specifically, consider the total flux across a surface (q_f) expressed in terms of the intercell transmissibilities, T_ℓ, and the pressures, $p_{1,\ell}$ and $p_{2,\ell}$, for the cell pairs on the two sides of the surface (Figure 2.2).

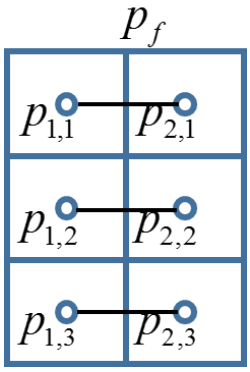

Figure 2.2: Stack of cells describing flux continuity at the shared face

$$q_f = \frac{1}{\mu}\sum_\ell T_\ell \cdot \left(p_{1,\ell} - p_{2,\ell}\right) \tag{2.23}$$

Flux equivalence (continuity) at the face leads to a transmissibility weighted definition of the average face pressure, p_f.

$$q_f = \frac{2}{\mu}\sum_\ell T_\ell \cdot \left(p_{1,\ell} - p_f\right) = \frac{2}{\mu}\sum_\ell T_\ell \cdot \left(p_f - p_{2,\ell}\right) \tag{2.24}$$

$$p_f \equiv \frac{1}{2}\sum_\ell T_\ell \cdot \left(p_{1,\ell} + p_{2,\ell}\right) \Big/ \sum_\ell T_\ell \tag{2.25}$$

The flux equivalence provides a relationship between the cell pressures on each side of the surface, the average face pressure, and the flux. At a boundary of the computational domain, the half cell transmissibility and the face pressure are used in this average instead of the intercell transmissibility and the adjacent cell pressure. If the face is considered at a no flow boundary condition, then the face pressure just becomes the transmissibility weighted average of the upstream cell pressures.

$$p_f \equiv \sum_\ell T_\ell \cdot p_\ell \Big/ \sum_\ell T_\ell \tag{2.26}$$

As an example of the use of this flux based definition of the pressure average, flow in a 2D radial element of uniform thickness *h* is examined to evaluate the half cell transmissibility, Figure 2.3.

The Darcy velocity and its divergence expressed in 2D radial coordinates are given below.

$$u_r = -\frac{k}{\mu}\frac{\partial p}{\partial r} \quad u_\theta = -\frac{k}{\mu}\frac{1}{r}\frac{\partial p}{\partial \theta} \quad \nabla \cdot \vec{u} = \frac{1}{r}\frac{\partial}{\partial r}\left(r u_r\right) + \frac{1}{r}\frac{\partial u_\theta}{\partial \theta} \tag{2.27}$$

The total flux in each direction is obtained as an integral of the Darcy velocity across the appropriate cross-section.

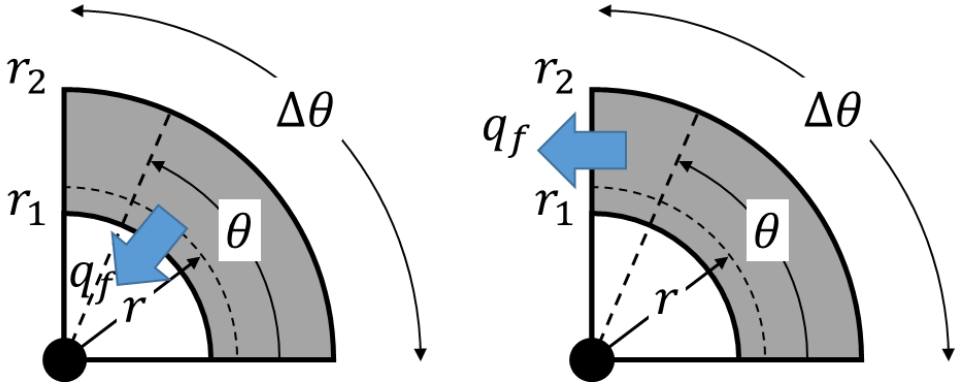

Figure 2.3: 2D radial element (a) Radial flow (b) Azimuthal flow

The flux profiles for radial and azimuthal flow are given in Eq.(2.28) and Eq.(2.29) respectively.

$$q(r) = -\int_{\Delta\theta} rhd\theta u_r = \frac{kh}{\mu} r \int_{\Delta\theta} d\theta \frac{\partial p(r,\theta)}{\partial r} \tag{2.28}$$

$$q(\theta) = \int_{r_1}^{r_2} hdr\, u_\theta = -\frac{kh}{\mu} \int_{r_1}^{r_2} \frac{dr}{r} \frac{\partial p(r,\theta)}{\partial \theta} \tag{2.29}$$

Each flow direction defines an average pressure specific to that direction of flow (Eq.(2.30) and Eq.(2.31)). The weights in the average are proportional to the local transmissibility, similar to the finite difference form of the pressure average, just shown.

$$q(r) = \frac{kh}{\mu} r \int_{\Delta\theta} d\theta \frac{\partial p(r,\theta)}{\partial r} = \frac{kh}{\mu} r\Delta\theta \frac{d\bar{p}(r)}{dr} \quad \bar{p}(r) \equiv \frac{1}{\Delta\theta} \int_{\Delta\theta} d\theta p(r,\theta) \tag{2.30}$$

$$q(\theta) = -\frac{kh}{\mu}\int_{r_1}^{r_2}\frac{dr}{r}\frac{\partial p(r,\theta)}{\partial \theta} = -\frac{kh}{\mu}\ln\left(\frac{r_2}{r_1}\right)\frac{d\bar{p}(\theta)}{d\theta}$$
$$\bar{p}(\theta) \equiv \frac{1}{\ln(r_2/r_1)}\int_{r_1}^{r_2}\frac{dr}{r}\,p(r,\theta) \tag{2.31}$$

For the two directional pseudo steady state solutions in the radial element, the total PSS flux corresponding to each face of the element may be integrated to obtain the average PSS pressure drop and corresponding half cell transmissibility. For radial flow through the r_1 face (Figure 2.3a), the PSS flux and the corresponding half cell transmissibility are given below:

$$q_{PSS}(r) = q_f \cdot \left(r_2^2 - r^2\right)\Big/\left(r_2^2 - r_1^2\right)$$
$$\frac{1}{T_1^{Half}} = \frac{\Delta\bar{p}_{PSS}}{\mu q_f} = \frac{1}{kh\Delta\theta}\int_{r_1}^{r_2}\frac{dr}{r}\frac{\left(r_2^2 - r^2\right)}{\left(r_2^2 - r_1^2\right)} = \frac{1}{kh\Delta\theta}\left(\frac{r_2^2}{r_2^2 - r_1^2}\ln\left(\frac{r_2}{r_1}\right) - \frac{1}{2}\right) \tag{2.32}$$

For radial flow through r_2 face, a similar result is obtained.

$$q_{PSS}(r) = q_f \cdot \left(r^2 - r_1^2\right)\Big/\left(r_2^2 - r_1^2\right)$$
$$\frac{1}{T_2^{Half}} = \frac{\Delta\bar{p}_{PSS}}{\mu q_f} = \frac{1}{kh\Delta\theta}\int_{r_1}^{r_2}\frac{dr}{r}\frac{\left(r^2 - r_1^2\right)}{\left(r_2^2 - r_1^2\right)} = \frac{1}{kh\Delta\theta}\left(\frac{1}{2} - \frac{r_1^2}{r_2^2 - r_1^2}\ln\left(\frac{r_2}{r_1}\right)\right) \tag{2.33}$$

For azimuthal flow (Figure 2.3b):

$$q_{PSS}(\theta) = q_f \cdot \theta/\Delta\theta$$
$$\frac{1}{T^{Half}} = \frac{\Delta\bar{p}_{PSS}}{\mu q_f} = \frac{1}{kh}\frac{1}{\ln(r_2/r_1)}\int_0^{\Delta\theta} d\theta\frac{\theta}{\Delta\theta} = \frac{1}{kh}\frac{1}{\ln(r_2/r_1)}\frac{\Delta\theta}{2} \tag{2.34}$$

These are the known solutions for the radial and azimuthal transmissibility within a 2D radial element. As an aside, these expressions for the PSS pressure drop may be used to determine the pressure equivalent center location for the radial element (Eq. (2.22)).

$$\ln r_c = \frac{r_2^2 \ln r_2 - r_1^2 \ln r_1}{r_2^2 - r_1^2} - \frac{1}{2} \quad \theta_c = \frac{1}{2} \cdot (\theta_1 + \theta_2) \tag{2.35}$$

The radial center is not at the cell centroid. For example, for a complete 360° radial element, the centroid is at $r = 0$, which is not within the cell, while this pressure equivalent location is always within the element.

In the radial PSS solution, a uniform value for $\nabla \cdot \vec{u}$ is consistent with a pressure that does not depend upon θ, so there is no distinction between $p(r,\theta)$ and $\bar{p}(r)$. However, for the azimuthal PSS solution, the pressure depends upon both coordinates, and this definition of $\bar{p}(\theta)$ has a non-trivial relationship to $p(r,\theta)$. This definition of the average pressure based upon the total flux correctly obtains the azimuthal transmissibility

To summarize, two examples were shown of the reduction of a multi-dimensional pressure distribution to an equivalent 1D pressure profile. The averaged pressure for a surface is defined to be consistent with the total flux across the surface. For a finite difference calculation, this fixes the weights to be the intercell transmissibility between elements. For a homogeneous element, as in the case of the radial element, the directional average pressures may be obtained analytically.

The two elements that will be used in the transmissibility upscaling approach are: the use of PSS pressure drops associated with the flux through each cell face, and the reduction of 3D pressure distributions to 1D pressure profiles by a flux-based pressure average.

Now, two ways of setting up a 3D PSS upscaling calculation are presented. One is to use no flow boundary conditions everywhere on the exterior of the domain except the flowing face and define an upstream average pressure using a local transmissibility weight as in Eq.(2.26) to calculate the reference PSS pressure drop for transmissibility (Δp_{PSS}). The second is to set up the upstream face as an isobar by making the total flow equal to zero but not necessary the local flow. The unknown upstream face pressure is obtained by solving the flow equation with this extra condition. A discussion of these approaches is presented in the following sub section.

2.3.1 3D Steady State Pressure Averaging

The set up for 3D steady state transmissibility upscaling is highlighted in Figure 2.4 where upstream and downstream isobars are imposed to drive flow. 3D steady state pressure equation (Eq.(1.1)) is solved for pressure and total flux given the uniform face pressures and no flow side boundary conditions.

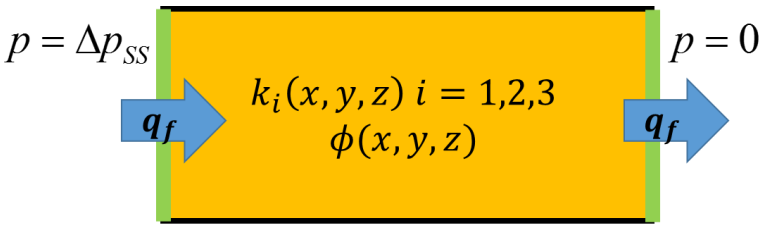

Figure 2.4: 3D Steady state pressure averaging

Pore volume weighted pressure ($\bar{p}_{SS}$) is calculated from the 3D solution to obtain reference pressure drop for half-cell transmissibility.

$$T^{Half\,1} = \frac{\mu q_f}{\Delta p_{SS} - \bar{p}_{SS}}; T^{Half\,2} = \frac{\mu q_f}{\bar{p}_{SS} - 0} \tag{2.36}$$

2.3.2 3D Pseudo Steady State Pressure Averaging

In 3D PSS flow pressure averaging, the 3D flow is reduced to an equivalent 1D flow using total flux and an average pressure. At PSS, the total flux can be obtained from the enclosed pore volume and is proportional to the face flux (q_f). Two scenarios are considered herein. The first is similar to the steady state set up with isobars at upstream and downstream faces and no flow side boundary conditions (Figure 2.5a). This approach is named PSSP. Total PSS flux at the downstream face is specified and zero total flux at the upstream face is imposed. The downstream isobar sets the gauge and the upstream isobar is a consequence of the zero total flux condition. This is a completely local upscaling calculation on the coarse grid, but not on the fine grid.

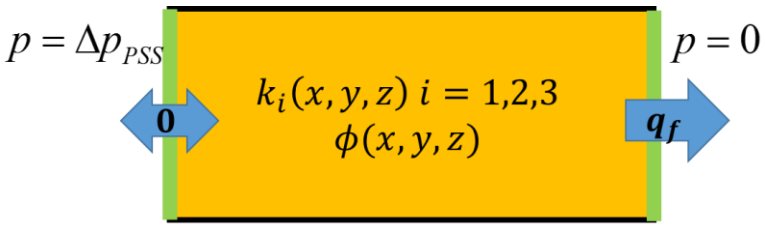

(a) 3D PSSP averaging

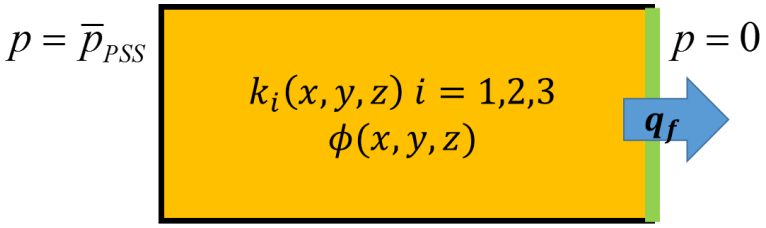

(b) 3D PSSQ averaging

Figure 2.5: 3D PSS pressure averaging

3D PSS pressure equations (Eq.(2.1)) are solved for the unknown upstream face pressure and the half-cell transmissibility with flow referenced to the downstream face is given by

$$T^{Half\,2} = \frac{\mu q_f}{\Delta p_{PSS} - 0} \tag{2.37}$$

Another PSS flow pressure averaging set up is described in Figure 2.5b where the flow is completely localized compared to the previous two flow descriptions. This approach is named PSSQ where the total flux is specified at the flowing face and no flow boundary conditions imposed on all other exterior faces. The total as well as the local flux is zero everywhere on the exterior faces except the flowing face which gives a completely local upscaling calculation both on the fine as well as the coarse grid. After solving the

3D PSS pressure equations, the upstream average face pressure ($\bar{p}_{PSS}$) is calculated as a local transmissibility weighted average as described in Eq. (2.26). The half-cell transmissibility now is given by Eq.(2.38). The transmissibility calculated using this approach is always less than or equal to the transmissibility calculated by PSSP. Both of these PSS upscaling approaches will exposed further for upscaling calculations in the next chapter.

$$T^{Half\,2} = \frac{\mu q_f}{\bar{p}_{PSS} - 0} \tag{2.38}$$

2.4 Discussion

This chapter presented a review of transmissibility construction using steady state and pseudo steady state concepts. The reference pressure drop for steady state transmissibility was shown to be the pore volume averaged pressure drop and the 1D cell center was defined using the steady state and the averaged steady state pressure profile. The center defined this way guarantees to be within the cell and may not coincide with the geometric centroid as shown in the radial flow example.

The PSS transmissibility construction in 1D was made possible due to an equivalence relation derived between pore volume averaged steady state pressure drop and the total PSS pressure drop. Superposition of PSS pressure drops was shown to recover SS pressure drop making the PSS solutions more general than steady state. This is because flux is not assumed to be uniform in the direction of flow unlike a steady state calculation.

A new form of PSS pressure averaging was introduced to extend the 1D PSS transmissibility construction to 3D for upscaling purposes. The averaging procedure was

motivated by defining a face pressure based on flux continuity. The averaging approach was demonstrated on a 2D radial element with both radial and azimuthal flow. Two types of 3D PSS flow problems were presented, one with zero total flux at the upstream face but not necessary the local flux (PSSP) and the other with a zero local flux on all external faces except the flowing face (PSSQ). A steady state upscaling calculation is explicitly coupled to the upstream and downstream pressure boundary conditions and implicitly coupled to the large scale boundary conditions. PSSP calculation is weakly coupled to the upstream and downstream faces and PSSQ calculation has the advantage of complete localization. PSS flow in general is driven the natural reservoir energy whereas steady state flow depends on the choice of boundary conditions.

In the next section, PSS upscaling formulation is formally presented using the results derived in the current section.

CHAPTER III

PSEUDO STEADY STATE UPSCALING*

3.1 Methodology

In this section, the PSS upscaling formulation is formally presented. Since at PSS, flux varies linearly with pore volume (Matthews et al. 1954), the slightly compressible 3D diffusivity equation is rewritten in terms of pore volume and face flux (Eq.(3.1)).

$$\nabla \cdot \vec{u} = \phi c_t \frac{\partial p}{\partial t} = \pm \phi \frac{q_{face}}{V_p} \tag{3.1}$$

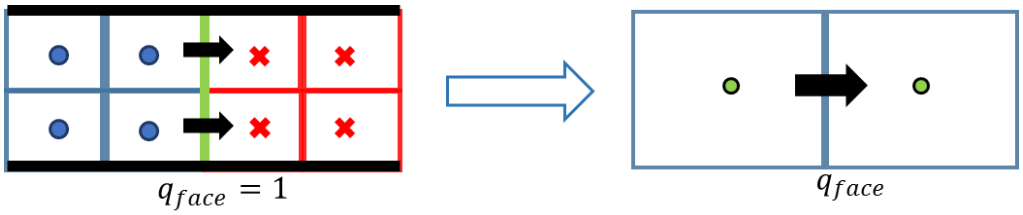

Figure 3.1: 2x2 PSS upscaling formulation

The PSS upscaling set up is described in Figure 3.1 where effective transmissibility is calculated between a coarse block pair using an imposed coarse face flux and total PSS

*Part of the data reported in this chapter is reprinted with permission from "Dynamic Downscaling and Upscaling in High Contrast Systems" by Nunna and King, 2017: Paper SPE-186289-MS presented at SPE Reservoir Simulation Conference held in Montgomery, Texas, USA, 20–22 February 2017. Copyright 2017, Society of Petroleum Engineers.

*Part of the data reported in this chapter is reprinted with permission from "Application of Pressure Transient Concepts for Improved Upscaling of Geologic Models" by Nunna 2017: Paper SPE-189293-STU presented at the SPE Annual Technical Conference and Exhibition held in San Antonio, Texas, USA, 9-11 October 2017. Copyright 2017, Society of Petroleum Engineers.

pressure drop. Unlike steady state flow based upscaling where flow is driven by artificially imposed pressure isobars, the flow in PSS upscaling is driven by the source terms attributed to the compressibility driven natural reservoir energy. In Figure 3.1, the side boundary conditions are no flow while the choice of upstream and downstream boundary conditions differ for the two different PSS upscaling approaches which will be described in this work – PSSQ and PSSP. The upstream cells act as a source and the downstream cells as a sink. The strength of the source/sink terms in each fine cell are proportional to the pore volume and are scaled by the total imposed flux at the coarse face (Eq.(3.1)).

The use of superposition gives a simple and useful relation between PSS and SS as discussed before. The superposition to two PSS solutions with equal and opposite source/sink terms gives a SS solution but not vice versa i.e., PSS solutions are more complete and steady state is only one subset of the solutions that PSS can describe. Figure 3.2 describes the example where SS flow in the blue coarse block is described using superposition of PSS flow between the blue-red and the green-blue coarse cell pairs. The PSS flow description has the advantage of reducing the dependence on large scale boundary conditions by utilizing the local source/sink terms to drive flow for a local upscaling calculation.

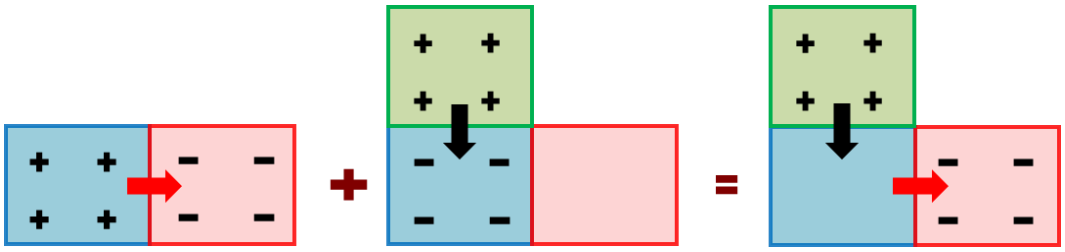

Figure 3.2: Sum of two local PSS calculation giving a SS flow profile (Reprinted with permission from Nunna and King 2017)

After defining the source/sink terms and the boundary conditions, one additional gauge condition is required to close the loop and obtain a discrete solution of Eq.(3.1). Two choices were explored for this: one is to set the pore volume average of the pressures to vanish (Eq.(3.2)) and the other is to impose an additional constraint on the shared face by making it an isobar ($p_{face} = 0$). Although Eq.(3.2) relaxes the additional assumption on the shared face, there are some instances which may lead to material balance issues. For instance, in Figure 3.3, a barrier running across the coarse cell pair causes material balance issue. The source term of fine cell 1 does not necessarily equal the sink term of sink term of cell 2 although the total flux is preserved by construction. This results in a material balance issue making the coefficient matrix of the discrete equation singular and forcing a zero effective transmissibility. Imposing the shared face as an isobar always guarantees non-negative transmissibility by allowing fluid to leak through the shared face in case of barrier as in Figure 3.3.

$$\sum_i p_i PV_i = 0 \tag{3.2}$$

(a) Issue **(b) Solution**

Figure 3.3: Disconnected pay issues in PSS upscaling

The use of PSS concepts for upscaling was first described by Karimi‐Fard et al. 2006 in the context of dual porosity matrix fracture simulation. The PSS upscaling was used to describe flow in fracture systems. Although the flow calculation is similar to Karimi‐Fard et al. 2006, the current approach differs in the calculation of effective transmissibility using the pressure averaging technique described in the previous chapter. The PSS construction is also similar to the work done by Aarnes 2004 and Lie, K.-A. et al. 2012 for computing basis function in multiscale simulation.

3.2 PSSQ and PSSP Transmissibility Upscaling Formulation

In this section, two different choices of setting up the PSS upscaling formulation is described through the choice of defining the upstream and downstream face boundary conditions. The PSSQ approach imposes no flow on the entire outer periphery making it completely localized (Figure 3.4a). After discretizing Eq.(3.1) and solving for the local pressures, the average upstream and downstream face pressures are calculated as

transmissibility weighted average (Eq.(3.3)) as discussed in the previous chapter. The weight T_i in Eq.(3.3) refers to twice the intercell transmissibility or half-cell transmissibility along the outer fine cell faces. Intercell transmissibility is the default choice unless the face is on the boundary of the reservoir or is surrounded entirely by a non-pay barrier.

$$\bar{p} = \frac{\sum_{i \in up/down\ face} p_i T_i}{\sum_{i \in up/down\ face} T_i} \tag{3.3}$$

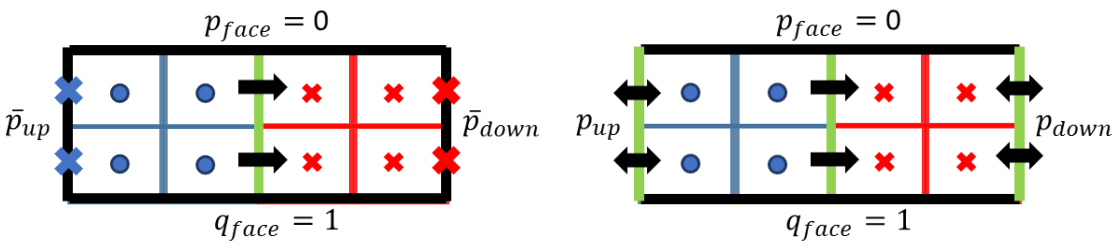

(a) PSSQ **(b) PSSP**

Figure 3.4: PSS transmissibility upscaling formulation

The upscaled inter cell transmissibility is computed from the average upstream and downstream face pressures given by Eq.(3.4)

$$\frac{1}{T_{PSSQ}^{Eff}} = \frac{\bar{p}_{up} - \bar{p}_{down}}{\mu q_{face}} \tag{3.4}$$

The PSSP approach relaxes the assumption of no flow upstream and downstream boundary conditions by allowing the leaky local flow but keeping the total flux equal to zero. This is done by setting the boundary face as an isobar with unknown pressure that is

to be calculated. One additional equation for each face is required which is given by Eq.(3.5). Interestingly, this equation is the similar to the transmissibility weighted average described for the PSSQ algorithm (Eq.(3.3)). The main difference here is that the face pressure is imposed as a uniform isobar for PSSP while no such condition is required for PSSQ. The equation for upscaled PSSP inter cell transmissibility is similar to Eq.(3.4) with the upstream and downstream face pressures now being uniform (Eq.(3.6)).

$$\sum_{i \in up,down\ face} T_i \left(p_i - p_{PSS} \right) = 0 \tag{3.5}$$

$$\frac{1}{T_{PSSP}^{Eff}} = \frac{p_{PSS}^{up} - p_{PSS}^{down}}{\mu q_{face}} \tag{3.6}$$

This formulation is inspired from the variational formulation of the diffusivity equation which is based on minimizing the work required to move fluids through the subsurface volume (Stewart 1968). Given a volume Ω where we specify either p or $\vec{n} \cdot \vec{\vec{k}} \cdot \nabla p$ on its boundary, $\partial\Omega$ then the dissipation must be minimized, where the dissipation is proportional to Eq.(3.7). Minimizing Eq.(3.7) is equivalent to solving the Laplace equation and gives the additional equation Eq.(3.5).

$$\iiint_{\Omega} d^3x \nabla p \cdot \vec{\vec{k}} \cdot \nabla p \tag{3.7}$$

3.2.1 Two-point Upscaling Diagnostics - SS vs PSS

In this section, the advantage of using PSS concepts for upscaling is highlighted with two simple numerical examples with $2 \times 2 \times 2$ coarsening. The two-point flux diagnostic measure proposed by Kasap and Lake 1990 is used to compare transverse and

longitudinal pressure drops for the upscaling calculations. The transverse face pressure drops are calculated using the transmissibility weighted pressures at the no flow transverse boundaries.

Case 1

Figure 3.5 describes the permeability field for case 1. The pressure solutions for steady state, PSSQ and PSSP upscaling are shown in Figure 3.6.

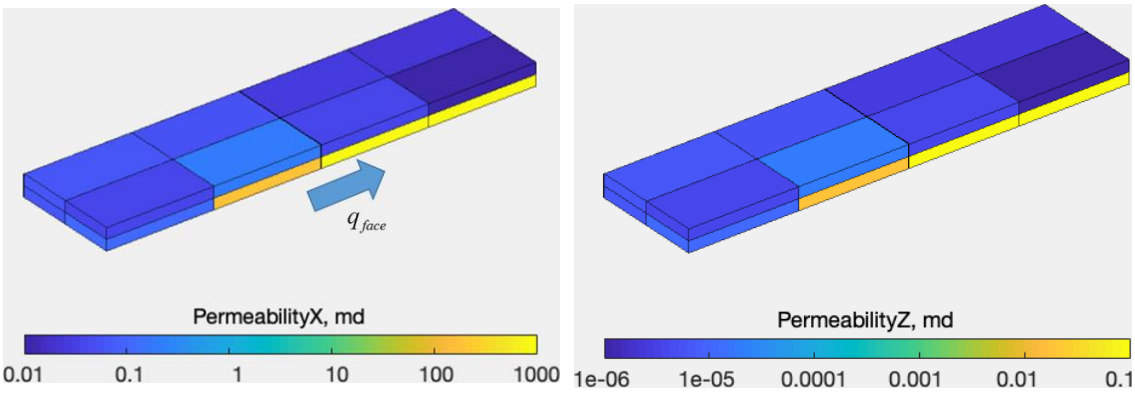

Figure 3.5: Case 1 - 2x2x2 permeability in X and Z directions

The amount of crossflow can be quantified by comparing the transmissibility weighted average transverse pressure drops with the longitudinal average pressure drop for each upscaling calculation. Table 3.1 represents the longitudinal and transverse pressure drops for each upscaling calculation. The numbers in the parenthesis represent the transverse pressure drop as a percentage of longitudinal pressure drop. Clearly, SS has the highest cross flow in the vertical direction whereas both PSSQ and PSSP calculations

have a minimal transverse pressure drops. This is also evident from the pressure maps in Figure 3.6. Notice, the reference SS pressure drop for transmissibility is negative because the pore volume averaged difference does not always guarantee non-negative transmissibility especially in the presence of strong cross flow. The PSS calculations on the other hand have no restriction on flux being uniform in a way SS does, instead the flux profile may follow the local heterogeneity which highlights one of the advantages of using PSS concepts for upscaling. Another key difference between the SS and PSS methods is the averaging procedure. The transmissibility weighted pressure average used for PSS methods emphasizes the high flow regions over the low flow cells by means of transmissibility. This is not true for the pore volume which is evident from the negative pressure drop for the steady state upscaling calculation in Table 3.1.

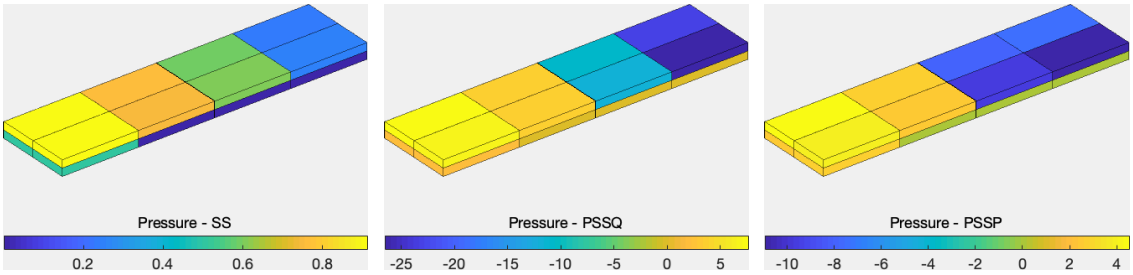

(a) Steady state **(b) PSSQ** **(c) PSSP**

Figure 3.6: Case 1 - Pressure solutions for 2x2x2 upscaling calculations

	$\Delta\bar{p}_{SS}$	Δp_{PSSQ}	Δp_{PSSP}
I (longitudinal)	-0.06	3.47	3.24
J (transverse)	0.0002 (0%)	0.0003 (0%)	-0.0004 (0%)
K (transverse)	0.73 (1200%)	0.96 (28%)	0.59 (18%)

Table 3.1: Case 1 - Average pressure drops in each direction for 2x2x2 steady state, PSSQ and PSSP upscaling

Case 2

Figure 3.7 shows the permeability map for case 2 and Figure 3.8 the corresponding pressure distributions for the upscaling methods tested. The longitudinal and transverse pressure drops are tabulated in Table 3.2. Most of the permeability distribution is high except the downstream right blocks at the bottom (Figure 3.7). Compared to PSS methods, there is significant amount of cross flow in the vertical direction for steady state as tabulated in Figure 3.9 and Table 3.2 through the transverse pressure drop calculations. This is due to the uniform flux assumption in steady state whereas for both the PSS methods, the velocity is mostly aligned to the longitudinal pressure drop and most of the pressure drop is seen only around the low permeability region towards the right. Both PSS calculations show less artifacts and vertical cross flow dominates in SS but not for PSS methods.

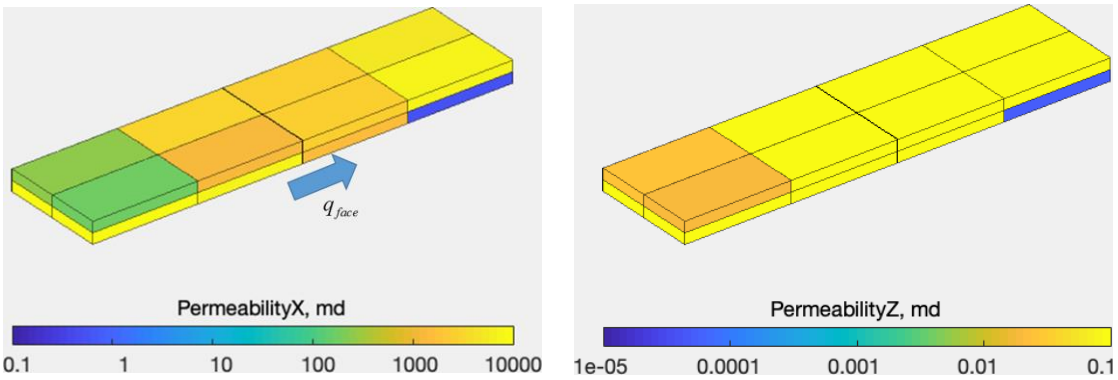

Figure 3.7: Case 2 - 2x2x2 permeability in X and Z directions

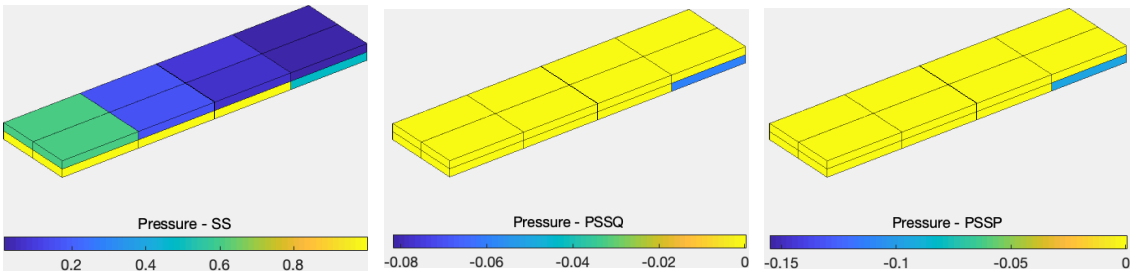

(a) Steady state **(b) PSSQ** **(c) PSSP**

Figure 3.8: Case 2 - Pressure solutions for 2x2x2 upscaling calculations

	$\Delta\bar{p}_{SS}$	Δp_{PSSQ}	Δp_{PSSP}
I (longitudinal)	0.3553	0.00017723	0.0006295
J (transverse)	-0.0448 (4%)	-1.31E-05 (7%)	-4.41E-05 (7%)
K (transverse)	-0.9285 (261%)	-0.000113 (64%)	-0.0004229 (67%)

Table 3.2: Case 2 - Average pressure drops in each direction for 2x2x2 steady state, PSSQ and PSSP upscaling

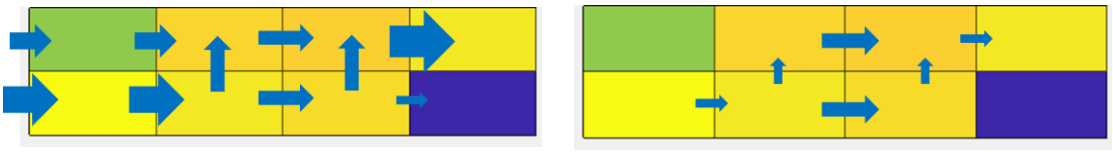

(a) Steady State flow **(b) PSS flow**

Figure 3.9: Case 2 - Vertical cross flow in SS and PSS upscaling calculations

Both the above test cases highlight the advantage of using PSS concepts for flow based upscaling.

3.3 PSS Well Index Upscaling Formulation

Well index definition is based upon a steady state pressure drop from the bottomhole flowing pressure to a reference pressure. In the context of local well index upscaling, the well index is expressed using PSS flow and superposition of the pressure drops from the cell to bottomhole and the cell to neighboring cells (Eq.(3.8)). The well index is defined by the pressure drop from the bottomhole to the cell (Eq.(3.9)) and the pressure drop from the cell to neighboring cells is the transmissibility piece given by the numerical finite difference calculation which has already been described in the above sections (Eq.(3.10)). The equations are pictorially represented in Figure 3.10.

$$\left(\Delta p_{SS}\right)_{NextCell}^{Bottomhole} = \left(\Delta p_{PSS}\right)_{Cell}^{Bottomhole} + \left(\Delta p_{PSS}\right)_{NextCell}^{Cell} \tag{3.8}$$

$$\left(\Delta p_{PSS}\right)_{Cell}^{Bottomhole} = \frac{\mu q_w}{WI} \tag{3.9}$$

$$\left(\Delta p_{PSS}\right)_{Cell}^{NextCell} = \frac{\mu q_w}{T_{Face}} \tag{3.10}$$

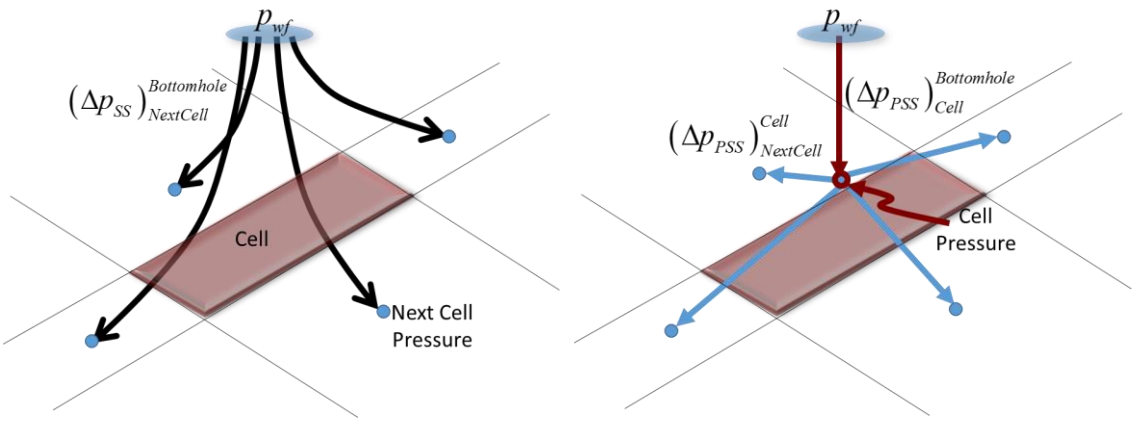

(a) Reference SS pressure drop **(b) PSS pressure drops**

Figure 3.10: SS and PSS pressure drops used to calculate well index

The pressure drop from the bottomhole to the cell faces is obtained from a reference calculation which sets the boundary conditions for the finite difference calculation. Peaceman 1978, 1983, 1990 used two wells or a well and a coarse cell boundary as reference pressures and then computed the well index and the equivalent wellbore radius under numerical refinement. Under numerical refinement, the impact of far field boundary conditions near the well are negligible and all that is left is the pressure drop due to the well which is used to calculate the well index. However, for an upscaling calculation, numerical refinement is not performed, instead a single cell Peaceman calculation is performed to evaluate the coarse well index.

As done for the PSS transmissibility, the well index upscaling is formulated using the same set up described for transmissibility upscaling. Instead of the face flux, the flow

is now driven by a well flux ($q_w = 1$). The bottomhole pressure ($p_{wf} = 0$) is set to a gauge pressure of zero and the averaging surface now becomes the outer boundary $\partial\Omega$ of the coarse block (Figure 3.11).

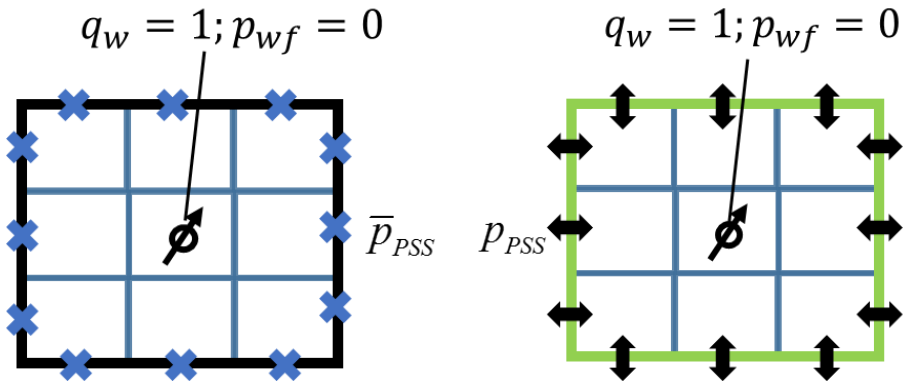

(a) PSSQ **(b) PSSP**

Figure 3.11: PSS well index upscaling

After solving the discretized version of Eq.(3.1), the upscaled well index is given by Eq.(3.11)

$$\frac{1}{WI_{PSS}^{Eff}} = \frac{p_{PSS} - p_{wf}}{\mu q_w} \tag{3.11}$$

The PSSP well index formulation is similar to the steady state well index formulation proposed by Durlofsky et al. 2000 where the upstream isobar is imposed on an extended domain instead of the boundary of the coarse block that contains the well.

Peaceman 1990 utilized analytic steady state radial flow pressures at the boundaries of the computation domain as boundary conditions (Eq.(3.12)) to evaluate the fine scale equivalent radius (r_o) for finite difference numerical calculation. This is done

by finding the well cell pressure (p_o) from the numerical calculation and the difference between well cell pressure and the bottomhole pressure defines the equivalent radius (Eq.(3.13)). This is identical to solving the difference between analytic and numerical pressures which vanishes at the boundary and matches the total flux from the well. This particular calculation corresponds to PSSP where the total flux conditions is imposed. However, the local flux at the boundary does not match the analytic radial solution. Therefore, PSSP is the preferred upscaling calculation over PSSQ.

$$p(x,y) = p_{wf} + \frac{\mu q_w}{2\pi kh} \ln\left(\frac{r_{xy}}{r_w}\right) \tag{3.12}$$

$$\ln\left(\frac{r_o}{r_w}\right) = \frac{2\pi kh}{\mu q_w}\left(p_o - p_{wf}\right) \tag{3.13}$$

The two proposed PSS well index methods are further tested on homogeneous models with known reference solutions. A 3×3 homogeneous test model was considered with different aspect ratios and well in the center of the coarse block. The reference coarse well index was calculated form the equivalent Peaceman radius (Eq.(3.14)) and the upscaled well indices were calculated using a flow based approach with the boundary conditions specified as above for PSS. For steady state, a uniform known isobar is specified on the outer boundary and the upscaled well index is evaluated based on the difference between pore volume averaged cell pressure and the specified bottomhole pressure. Eq. (3.14) is an approximation to the actual Peaceman radius as Peaceman 1990 clearly demonstrated the calculation is not so accurate for a single cell. Nonetheless, it may give us a direction on choosing the PSS upscaling approach for well index.

$$r_o = 0.14\sqrt{DX^2 + DY^2}$$
$$WI_{Peaceman} = \frac{2\pi kh}{\mu \ln\left(r_o / r_w\right)} \tag{3.14}$$

Four different aspect ratios were tested ($\alpha = DY/DX = 1, 2, 5, 10$) and Figure 3.12 describes the pressure maps with the corresponding well indices evaluated for steady state, PSSP and PSSQ. The error seems to increase with increase in aspect ratio as shown in Table 3.3. Both PSSP and SS well index upscaling methods show relatively less error compared to PSSQ. Henceforth, PSSP well index will be considered the preferred well index method for the current work. The upscaled transmissibilities will be evaluated based on PSSP and PSSQ but the well index calculation is restricted to PSSP method.

	Absolute Error (%)		
Aspect ratio	**SS**	**PSSP**	**PSSQ**
1	7.66	7.66	9.09
2	3.48	3.48	9.79
5	6.38	6.38	19.46
10	11.07	11.07	34.03

Table 3.3: Well index error evaluated for different aspect ratios

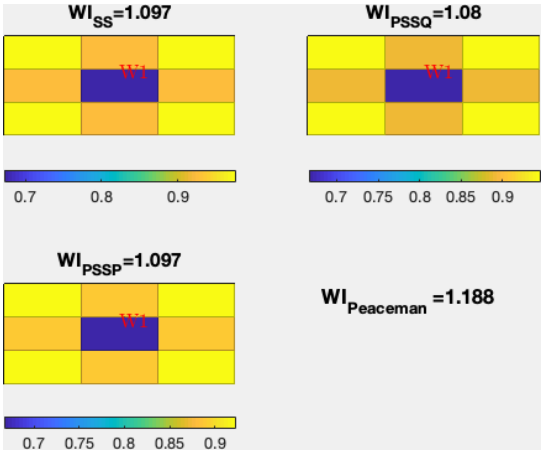

(a) Aspect ratio = 1

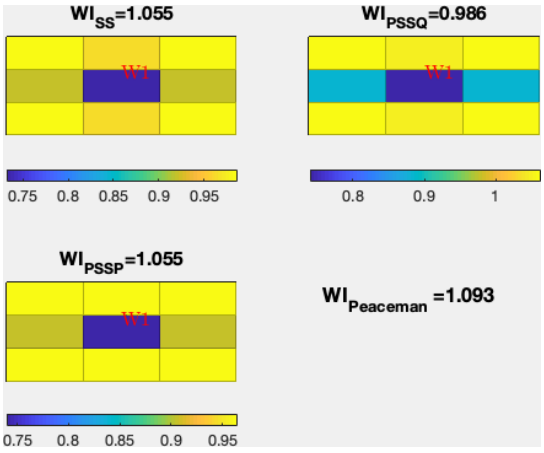

(a) Aspect ratio = 2

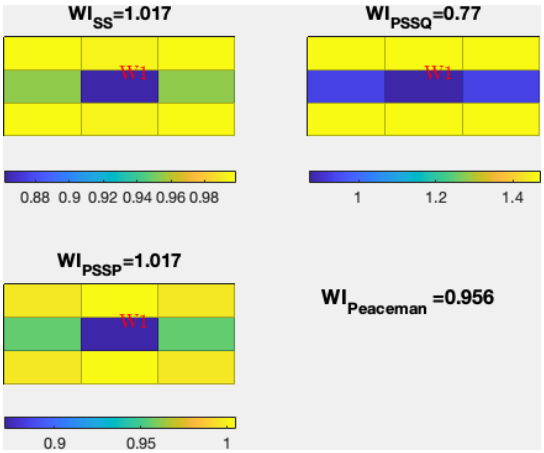

(a) Aspect ratio = 5

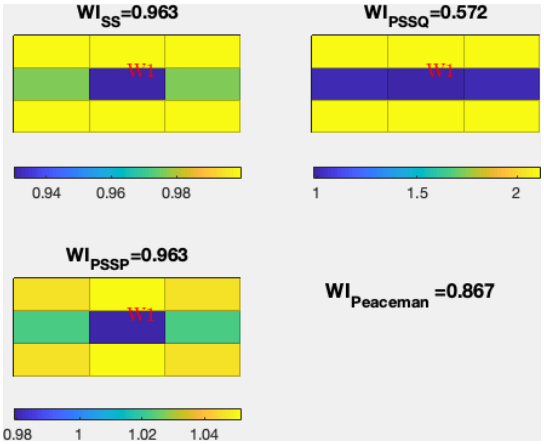

(a) Aspect ratio = 10

Figure 3.12: 3x3 Homogeneous well index comparison for SS, PSSP, and PSSQ

3.4 Numerical Experiments

The PSS upscaling formulation is tested on SPE10 synthetic reservoir model (Christie and Blunt 2001) and an onshore tight gas reservoir (Zhou and King 2011). In the original study, the SPE10 dataset was studied under secondary recovery. The current work is primarily restricted to single phase flow to study pressure and rate upscaling without the need to address multiphase flow issues which may be rigorously captured in a multiscale simulation framework.

The SPE10 model has been designed to be a challenge for upscaling algorithms. It is a $60\times220\times85$ cell model (1,122,000 cells in total) with uniform rectangular 20 ft x 10 ft x 2 ft cells. The architecture of the reservoir consists of sheet sands in the upper geologic unit and tortuous narrow channels in the lower unit (Figure 3.13). The facies distribution in Figure 3.13 is implicit in the model and is obtained from the ratio of vertical to horizontal permeability. The reservoir properties are highly heterogeneous with strong contrast between the porosity and permeability trends (Figure 3.14).

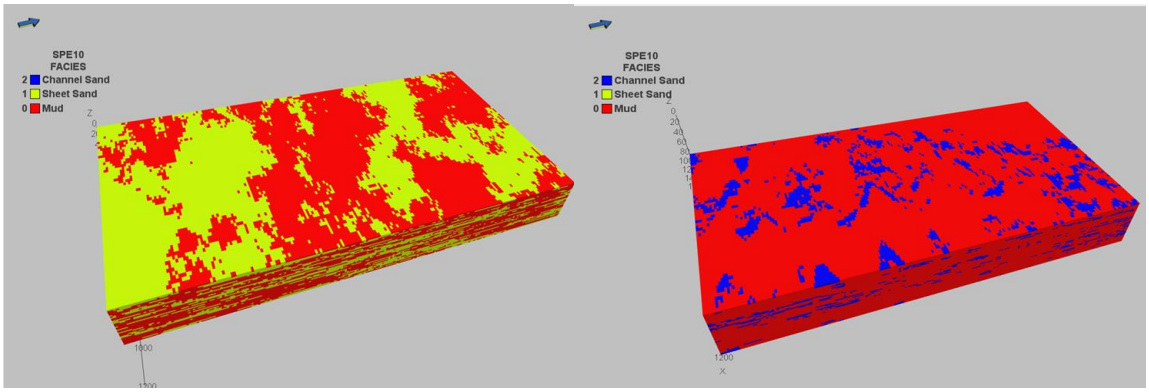

(a) SPE10 Upper geologic unit (Tarbert) **(b) SPE10 Lower geologic unit (Upper Ness)**

Figure 3.13: Facies description of the upper and lower geologic units of SPE10 (Reprinted with permission from Nunna and King 2017)

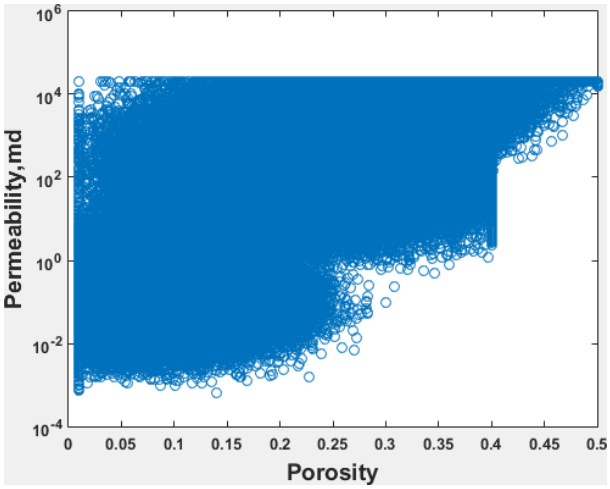

Figure 3.14: SPE10 permeability porosity cross plot

The tight gas reservoir model is a low net to gross reservoir undergoing primary depletion. Figure 3.15a describes the facies map of the high resolution 3D geologic model showing thin fluvial sands with intermittent connectivity. The model size 103×108×375 cells (~4 million cells) and the cells are 250 feet on the side and approximately 1 foot in

thickness. The areal grid is uniform while the vertical grid is stratigraphic. The model has been built with proportional layering within each zone. Less than 17% of the cells are active in the geologic model and we expect that continuity of the sand channels will be difficult to preserve. There is significant heterogeneity within the sand channels themselves, with permeability varying over four orders of magnitude. The reservoir has 81 vertical wells with 24 years of production history (Figure 3.15b).

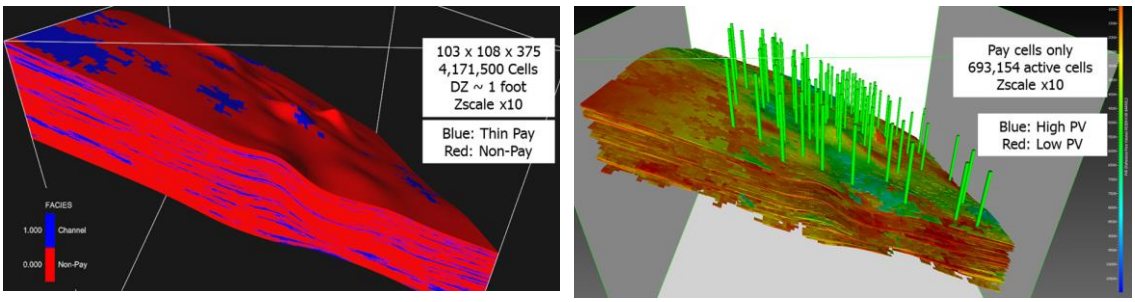

(a) Facies map **(b) Pore volume map**

Figure 3.15: Full field tight gas reservoir model (After Zhou and King 2011)

3.4.1 2D SPE10 Localization Test

In this section, the impact of localization i.e., the effectiveness of boundary conditions on the local upscaling methods is evaluated. The PSS upscaling approach is benchmarked against extended local (Holden and Lia 1992) and adaptive local global (Chen and Durlofsky 2006) upscaling methods. The 2D test case studied here is one of the steady state models considered in Chen and Durlofsky 2006 which is layer 55 of the SPE10 model with 1 injector and two producers (Figure 3.16). The injector I1 is placed at $(5,5)$ and the two producers are placed at $(5,175)$ and $(55,215)$ respectively. The coarsening

ratio is 10×10. The injector is maintained at bottomhole pressure equal to one and the producers at zero bottomhole pressure with steady state flow regime. As shown in the Figure 3.16, the test case has high contrast in properties with high permeability channels with low permeability sands in between making it a challenging case. The errors in localization are assessed by evaluating the error in face fluxes relative to the fine scale simulation. The face fluxes obtained from fine scale simulation are summed up to the resolution of the coarse grid to have a like for like comparison. The average error is quantified based on the total summed up flux consistent with the Chen and Durlofsky 2006 paper (Eq.(3.15)). The upscaling methods were implemented inside the Matlab Reservoir Simulation Toolbox environment (Krogstad et al. 2015;Lie, K.A. et al. 2012;Lie 2014).

$$\langle Error \rangle = 100 \times \left\| 1 - \frac{\sum q_{face}^{Coarse}}{\sum q_{face}^{Fine}} \right\| \tag{3.15}$$

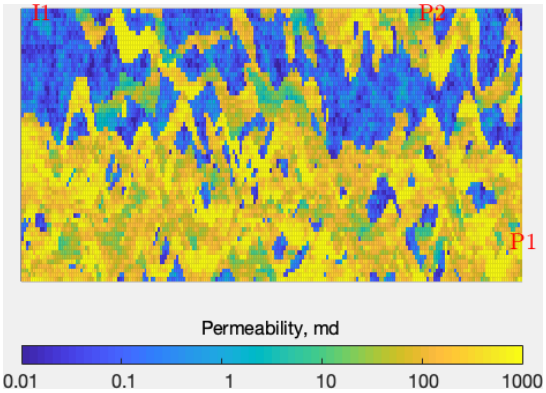

Figure 3.16: SPE10 layer 55 permeability

Figure 3.17 and Figure 3.18 describe the error in face fluxes in X and Y directions for extended local (EL), adaptive local-global (ALG), PSSQ and PSSP methods

respectively. While adaptive local-global is consistently accurate in both directions, extended local appears have to the largest error out of the four upscaling methods. This is not a surprise as ALG is specifically optimized to the particular well configuration considered here. Notice both PSSQ and PSSP perform reasonably well without reference to any global boundary conditions. This particular test case highlights the advantage of using PSS concepts for upscaling as opposed to a steady state technique.

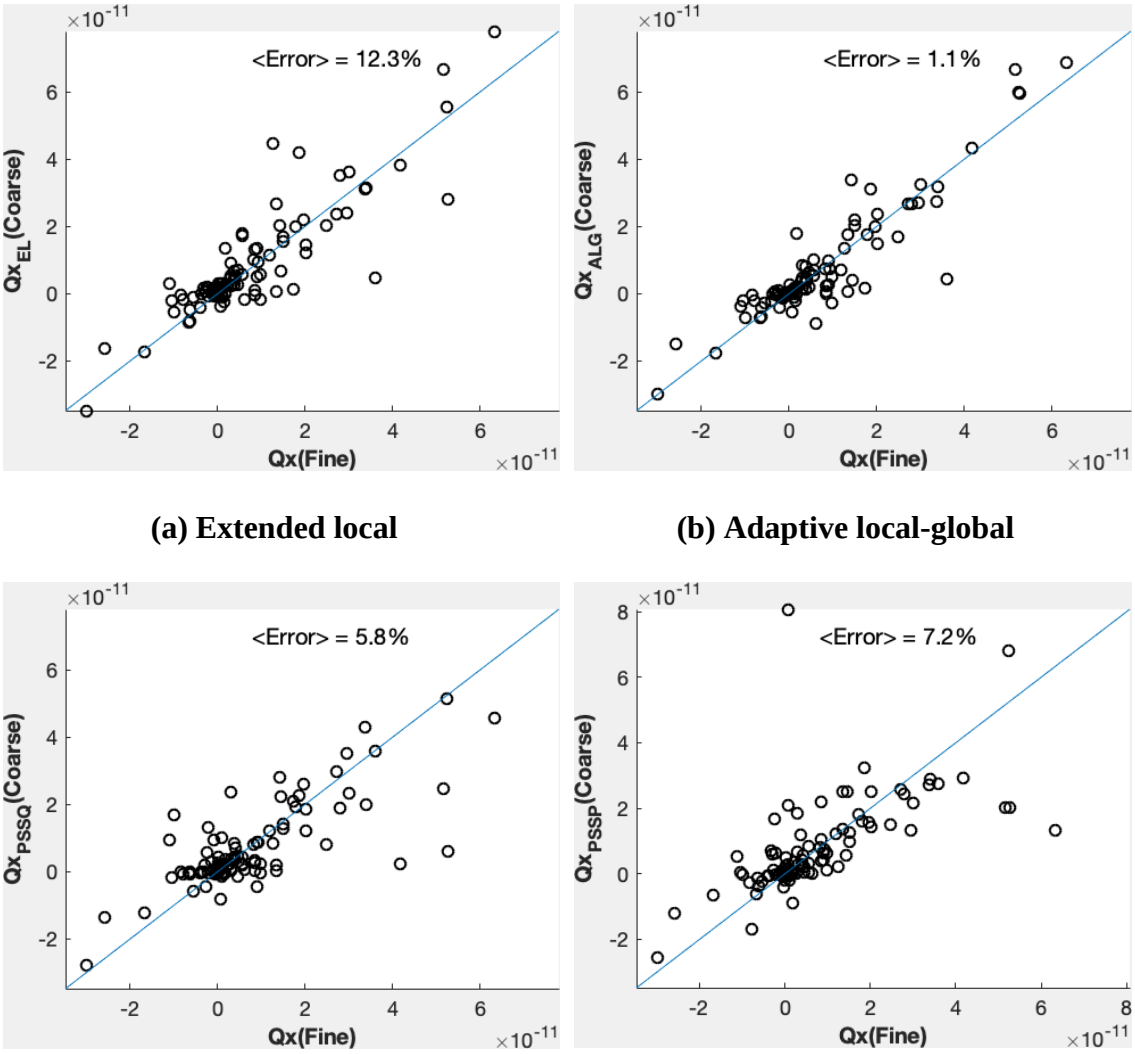

(a) Extended local **(b) Adaptive local-global**

(c) PSSQ **(d) PSSP**

Figure 3.17: SPE10 layer 55 X direction face flux comparisons for different upscaling methods

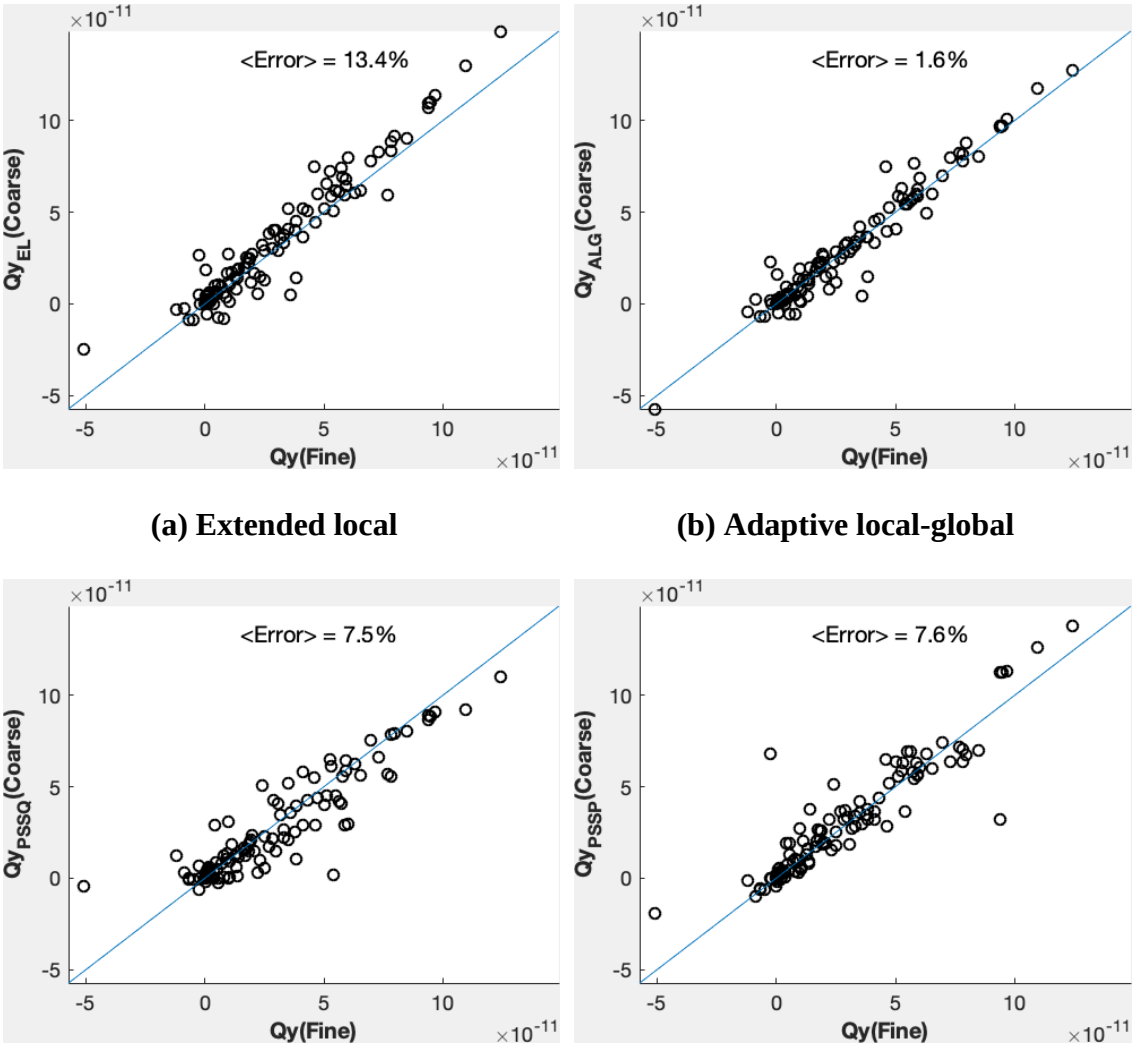

(a) Extended local **(b) Adaptive local-global**

(c) PSSQ **(d) PSSP**

Figure 3.18: SPE10 layer 55 Y direction face flux comparisons for different upscaling methods

3.4.2 3D SPE10 Single Phase Flow

In this section, the upscaling methods are evaluated on the entire SPE10 model with a producer and injector pair placed at the corners (Figure 3.19). The oil and rock

compressibilities were left to the default values of the original SPE10 dataset. The well constraints and simulation input data are summarized in Table 3.4.

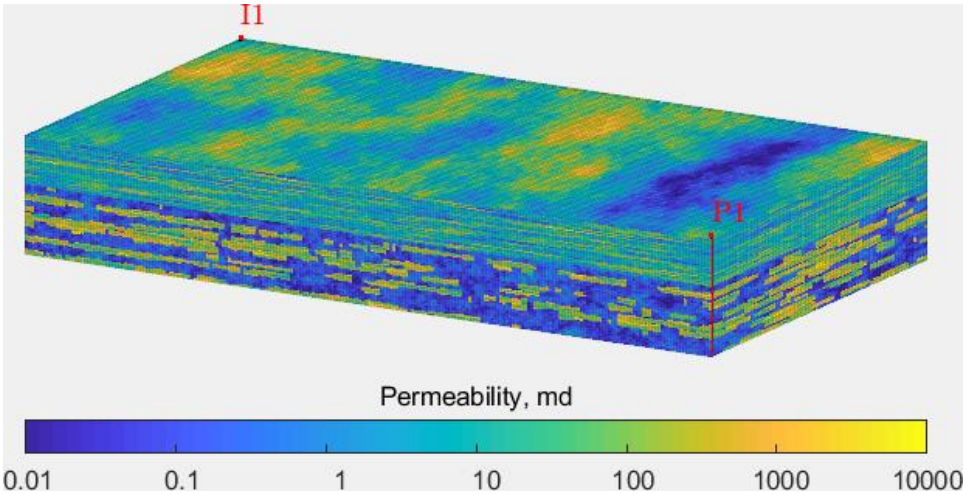

Figure 3.19: SPE10 model permeability map with injector and producer

Initial pressure, psia	6000
Rock compressibility, psi^{-1}	1e-6
Producer constraints	4000 psia bottomhole pressure
Injector constraints	2000 bbl/day target reservoir volume; 10000 psia bottomhole pressure constraint
Simulation time	1 year

Table 3.4: SPE10 single phase flow simulation input data

Five coarsening ratios ($1\times1\times4$, $2\times2\times1$, $2\times2\times2$, $3\times3\times1$ and $2\times2\times5$) are considered and the PSS upscaling methods are benchmarked against local steady state upscaling method with pressure isobars imposed on the upstream and downstream face

(Figure 3.20). The effective transmissibility is evaluated based on the face flux and the pore volume averaged pressure difference between the coarse blocks under consideration.

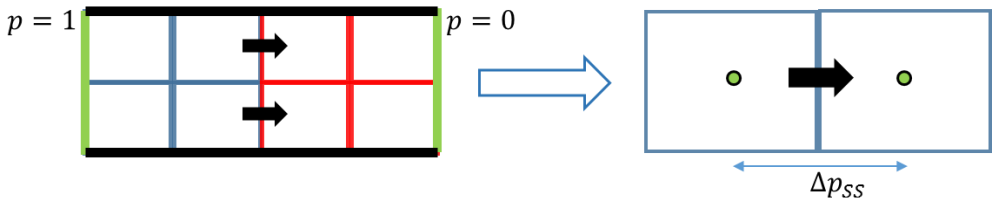

Figure 3.20: 2x2 local steady state upscaling

Figure 3.21 describes the cumulative oil recoveries for the 5 coarsening ratios. It is clear that both steady state and PSSP upscaling perform consistently better than the PSSQ upscaling method with regards to the well rates. However, the face flux error comparisons (Figure 3.22, Table 3.5) show that PSSP better captures the flow field compared to the steady state and PSSQ. For the sake of brevity, only 4 coarsening ratios are shown that capture the most information. The face fluxes are compared for the last time step and the error in face flux is computed using the L^2-norm given by Eq.(3.16).

$$e(q_{face}) = \frac{\left\| q_{fine} - q_{coarse} \right\|_{L^2}}{\left\| q_{fine} \right\|_{L^2}} \tag{3.16}$$

In summary, PSS upscaling results show consistently lower performance prediction relative to fine scale simulation for SPE10 model. The assumption of entire coarse blocks reaching PSS may not be valid in a high contrast model such as SPE10 especially in the lower geologic unit which represents high contrast highly channelized environment.

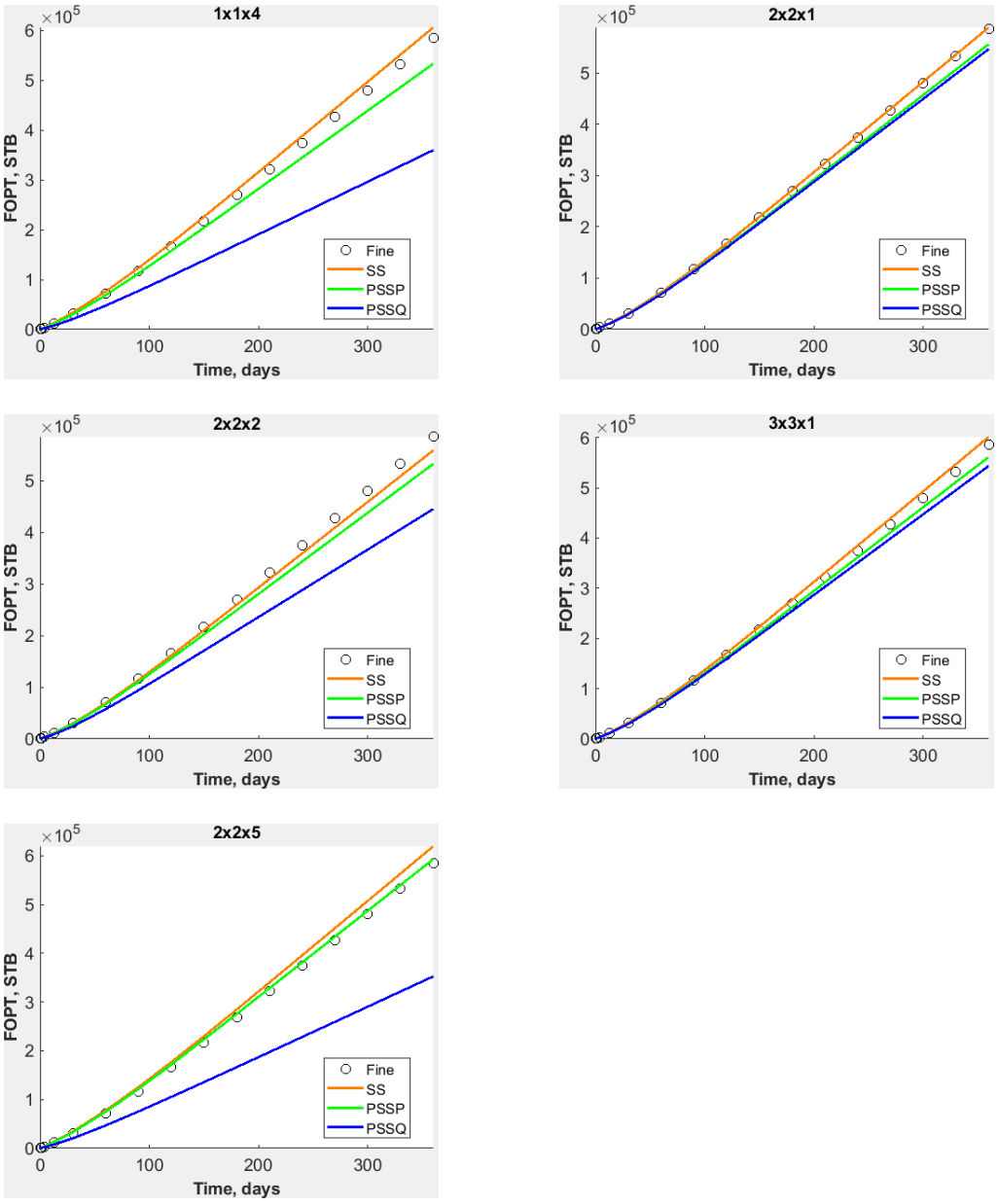

Figure 3.21: SPE10 single phase flow cumulative oil recovery for different coarsening ratios

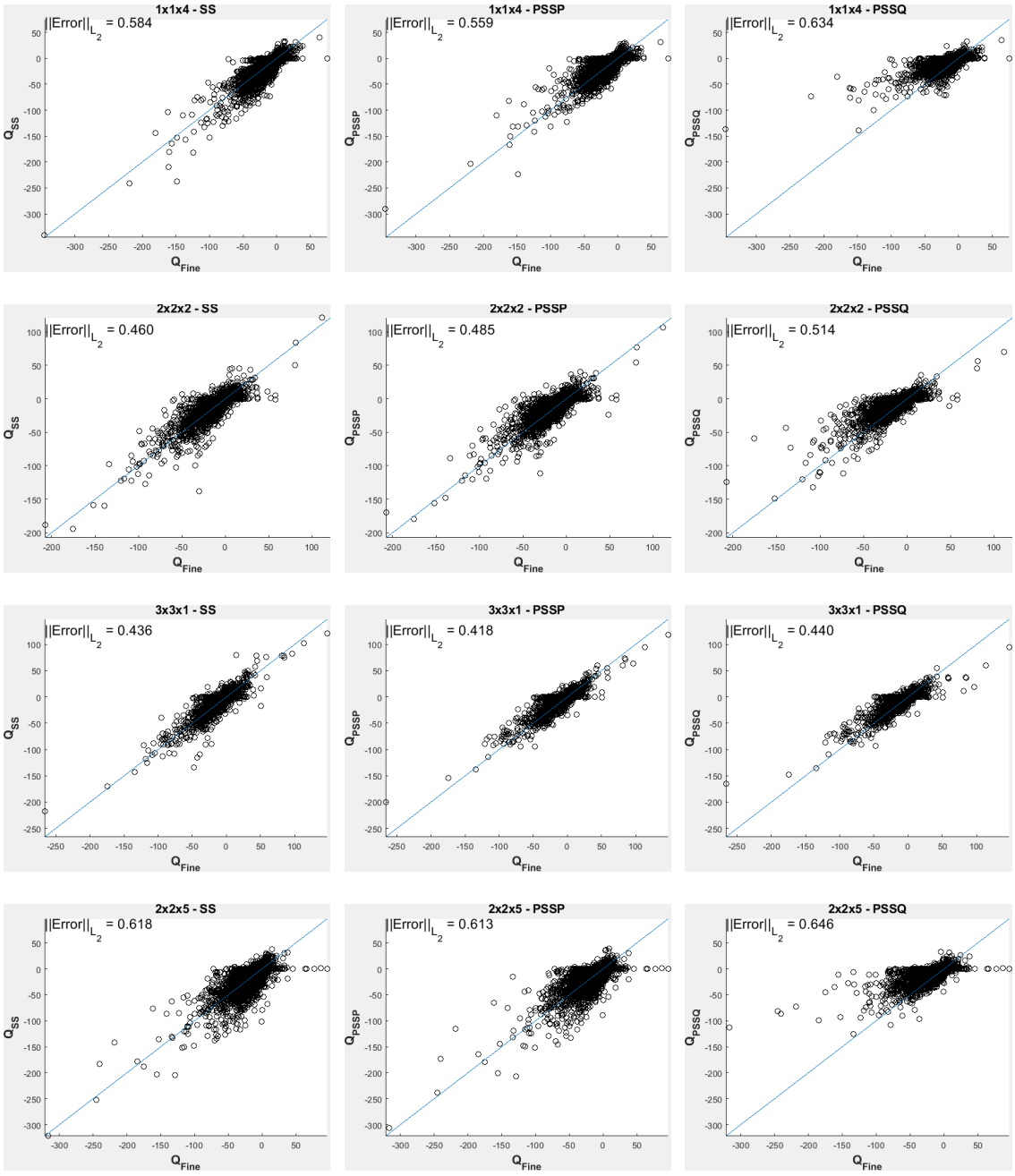

Figure 3.22: SPE10 single phase flow face flux comparisons for different coarsening ratios

	1×1×4	2×2×1	2×2×2	3×3×1	2×2×5
SS	0.584	0.333	0.460	0.436	0.618
PSSP	0.559	0.362	0.485	0.418	0.613
PSSQ	0.634	0.374	0.514	0.440	0.646

Table 3.5: SPE10 single phase flow face flux errors for different coarsening ratios

3.4.3 3D Low Contrast SPE10 Single Phase Flow

In this section, the PSS upscaling methods are tested on the low contrast Tarbert formation of the SPE10 model (layer 1-35). The formation contains fairly continuous sheet sands. The simulation input data and the coarsening ratios are kept same as the previous section. Figure 3.23 and Figure 3.24 describe the cumulative recoveries and face flux comparisons for the coarsening ratios considered in the previous section. Clearly, the PSS upscaling results show considerable improvement compared to the high contrast SPE10 model discussed before. Therefore, the assumption of reaching PSS in a low contrast coarse block may be a valid one.

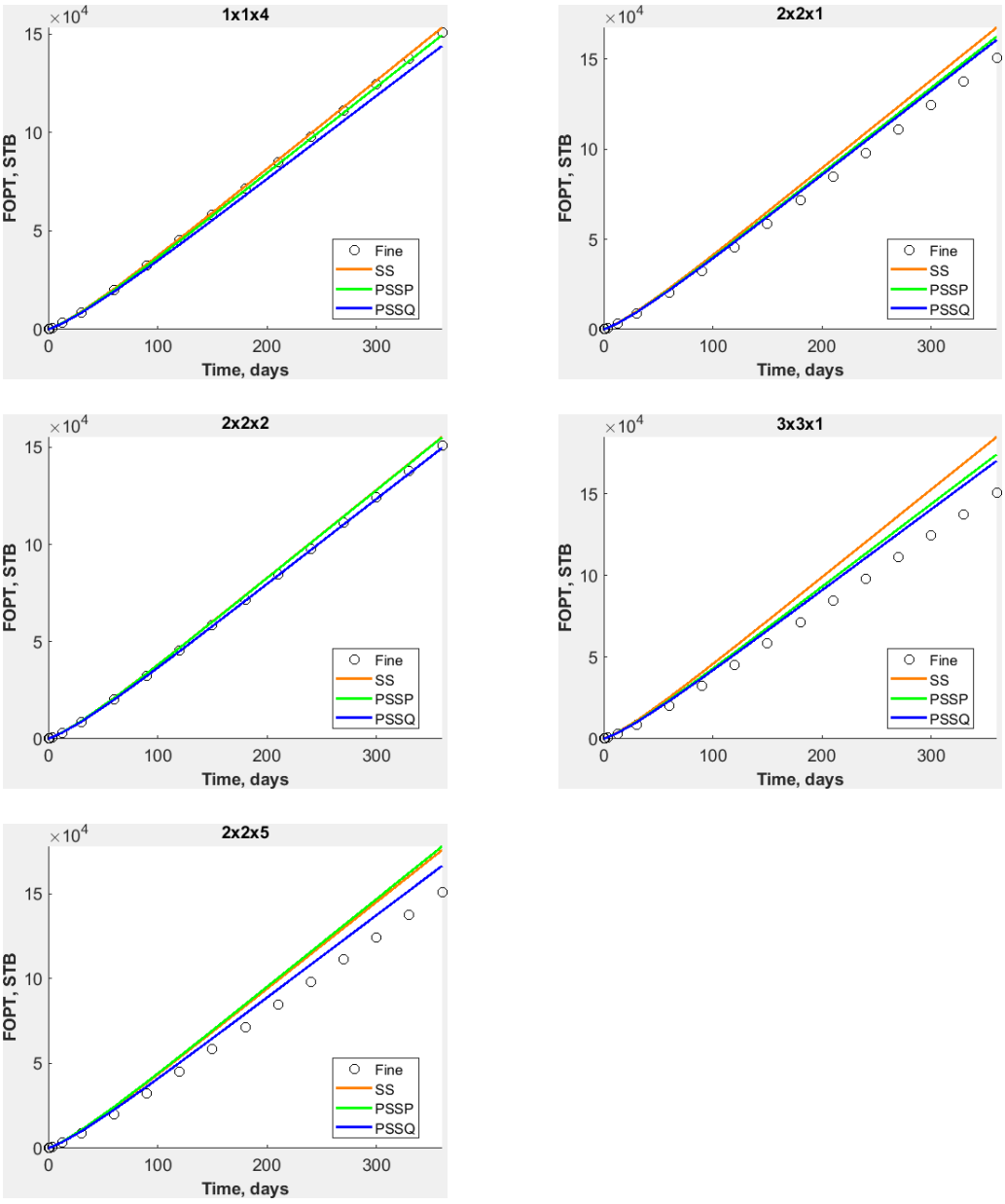

Figure 3.23: SPE10 Tarbert formation cumulative oil recovery for different coarsening ratios

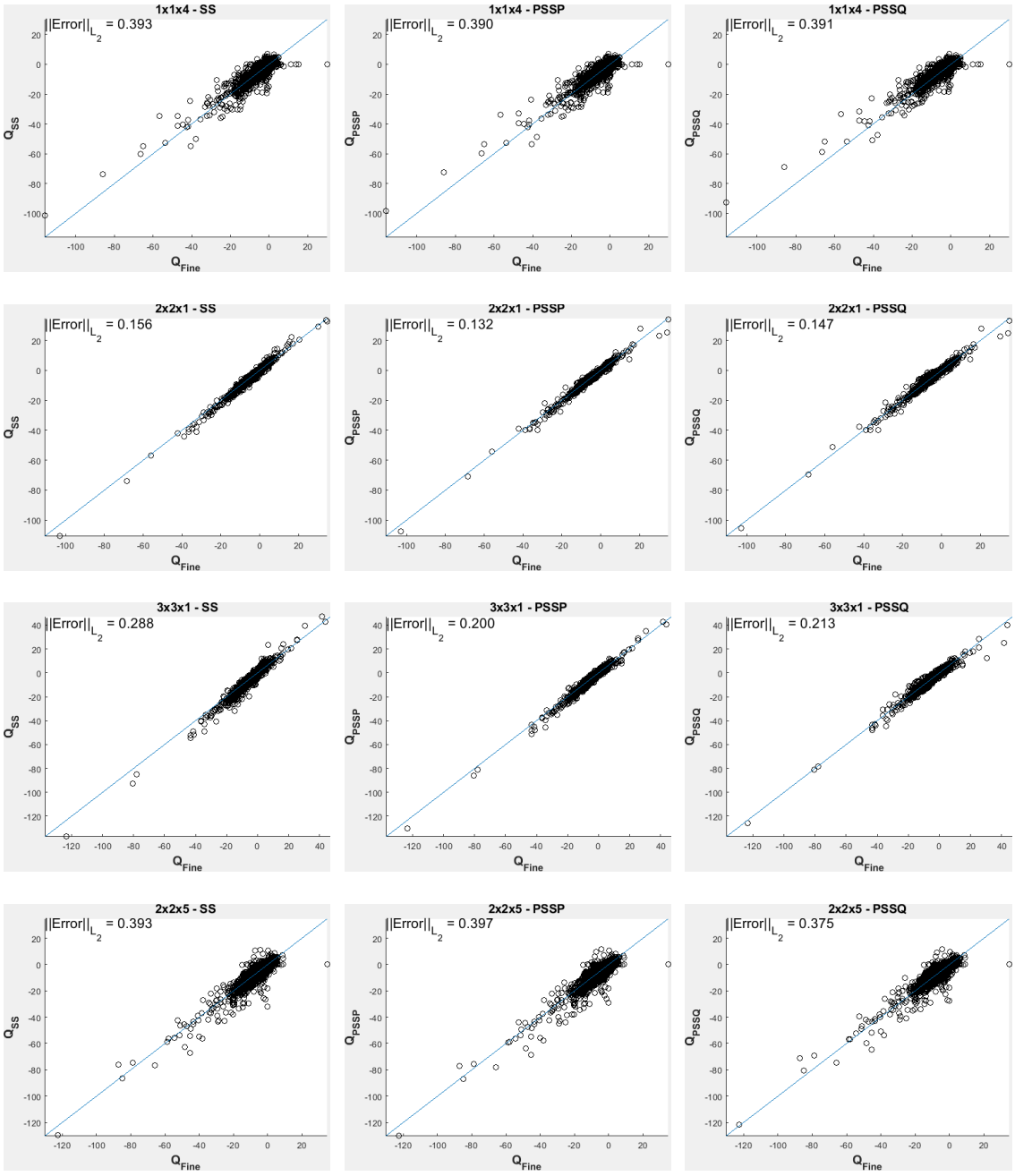

Figure 3.24: SPE10 Tarbert formation face flux comparisons for different coarsening ratios

3.4.4 3D Full Field Tight Gas Single Phase Flow

The upscaling results for the tight gas model (Figure 3.15) are presented in this section. The upgridding resolution in the vertical direction is performed based on pillar adaptive unstructured coarsening approach proposed by Zhou and King 2011. Three coarsening ratios are chosen: $1\times1\times\mathrm{N}$, $2\times2\times\mathrm{N}$ and $3\times3\times\mathrm{N}$. Here 'N' is obtained from the adaptive upgridding approach that preserves the vertical continuity in the fine cells that encompass a coarse block. Figure 3.25 describes the total cumulative gas recovery for the 24 year production history for the 3 coarsening ratios. For $1\times1\times\mathrm{N}$, all the upscaling methods yield accurate performance prediction relative to the fine scale simulation. This is due to the low contrast of permeability within each coarse cell obtained from adaptive vertical coarsening. For the areal coarsening cases, we can clearly see that steady state consistently overestimates while pseudo steady state consistently predicts accurate gas recovery compared to the fine scale model even at a lower resolution. For example, in $3\times3\times\mathrm{N}$ case, there are approximately 40,000 active cells in the coarse model compared to 4 million cells in the geologic model. Notice, there is hardly any difference between PSSP and PSSQ methods. The adaptive gridding of the tight gas example is a specialized upgridding application. When considering multiphase flow, for instance, gravity segregation is a fundamental mechanism which cannot be captured with such a grid design. However, the upscaling calculations demonstrated in this case have not been specialized to tight gas, and the high permeability contrast within the channels have made this a useful test case.

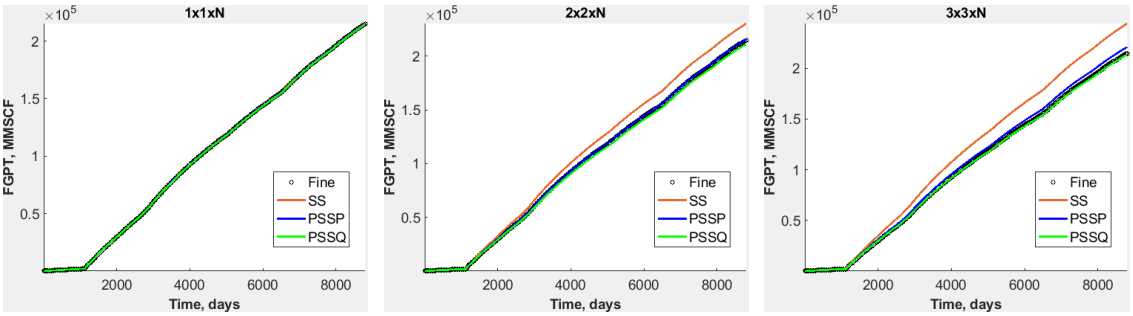

Figure 3.25: Tight gas full field cumulative gas recoveries for 3 coarsening ratios

3.5 Discussion

The formulation and application of pseudo steady state upscaling was presented in this chapter. Two different ways of setting up a PSS transmissibility upscaling calculation were discussed – PSSQ and PSSP. The advantage of using PSS concepts for upscaling was highlighted using two simple numerical examples where the steady state calculations failed in the presence of significant cross flow. On the other hand, the flow for PSS calculations was almost linear with less bias.

For the well index upscaling, PSSP upscaling was chosen as the default PSS algorithm based on equivalence between the PSSP method and the calculation performed by Peaceman 1990 both of which match the total flux across the computational boundary.

The PSS upscaling methodology was tested on a high contrast 2D model to evaluate the effectiveness of the local boundary conditions on the performance of the coarse model relative to the fine scale simulation. The results demonstrated improved performance of PSS upscaling methods relative to extended local upscaling without having to reference the large scale boundary conditions in a way the local-global upscaling method requires. . By construction, the superposition of PSS solutions gives back the SS

flow profile. Through the use of superposition, the fundamental flow fields studied allow for the capture of cross-flow in the upscaling calculation.

Both PSSQ and PSSP methods performed reasonably well for the 2D SPE10, 3D SPE10 low contrast and 3D tight gas examples. However, PSS method consistently underestimated the performance predictions for the high contrast 3D SPE10 model. This is due to the restrictive assumption that an entire coarse block reaches PSS even in the presence of weakly connected pay where it takes a long time for the pressure to equilibrate. Following King 2007, the assumption of pressure equilibrium inside a coarse block is violated in the presence of weakly connected or disconnected pay. For instance, consider a coarse cell pair upscaling as shown in Figure 3.26 with a weakly connected barrier in the middle of the upstream coarse block. The assumption of PSS in the entire volume for flow at the face leads to steep pressure gradient towards the left of the domain and biases the upscaled transmisisbilities downwards. In order to identify the sub volume that effectively contributes to the flow at the face, a pressure transient diffuse source upscaling approach is proposed in the following chapter.

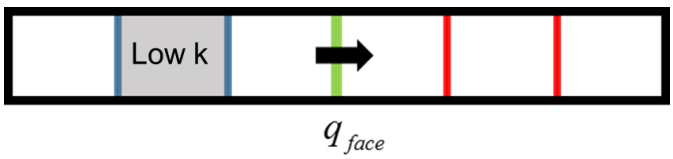

Figure 3.26: 1D PSS upscaling stranded pay issue

CHAPTER IV

DIFFUSE SOURCE UPSCALING*

In this chapter, the background elements needed to set up the pressure transient diffuse source (DS) upscaling algorithm are highlighted starting with the diffusive time of flight and asymptotic pressure approximation of the diffusivity equation.

4.1 Diffusive Time of Flight

The diffusive time of flight τ is obtained from the solution of the Eikonal equation which arises from the high frequency asymptotic limit of the diffusivity equation. Fourier transform of the slightly compressible diffusivity equation (Eq.(2.1)) to the frequency domain gives Eq.(4.1) as shown by Virieux et al. 1994.

$$\nabla \cdot \left(\vec{\vec{k}}(\vec{x}) \cdot \nabla \tilde{p}\left(\vec{x}, \omega\right) \right) = \phi\left(\vec{x}\right) \mu c_t \left(-i\omega\right) \tilde{p}\left(\vec{x}, \omega\right) \tag{4.1}$$

Based on an analogy with electromagnetic wave propagation, Vasco and Datta - Gupta 1999 and Kulkarni et al. 2001 proposed the solution of Eq.(4.1) to be of the form given in Eq.(4.2).

---

*Part of the data reported in this chapter is reprinted with permission from "Dynamic Downscaling and Upscaling in High Contrast Systems" by Nunna and King, 2017: Paper SPE-186289-MS presented at SPE Reservoir Simulation Conference held in Montgomery, Texas, USA, 20–22 February 2017. Copyright 2017, Society of Petroleum Engineers.

*Part of the data reported in this chapter is reprinted with permission from "Application of Pressure Transient Concepts for Improved Upscaling of Geologic Models" by Nunna 2017: Paper SPE-189293-STU presented at the SPE Annual Technical Conference and Exhibition held in San Antonio, Texas, USA, 9-11 October 2017. Copyright 2017, Society of Petroleum Engineers.

$$\tilde{p}\left(\vec{x},\omega\right)=e^{-\sqrt{-i\omega}\tau\left(\vec{x}\right)}\sum_{k=0}^{\infty}\frac{\tilde{A}_k\left(\vec{x}\right)}{\left(\sqrt{-i\omega}\right)^k} \tag{4.2}$$

The Eikonal equation (Eq.(4.3)) is obtained by substituting Eq.(4.2) in Eq.(4.1) and collecting the high frequency terms.

$$\nabla\tau\left(\vec{x}\right)\cdot\vec{\vec{k}}\left(\vec{x}\right)\cdot\nabla\tau\left(\vec{x}\right)=\phi\left(\vec{x}\right)\mu c_t \tag{4.3}$$

Here, $\tau\left(\vec{x}\right)$ is associated with the propagation of the first passage pressure pulse from an impulse source or sink. For a homogeneous isotropic media, the Eikonal equation simply relates τ to the distance (r) from a source through a proportionality constant given by hydraulic diffusivity (Eq.(4.4))

$$\tau=r\sqrt{\frac{\phi\mu c_t}{k}} \tag{4.4}$$

The Eikonal equation may be solved on a gridded mesh using the Fast Marching Method (FMM) (Sethian 1996) which is an extension of the well-known graph search algorithm Dijkstra (Dijkstra 1959). For the current work, Dijkstra's algorithm is considered as the additional angular resolution offered by FMM is not necessary for an upscaling calculation using two-point discretization.

4.2 Asymptotic Pressure Approximation

Collecting the high frequency limit of Eq.(4.2) and transforming back to the time domain shows that the time derivative of the pressure drop is proportional to an exponential kernel of the form ($\partial p/\partial t\sim e^{-\tau^2/4t}$) for which King et al. 2016, Wang et al.

2017 derived the asymptotic solutions to the diffusivity equation for various boundary inner and outer boundary conditions. In the current work, the fixed rate drawdown solution derived by King et al. 2016 is utilized. In this formulation, the diffusivity equation is written in terms of pressure and flux which are functions of τ and *t*. The flux is defined as the total flux across a τ contour. The asymptotic fixed rate draw-down solution is given by Eq.(4.5) where q_w is the flowrate at the wellbore and $V(t)$ refers to the time dependent drainage volume. The explicit form of the drainage volume is a consequence of material balance since $q = q_w$ at the wellbore, $\tau = 0$. The exponential approximation in this equation is exact for early time at any location, even in the presence of strong heterogeneity. This is a consequence of $\tau(\vec{x})$ being a solution to the Eikonal equation. The exponential term may be physically interpreted as an outwardly moving pressure transient. For sufficiently smooth heterogeneity, where reflection terms are negligible, this may provide an excellent approximation for all times. Notice as $t \to \infty, e^{-\tau^2/4t} \to 1$ for any finite τ, and $V(t) \to V_p$, we recover a PSS solution (Eq.(3.1)).

$$
\begin{aligned}
c_t \frac{\partial p}{\partial t} &= \frac{\partial q}{\partial V_p(\tau)} \approx -\frac{q_w}{V(t)} e^{-\tau^2/4t} \\
V(t) &= \int_0^\infty dV_p(\tau) \cdot e^{-\tau^2/4t} \approx \sum_{Cell,\, j} PV_j \cdot e^{-\tau_j{}^2/4t}
\end{aligned}
\tag{4.5}
$$

King et al. 2016 described the characteristics of the asymptotic fixed rate draw-down solution in terms of the time derivative of the pressure drop. These characteristics relate the range of the exponential term to the spatial profile of the solution (Figure 4.1and Table 4.1). Figure 4.1 describes the spatial footprint of the asymptotic pressure solution in

terms of the time derivative of the pressure drop normalized to its value at the wellbore $(\tau = 0)$. There are three important relationships between τ and t that can be obtained from the asymptotic solution which are also described in Figure 4.1. In the pressure transient literature, the depth of investigation (DOI) is defined as the time when $\partial p/\partial t$ reaches a maximum at a given location for an impulse source/sink (Lee 1982). Calculation of DOI involves the exponential term and a geometry dependent pre-factor which depends on the flow geometry. For instance, $\tau^2/4t_{DOI} = 1$ is the relationship for radial flow. Although this is the most common relationship, it does not directly enter the DS upscaling formulation. A second relationship is associated with the limit of detectability (LOD). This appears in the well testing literature in the context of the time at which you can detect the distance to a fault or the distance to the boundary of the reservoir through the well-test derivative (Lee 1982). This follows the relationship $\tau^2/4t_{LOD} = 4$ where the exponential reaches a value of $e^{-\tau^2/4t_{LOD}} = e^{-4} \cong 0.018$. This exponential is evaluated relative to unity in the context of LOD. In the diffuse source upscaling formulation it will be used to estimate those volumes that are still at near initial pressures at a given time. The last relationship is given at late time when $\tau^2/4t_{PSS} = 0.01$ and $e^{-\tau^2/4t_{PSS}} = e^{-0.01} = 0.99$. This limit is important in the well testing literature as the flow regimes (radial, linear, spherical) are apparent at the well once the PSS limit is reached in the vicinity of the wellbore. This is also the time at which the line source radial flow transient solution, given by the exponential integral function $E_i\left(\tau^2/4t\right)$, may be approximated by its logarithmic limit.

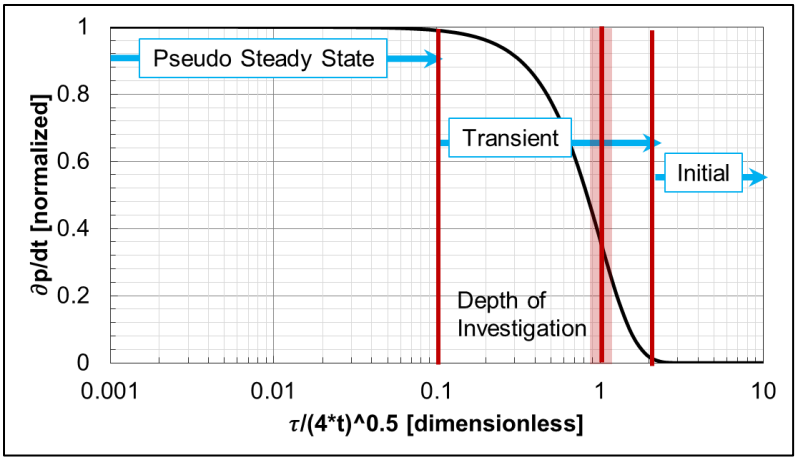

Figure 4.1: Spatial profile of the asymptotic pressure solution (After King et al. 2016)

Solution	Exponential Range	$\tau / \sqrt{4t}$ Range
PSS	$e^{-\tau^2/4t} > 0.99$	$\tau / \sqrt{4t} < 0.1$
Transient	$0.018 < e^{-\tau^2/4t} < 0.99$	$0.1 < \tau / \sqrt{4t} < 2$
Near Initial (Limit of Detectability)	$e^{-\tau^2/4t} < 0.018$	$\tau / \sqrt{4t} > 2$

Table 4.1: Solution characteristics of the asymptotic pressure approximation

King et al. 2016 derived a general form for the analytic solution for the equivalent 1D pressure profile using the asymptotic approximation described above. Its validity is limited to "sufficiently smooth" or early time solutions. In the current, the 3D diffusivity equation is solved numerically without the assumption that the spatial dependence of the pressure is only given by $\tau(\vec{x})$. However, the exponential form is retained as a diffuse source term as it provides a means to explore the transition from the initial pressure to the

long time pseudo steady state limit. It will be shown that of the three relationships described above, the diffuse source upscaling most strongly relies upon the Limit of Detectability, which is applicable even in the presence of strong heterogeneity

4.3 Diffuse Source Transmissibility Upscaling

Utilizing the asymptotic pressure approximation described above (Eq.(4.5)), the diffusivity equation is rewritten as Eq.(4.6) for implementing the diffuse source upscaling technique. This formulation was first proposed by Nunna 2014;Nunna et al. 2015 in the context of a tight gas reservoir upscaling problem.

$$\nabla \cdot \vec{u} \approx \pm \frac{q_{face}}{V(t)} \phi e^{-\tau^2/4t} \tag{4.6}$$

As is the case with PSS upscaling described in the previous chapter, the local flow in DS upscaling is driven by source/sink terms now in a transient sense. The strength of the local source and sink terms are proportional to $\phi e^{-\tau^2/4t}$. The diffusive time of flight to the center of each fine cell is obtained using Dijkstra's algorithm with the starting value $\tau = 0$ on the shared coarse cell face as shown in Figure 4.2.

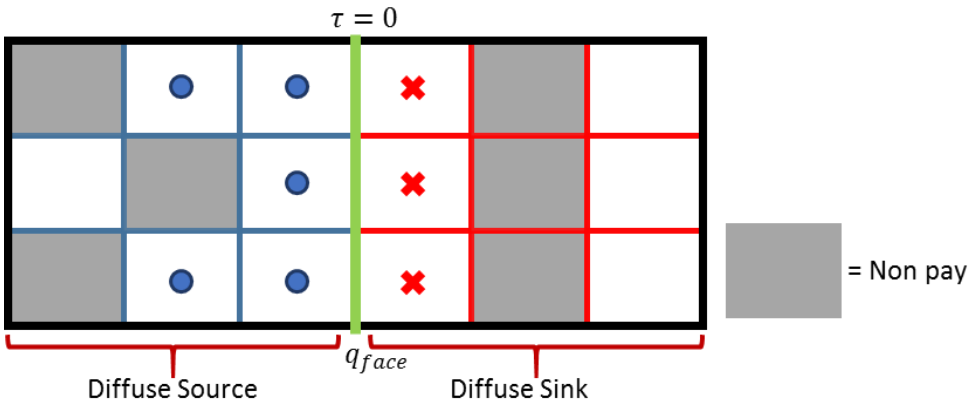

Figure 4.2: Diffuse source cell face drainage volume

In Figure 4.2, consider a pressure front moving away from the coarse cell face, only the fine cells connected to the face will have a finite value of τ. The construction naturally removes the non-pay (grey cells) and isolated pay from the drainage volume of the coarse cell face. The non-pay cells (grey) and disconnected cells have infinite time of flight, but the remaining cells have finite τ and will contribute to the upscaling calculation. Depending upon the time threshold chosen, this may also reduce the impact of low but non-zero values of permeability, making the results less sensitive to the choice of a net-pay cut-off. The calculation is local to the coarse cell face instead of being directly based upon all the fine cells. The application of local steady state or pseudo steady state upscaling techniques to Figure 4.2 would yield no flow as the center of the downstream coarse block is a barrier but the diffuse source approach can capture any finite flow local to the face. While the entire literature focused on expanding the computational domain to reduce the dependence on local boundary conditions for an upscaling calculation, the DS method tries to reduce the domain by working backwards from the flowing face.

The mathematics of the construction becomes apparent by examining a 1D homogeneous case, with a uniform cross section. From the asymptotic approximation, the flux function may be calculated analytically for the coarse cell pair with diffuse source and sink terms. The asymptotic approximation for uniform cross section w_{face} and $dV_p(\tau) = w_{face} \cdot d\tau$ reduces to Eq.(4.7).

$$\frac{\partial q}{\partial \tau} = -w_{face} \frac{q_{face}}{V(t)} e^{-\tau^2/4t} \tag{4.7}$$

At the upstream/downstream edge of the domain, the flux vanishes. Hence, $q = 0$ at $\tau = \tau_e$; τ_e is the diffusive time of flight to the edge of the volume. Integrating Eq.(4.7) to a finite τ gives Eq.(4.8).

$$\int_0^{q(\tau,t)} dq = -w_{face} \frac{q_{face}}{V(t)} \int_{\tau_e}^{\tau} e^{-\tau^2/4t} d\tau \tag{4.8}$$

After algebraic manipulation, the analytic flux function is given below.

$$q(\tau,t) = q_{face} \sqrt{\pi t} \frac{w_{face}}{V(t)} \left\{ erf\left(\frac{\tau_e}{2\sqrt{t}}\right) - erf\left(\frac{\tau}{2\sqrt{t}}\right) \right\} \tag{4.9}$$

Evaluating $V(t)$ for a uniform cross section in a bounded domain with upper limit τ_e gives Eq.(4.10)

$$V(t) = \sqrt{\pi t} w_{face} erf\left(\frac{\tau_e}{2\sqrt{t}}\right) \tag{4.10}$$

Substituting Eq.(4.10) in Eq.(4.9) and normalizing by q_{face} gives the flux basis function as a function of position (τ) and time.

$$\hat{q}_0(\tau,t) = 1 - erf\left(\frac{\tau}{2\sqrt{t}}\right) \Big/ erf\left(\frac{\tau_e}{2\sqrt{t}}\right) \tag{4.11}$$

At long time limit i.e. at PSS $(t \to \infty)$, Eq.(4.11) becomes a linear function of τ given by Eq.(4.12). The flux profile at PSS has reduced to Raviart and Thomas 1977 basis whereas for steady state, the flux is uniform throughout the domain.

$$\hat{q}_0(\tau) = 1 - \tau/\tau_e \tag{4.12}$$

Eq.(4.11) is graphically presented in Figure 4.3 for a 1D homogeneous cell pair. The arrow shows the direction of fluid flow. For early time, the flux vanishes except near the coarse cell face, and an upscaling calculation will emphasize only those cells near the face. In the late time limit at PSS, the flux function will be a simple linear function which is a finite element RT0 basis. In 3D and with heterogeneity, the flux function is more complicated and will need to be determined numerically.

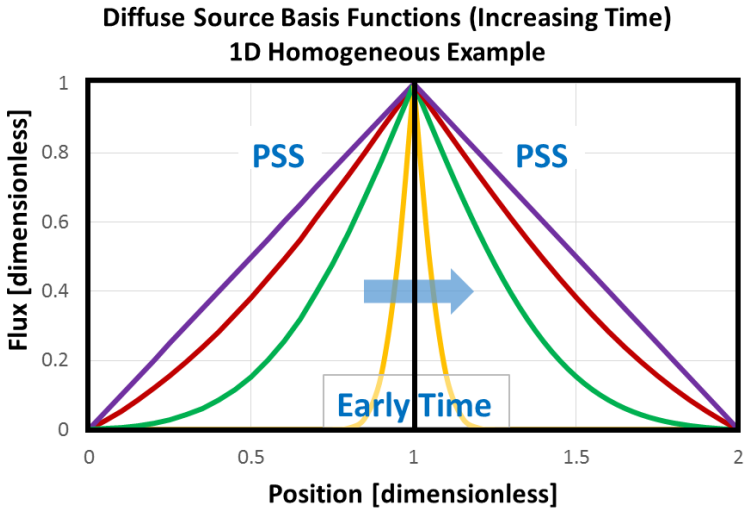

Figure 4.3: 1D Homogeneous diffuse source flux profile for a cell pair (Reprinted with permission from Nunna 2017)

Similar to the two PSS upscaling methods exposed in the previous chapter, the DS upscaling method also has two choices of specifying the upstream and downstream boundary conditions namely DSQ and DSP. In fact, PSS upscaling is a subset of the more general DS formulation for a particular choice of time. The source/sink terms for the diffuse source upscaling technique are evaluated at a specified time which will be discussed in the following section. After specifying time, Eq.(4.6) is discretized and the pressures are solved numerically. Then, the effective transmissibility for DSQ and DSP methods is obtained using the pressure averaging procedure (Eq.(3.4) and Eq.(3.6)). The near well upscaling formulation using the diffuse source methodology is very similar to the PSS well index formulation discussed in the previous chapter (Figure 3.11). The only difference for the DS method is that the diffusive time of flight is evaluated from the perforated cells ($\tau = 0$) with source terms scaled as per $\phi e^{-\tau^2/4t}$ instead of ϕ.

4.3.1 Selection of Time

The purpose of a non-net cutoff is to discard those portions of a reservoir description that do not contribute to recovery or to the reservoir energy. A good cutoff is one where the gross quantities of interest, e.g., transmissibility or gross permeability or gross porosity do not vary significantly when the cutoff is varied. The exponential term can distinguish between the net and non-net cells, according to the value of τ. For a finite τ at a large but finite time, $\phi e^{-\tau^2/4t} \to \phi$. These are the net cells. However, low permeability cells have a large value for τ, so that at a large but finite time $\phi e^{-\tau^2/4t} \to 0$.

An upscaling calculation has potentially very wide range of τ values. Since τ is a surrogate for pressure, an average τ value for the region is defined using the effective pore volume (PV) weight.

$$\bar{\tau} = \sum_i PV_i e^{-\tau_i^2/4t} \tau_i \Big/ \sum_i PV_i e^{-\tau_i^2/4t} \tag{4.13}$$

In order to characterize the transient, τ average should be evaluated at a time which the system is still infinite acting. This gives a relation for time at which the outer boundary is first detected approximated by $2\bar{\tau}$. This is the limit of detectability (LOD) of the outer boundary given by: $\left(2\bar{\tau}\right)^2 / 4t_{LOD} = 4$ (Table 4.1). Using $t = t_{LOD}$ in Eq.(4.13) gives Eq.(4.14) which is a non-linear equation for $\bar{\tau}$ that can be solved by successive substitution or simple bisection between $\tau_{\max}$ and $\tau_{\min}$.

$$\bar{\tau} = \sum_i PV_i e^{-\tau_i^2/\bar{\tau}^2} \tau_i \Big/ \sum_i PV_i e^{-\tau_i^2/\bar{\tau}^2} \tag{4.14}$$

Eq.(4.14) reduces to $\tau_{\min}$ as $\bar{\tau} \to 0$ and the usual pore volume weighted average as $\bar{\tau} \to \infty$. Therefore, the solution is bounded between $\tau_{\min}$ and the pore volume weighted average. At low values of $\bar{\tau}$, there is a possibility of the ratio becoming $0/0$. Hence for the sake of implementation, Eq.(4.14) is modified as Eq.(4.15) by multiplying both numerator and denominator by $e^{\tau_{\min}^2/\bar{\tau}^2}$. This guarantees at least one cell has a non-zero source term.

$$\bar{\tau} = \sum_i PV_i e^{-\left(\tau_i^2 - \tau_{\min}^2\right)/\bar{\tau}^2} \tau_i \Big/ \sum_i PV_i e^{-\left(\tau_i^2 - \tau_{\min}^2\right)/\bar{\tau}^2} \tag{4.15}$$

Following the discussion of Table 4.1, once $\tau_i > 2\bar{\tau}$, the contribution to the reservoir energy within the upscaling region is negligible. This provides a natural definition for non-net. In the analysis of the dynamics of the upscaling calculation, a range of times is considered to evaluate the impact of time selection on the upscaled property (permeability or transmissibility). Once a $\bar{\tau}$ is obtained, the range of times to be examined is based on the following relationships to a characteristic time, given by the ratio $\bar{\tau}^2/4$.

- Divide by 4 to get the "near initial" time (exponential $< 1.8\%$)
- Multiple by 10 to get the onset of approximate PSS (exponential > 0.9)
- Multiple by 100 to get the PSS limit (exponential > 0.99)

To have more information within the transient period, the range of times specified in Table 4.2 are chosen to evaluate the impact of time selection on the upscaled property.

Solution	Time: t	Exponential: $e^{-\bar{\tau}^2/4t}$
PSS	∞	1.00
PSS Limit	$100\left(\bar{\tau}^2/4\right)$	0.99
Approximate PSS	$10\left(\bar{\tau}^2/4\right)$	0.90
Characteristic Time	$\left(\bar{\tau}^2/4\right)$	0.37
Near Initial	$\left(\bar{\tau}^2/4\right)/4$	0.018

Table 4.2: Range of times chosen for the time sensitivity study and the corresponding solution characteristics

Now, two local upscaling examples are presented, one with a high contrast permeability field and the other with a relatively low contrast in properties. The choice of time will impact the volume support for the upscaling calculation. At any time, the drainage volume fraction is given by the ratio of drainage volume to the total pore volume of the system.

$$Drainage\,Volume\,Fraction = \frac{V(t)}{V_p} = \frac{\sum_i PV_i e^{-\tau_i^2/4t}}{\sum_i PV_i} \tag{4.16}$$

The impact of time selection is analyzed through a cross plot of effective permeability and the drainage volume fraction. Here, the effective link permeability is obtained by scaling out the geometry from the effective transmissibility. For the sake of brevity, only DSQ calculation is evaluated.

High Contrast System

Figure 4.4 shows the permeability, porosity distribution for a $3\times3\times1$ coarse cell pair. The contrast in permeability between the two coarse cells is over four orders of magnitude. The higher permeability cells have a lower diffusive time of flight and vice-versa. Figure 4.5 shows the visualization of the exponential weights at different choices of time. This displays the drainage volume evolution with time, moving outwards from the coarse cell interface. Observe the volume support increasing as the time is increased. At PSS $(t\to\infty)$, the entire pore volume contributes to the calculation of the effective permeability.

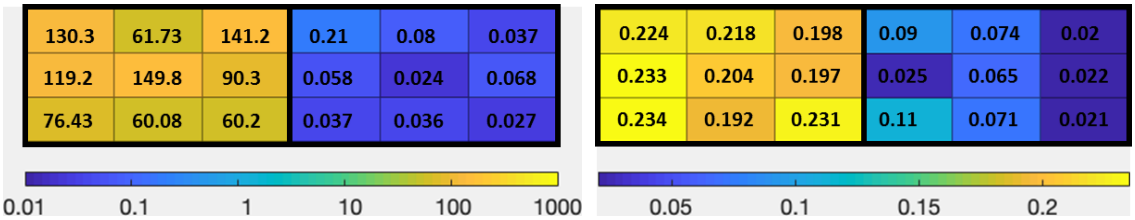

(a) Permeability (md) **(b) Porosity**

Figure 4.4: High contrast cell pair upscaling properties

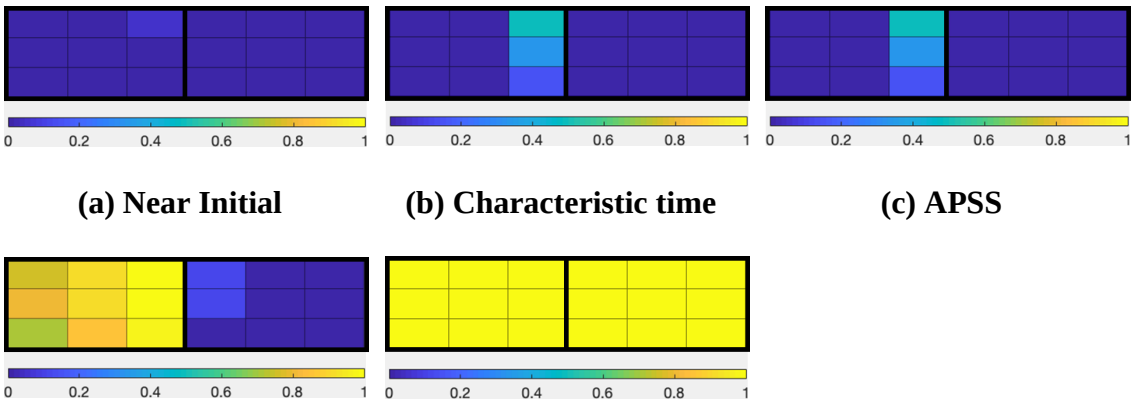

(a) Near Initial **(b) Characteristic time** **(c) APSS**

(d) PSS Limit **(e) PSS**

Figure 4.5: Evolution of drainage volume for the high contrast case

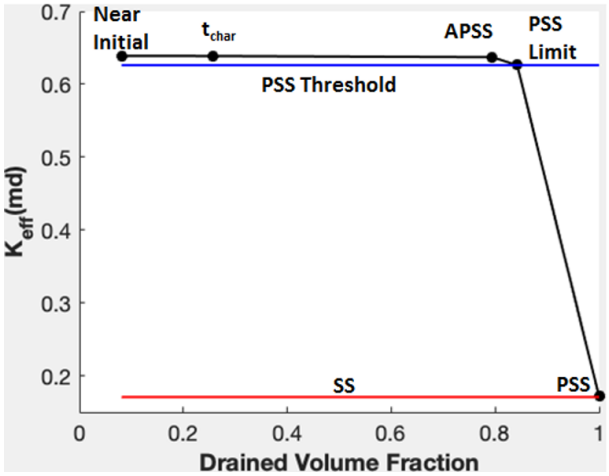

Figure 4.6: Effective permeability vs drainage volume fraction for the high contrast case

The cross plot between the upscaled permeability and the drainage volume fraction (Figure 4.6) shows that the permeability has stabilized between the near initial time and the PSS limit. The lower permeability cells on the right start contributing only at the PSS Limit and at this point, 85% of the pore volume is drained. However, when $t \to \infty$, to

reach PSS, source and sink terms are placed in cells that will not contribute to flow until a very large time. These terms induce high pressure gradients and lower the effective permeability. In contrast, at any finite time, including large but finite times, the volume contributing to flow from the downstream coarse cell has negligible support leading to an increased permeability compared to PSS. Notice the steady state effective permeability is also close to the PSS value as a consequence of superposition.

Low Contrast System

Figure 4.7 shows the permeability and porosity for a low contrast $3\times3\times1$ coarse cell pair with relatively higher permeabilities compared to the high contrast case. The drainage volume visualization (Figure 4.8) now shows that cells in both coarse blocks start responding by characteristic time, which was not the case in the high contrast example. The high permeability cell right at the face starts responding even at near initial time which is expected. The evolution of effective permeability (Figure 4.9) shows similar trend compared to the high contrast case. However, both PSS limit and PSS are exactly the same indicating the assumption of PSS in this region is valid. The steady state approach may not be bad in this case because of low contrast and relatively high permeability. While there was a 100% increase in effective permeability values between PSS and PSS limit in the high contrast case, there is no difference when there is minimal contrast.

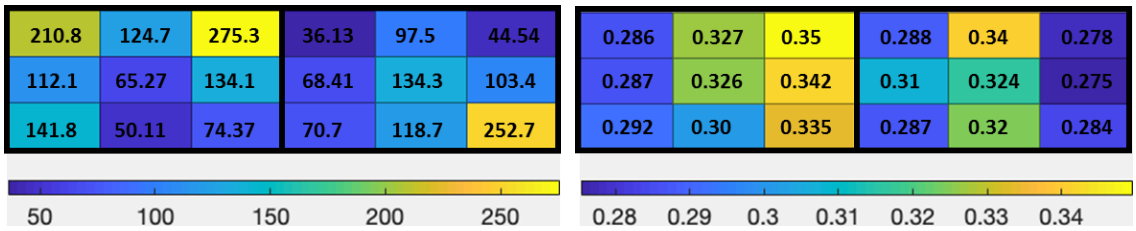

(a) Permeability (md) **(b) Porosity**

Figure 4.7: Low contrast cell pair upscaling properties

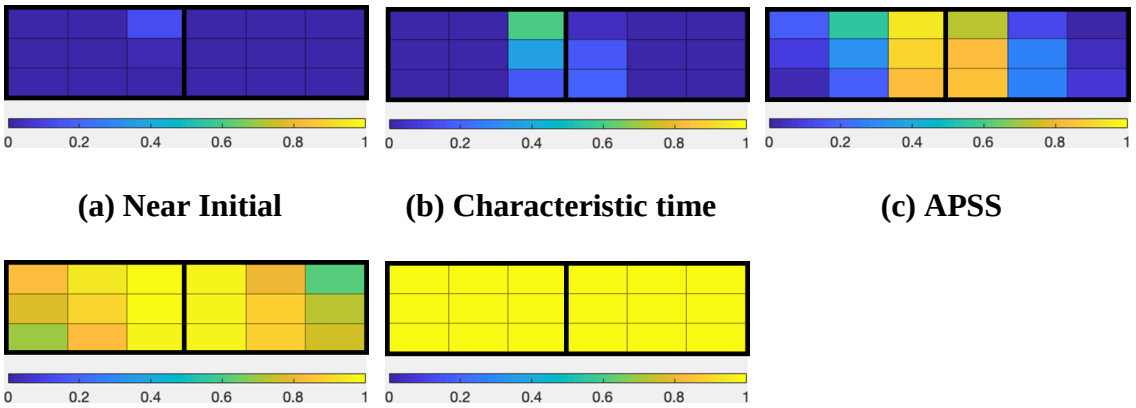

(a) Near Initial **(b) Characteristic time** **(c) APSS**

(d) PSS Limit **(e) PSS**

Figure 4.8: Evolution of drainage volume for the low contrast case

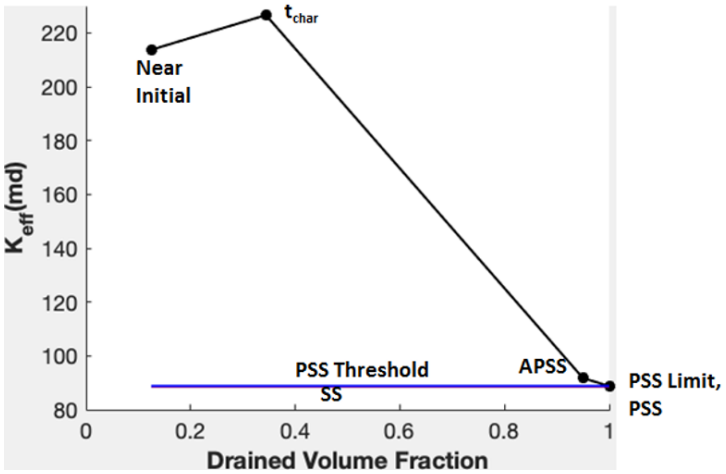

Figure 4.9: Effective permeability vs drainage volume fraction for the low contrast example

Impact of the Net/Non-Net Cutoff

In this section, the impact of the low permeability cells in the high contrast system is explored by modifying the initial reservoir model through the use of a non-net cutoff on the fine scale permeability. Following the depletion pattern in Figure 4.5d, only two cells in the downstream coarse block are considered to be pay, and the porosity is set to zero in the other cells. The permeability field and the corresponding upscaled results are shown in Figure 4.10. It is clear that now the PSS value is not a bad estimate of the permeability: due to the imposed non-net cutoff, the coarse cell face is responding only to the connected high permeability volume even at infinite time. The steady state effective permeability is also closer to the diffuse source upscaling result due to the absence of high contrast in the system compared to the previous case. For SS, the pressure boundary condition for the downstream coarse cell is imposed in the first column instead of the outer boundary which otherwise would yield no-flow. Notice that the value of effective permeability obtained

here (Figure 4.10b) matches closely with the PSS limit value in the case without cutoff (Figure 4.6). From this, a conclusion may be drawn that the transient formulation allows to capture the well connected sub-volume(s) without the need to introduce any explicit non-net cutoffs.

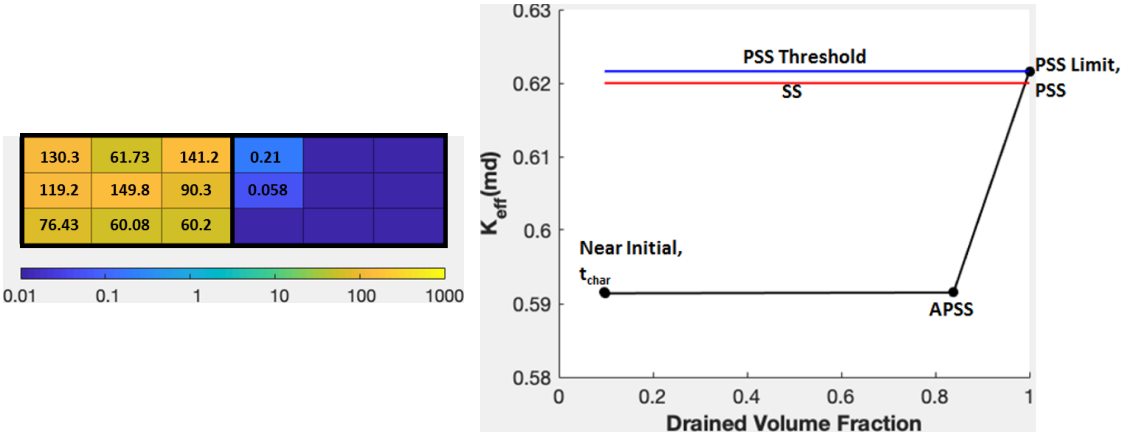

(a) Permeability **(b) Effective permeability vs Drainage Volume Fraction**

Figure 4.10: Impact of non-net cutoff on the high contrast case

Once the PSS limit has been selected as a representative time for the DS upscaling calculation, the source and sink strengths can be examined in more detail. A significant difference between this large but finite time, and an infinite time, only arises if there are sub-volumes that have not depleted by the PSS limit: these are those cells that are beyond the limit of detectability at t_{PSS}. Specifically, a distinction can be made between those cells that have not depleted from those that do deplete, by replacing the exponential weights with a value of 0 or 1 at the threshold of the limit of detectability as described in Eq.(4.17)

.

$$e^{-\tau_i^2/4t_{PSS}} = \begin{cases} 1 & if \quad \tau_i^2/4t_{PSS} < 4 \\ 0 & otherwise \end{cases} \tag{4.17}$$

The interpretation of the threshold is that only the volumes that are well-connected to the coarse face reach PSS whereas any weakly connected volumes do not. The threshold is chosen based on limit of detectability (LOD) at a time equal to the PSS limit. The results of using this "PSS Threshold" are shown in the above figures for the three cases studied, where they give values close to the PSS limit. This approach also has a conceptual advantage over the use of the full exponential as a source or sink term, as the asymptotic approximation is only valid at times earlier than the limit of detectability. In the form of this threshold, only those sub-volumes where the exponential term is valid retain a dependence on τ.

4.3.2 2D Diffuse Source Transmissibility Example

A 2D example is presented to summarize the diffuse source approach with a DSQ example (Figure 4.11).

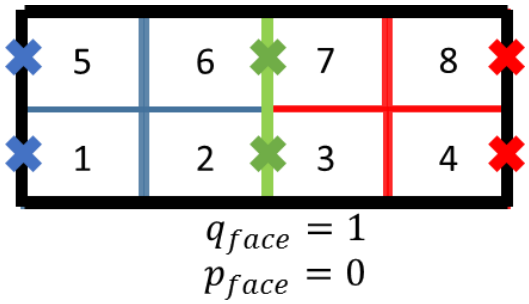

Figure 4.11: 2x2 DSQ upscaling example

The discrete equations for the upstream fine cells are given by Eq.(4.18). T_{ij}, here represents the fine scale intercell transmissibility between block i and block j, and PV_i represents the pore volume of grid block i.

$$
\begin{aligned}
&T_{12}(p_1-p_2)+T_{15}(p_1-p_5)=\mu q_{face}\left(PV_1e^{-\tau_1^2/4t}\Big/\sum_{i=1,2,5,6}PV_ie^{-\tau_i^2/4t}\right)\\
&T_{12}(p_2-p_1)+T_{26}(p_2-p_6)+2T_{23}(p_2-p_{face})=\mu q_{face}\left(PV_2e^{-\tau_2^2/4t}\Big/\sum_{i=1,2,5,6}PV_ie^{-\tau_i^2/4t}\right)\\
&T_{56}(p_5-p_6)+T_{15}(p_5-p_1)=\mu q_{face}\left(PV_5e^{-\tau_5^2/4t}\Big/\sum_{i=1,2,5,6}PV_ie^{-\tau_i^2/4t}\right)\\
&2T_{67}(p_6-p_{face})+T_{26}(p_6-p_2)+T_{56}(p_6-p_5)=\mu q_{face}\left(PV_6e^{-\tau_6^2/4t}\Big/\sum_{i=1,2,5,6}PV_ie^{-\tau_i^2/4t}\right)
\end{aligned}
\tag{4.18}
$$

The discretized equations for the downstream grid blocks are given by Eq.(4.19). The negative sign on the right hand side indicates sink terms.

$$
\begin{aligned}
&2T_{23}(p_3-p_{face})+T_{34}(p_3-p_4)+T_{37}(p_3-p_7)=-\mu q_{face}\left(PV_3e^{-\tau_3^2/4t}\Big/\sum_{i=3,4,7,8}PV_ie^{-\tau_i^2/4t}\right)\\
&T_{34}(p_4-p_3)+T_{48}(p_4-p_8)=-\mu q_{face}\left(PV_4e^{-\tau_4^2/4t}\Big/\sum_{i=3,4,7,8}PV_ie^{-\tau_i^2/4t}\right)\\
&2T_{67}(p_7-p_{face})+T_{78}(p_7-p_8)+T_{37}(p_7-p_3)=-\mu q_{face}\left(PV_7e^{-\tau_7^2/4t}\Big/\sum_{i=3,4,7,8}PV_ie^{-\tau_i^2/4t}\right)\\
&T_{78}(p_8-p_7)+T_{48}(p_8-p_4)=-\mu q_{face}\left(PV_8e^{-\tau_8^2/4t}\Big/\sum_{i=3,4,7,8}PV_ie^{-\tau_i^2/4t}\right)
\end{aligned}
\tag{4.19}
$$

To complete the set of equations, a gauge condition of uniform zero face pressure is specified. In setting the face pressure to be an isobar, the pressure field is effectively solved one coarse block at a time. Also notice that the transmissibility expressed with respect to the face pressure is twice the intercell transmissibility. For DSP upscaling

approach two additional equations are required to impose the outer faces as isobars (Eq.(3.5)).

The system of equations depends upon a specified time t, chosen based on the approach to the PSS limit. First a $\bar{\tau}$ is calculated for the upstream and downstream coarse blocks using Eq.(4.14) and then the maximum of the two $\left(\bar{\tau} = \max\left(\bar{\tau}_{up}, \bar{\tau}_{down}\right)\right)$ is obtained. Based on this, a large but finite time is determined from the approach to the PSS limit $\left(t = t_{PSS} = 100 * \bar{\tau}^2 / 4\right)$ and then threshold the exponential weights to 0 or 1 based on Eq.(4.17). After solving for the pressures, the reference diffuse source pressure drop for transmissibility is calculated based on Eq.(4.20) .Here, the transmissibility T refers to the intercell or half-cell transmissibility along the outer fine cell faces of the two coarse cells.

$$\Delta p_{DS} = \frac{p_1 T_1 + p_5 T_5}{T_1 + T_5} - \frac{p_4 T_4 + p_8 T_8}{T_4 + T_8} \tag{4.20}$$

The intercell transmissibility is used for cell faces which are internal to the 3D reservoir model. Half cell transmissibility is only used for the external boundaries of the model. The upscaled transmissibility is given by:

$$\frac{1}{T^{Eff}} = \frac{\Delta p_{DS}}{\mu q_{face}} \tag{4.21}$$

Notice that the face flux and viscosity scale out of the transmissibility calculation since the pressure drops are proportional to μq_{face}. Therefore, a unit value for this combination is imposed while implementing the algorithm.

Before moving on to the numerical experiments for the upscaling calculations, a downscaling exercise is presented using the diffuse source formulation to motivate its usage for the multiscale simulation.

4.4 Diffuse Source Downscaling

The downscaling is performed using a reference fine scale simulation model i.e., the coarse fluxes are obtained using the fine scale simulation instead of running a pressure solve on the coarse grid. This is done only to validate the proposed formulation as a downscaling exercise. The coarse fluxes are obtained by summing up the fine scale face fluxes to the resolution of the coarse grid.

For the DS approach, the coarse flux is downscaled using the transient formulation (Eq.(4.6)) with the exponential term replaced by the PSS/LOD threshold, to obtain the velocity field (Figure 4.12). Notice, the approach employed here is DSQ, not DSP. The DSP approach results in a flux discontinuity at the shared faces due to an imposed isobar. The coarse flux is continuous, however the fine scale fluxes are not. For DSQ approach the downscaling is trivial since the entire outer boundary is treated as no-flow allowing seamless superposition to obtain mass conservative fine scale velocity field.

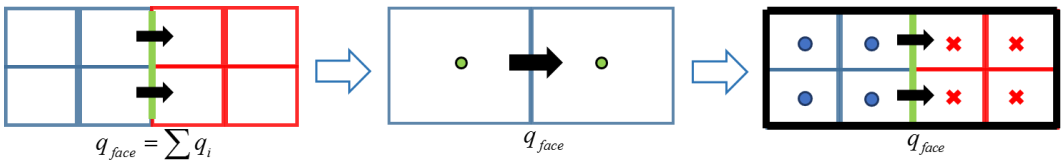

Figure 4.12: Diffuse source (DSQ) downscaling validation workflow

.

For the steady state approach, half-cell steady state formulation is utilized with pressure isobars at the centers of the respective coarse blocks. Since the equations are linear with no source/sinks (Eq.(1.1)), the pressure isobars are rescaled to match the coarse flux to obtain the local velocity field (Figure 4.13). Here, the fluid enters halfway through the upstream block and leaves halfway from the downstream block. The global velocity field is then obtained by superposition. This formulation by construction has flux discontinuity at the coarse cell centers. Møyner and Lie 2014b proposed a localization scheme for this approach to generate continuous mass conservative velocity fields. However, this is not considered in the current work.

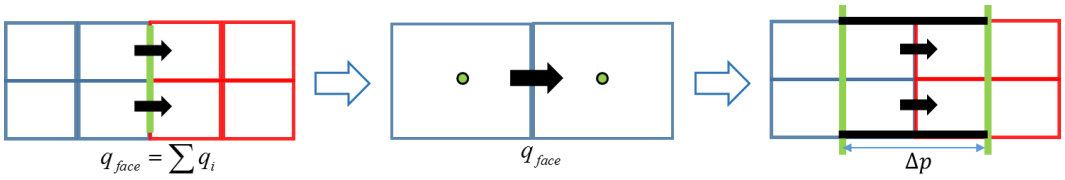

Figure 4.13: Steady state downscaling validation workflow

The downscaling workflow is tested on SPE10 top and bottom layers with an injector-producer pair at the corners (Figure 4.14). The coarsening ratio is $3\times3\times1$. The injector and producer are maintained at a constant bottomhole pressure of 10,000 psia and 4,000 psia respectively. The rock and single phase oil compressibility are left to the default values of the original SPE10 data set.

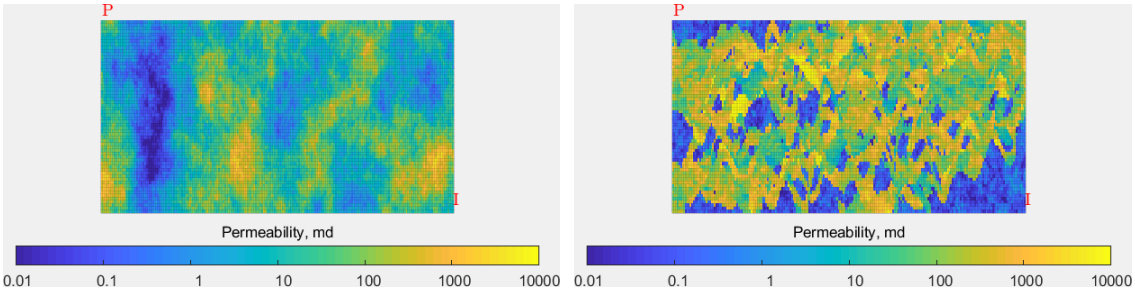

(a) Top layer **(b) Bottom layer**

Figure 4.14: Permeability of the top and bottom layers of SPE10

The downscaled velocity field is compared at a simulation time of 1 month. Figure 4.15 represents the velocity profile for the top layer. The range of the color scale is adjusted to be the same for the difference in velocities for the two approaches. The steady state downscaling approach consistently underestimates the total velocities while the DS formulation clearly has fewer biases. The largest discrepancy can be seen at the location of the wells, where the total velocities are the largest. The difference is more pronounced in the bottom layer (Figure 4.16) where there is higher contrast in properties compared to the top layer. Again, the diffuse source downscaling approach consistently reduces the biases introduced by steady state upscaling. Although the application shown here is for compressible flow, the same formulation may be utilized to simulative multiscale incompressible flow as demonstrated in Nunna et al. 2018.

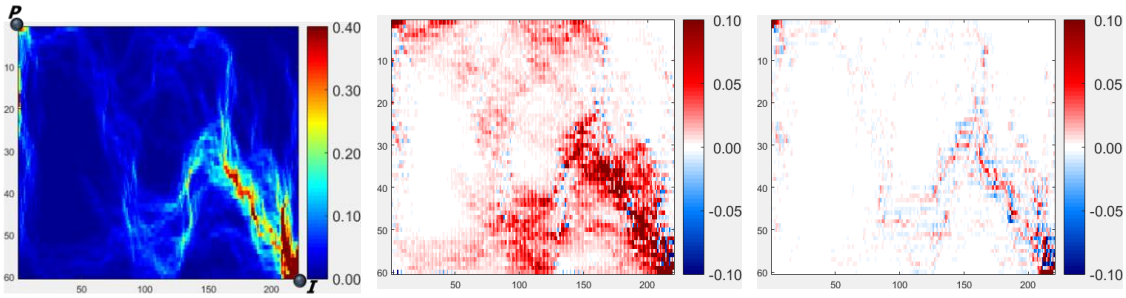

(a) **(b)** **(c)**

Figure 4.15: Total velocity profile of SPE10 top layer at 1 month, (a): Fine scale velocity, (b): SS velocity error, (c): DS velocity error

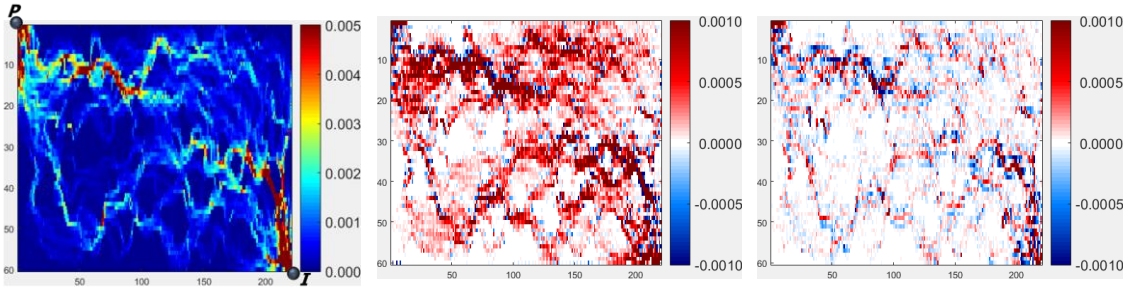

(a) **(b)** **(c)**

Figure 4.16: Total velocity profile of SPE10 bottom layer at 1 month, (a): Fine scale velocity, (b): SS velocity error, (c): DS velocity error

4.5 Numerical Experiments

The DS upscaling method is tested on the models described in the PSS upscaling chapter with some additional test cases.

4.5.1 3D SPE10 Single Phase Flow

The model and simulation input information are given in Figure 3.19 and Table 3.4 respectively. The well performance predictions are described in Figure 4.17 where the DSQ method consistently out performs the remaining upscaling algorithms. Figure 4.18 describes the face flux comparisons at the end of simulation. For the sake of brevity, the PSS plots are omitted and also $2\times2\times2$ resolution is not shown. The reader is advised to look at Figure 3.22 for PSS face flux comparisons. However, Table 4.3 provides a comprehensive summary of the face flux errors for all the tested upscaling methods. Both Figure 4.18 and Table 4.3 show that the DS methods consistently give superior coarse scale descriptions relative to steady state or pseudo steady state methods. Although the DSP method overestimates the well rates, it fares well in terms of the face flux comparisons. The overall effectiveness of the diffuse source upscaling methods relative to steady state and pseudo steady state methods on the high contrast SPE10 model is due to the fact that they can effectively capture the subgrid heterogeneity that contributes to the flow (i.e., reaches PSS) in a local upscaling calculation.

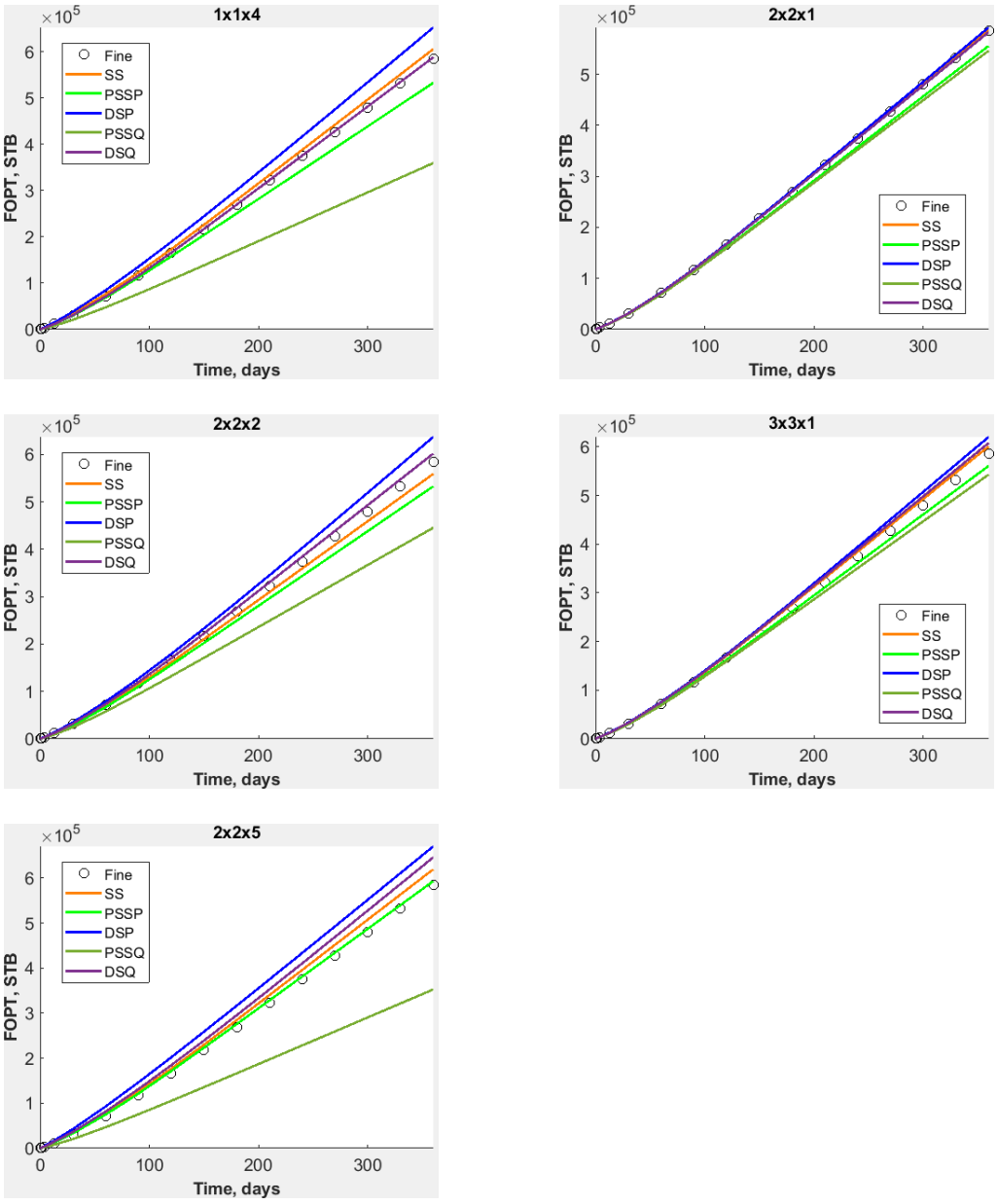

Figure 4.17: SPE10 single phase flow cumulative oil recovery for different coarsening ratios

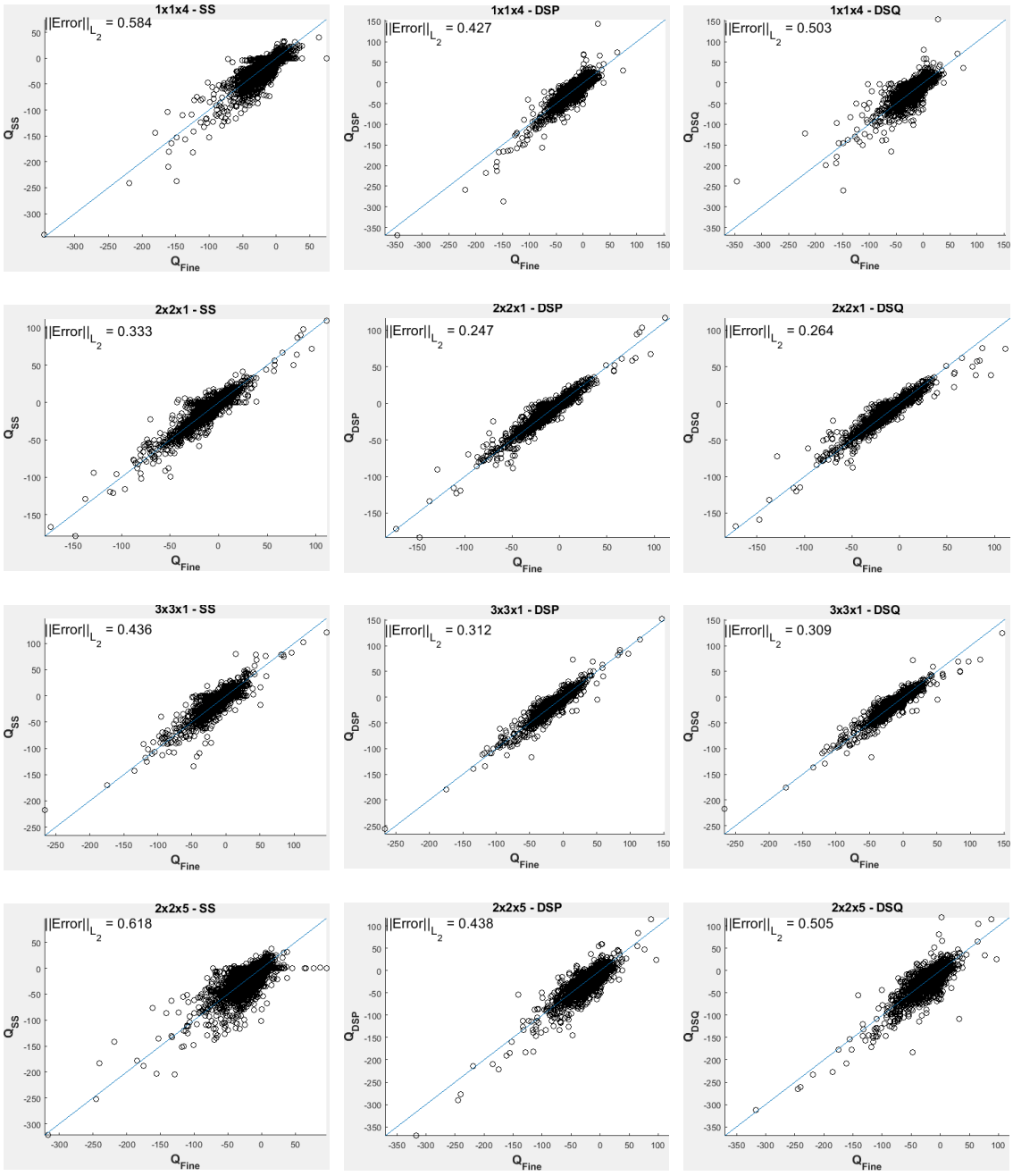

Figure 4.18: SPE10 single phase flow face flux comparisons for different coarsening ratios

	1×1×4	2×2×1	2×2×2	3×3×1	2×2×5
SS	0.584	0.333	0.460	0.436	0.618
PSSP	0.559	0.362	0.485	0.418	0.613
PSSQ	0.634	0.374	0.514	0.440	0.646
DSP	0.427	0.247	0.372	0.312	0.438
DSQ	0.503	0.264	0.355	0.309	0.505

Table 4.3: SPE10 single phase flow face flux errors for different coarsening ratios

4.5.2 2D SPE10 Two Phase Flow

In this section, the DS upscaling methods are tested for two phase flow (oil, water) scenario. The initial coarse relative permeabilities were obtained using pore volume averaged fine scale initial water saturations. Two 2D cases are considered: a low contrast layer 1 and a high contrast layer 68 of SPE10 model (Figure 4.19). The coarsening ratio chosen is $3\times3\times1$ and the simulation time is 5 years. The fluid, rock and well configurations were left to the default values of the SPE10 dataset.

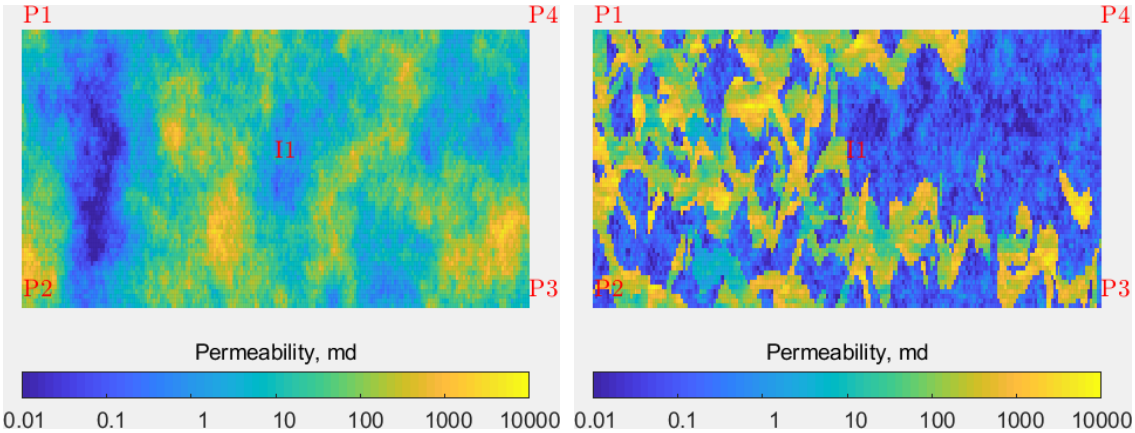

(a) Layer 1 **(b) Layer 68**

Figure 4.19: SPE10 permeability map for layers 1, 68 with one central injector and four producers

Figure 4.20 describes the layer 1 cumulative oil production and water cut for the 4 producers showing almost identical response for all the upscaling methods. Although the oil rates are accurate, some difference can be seen in the water cut response at wells P1, P2 and P4. The face flux comparison at the end of simulation also show similar errors for the tested upscaling methods (Figure 4.21). Figure 4.22 shows the water saturation (Sw) error maps at the end of simulation also showing similar spatial error for all the upscaling methods. The coarse water saturation is uniformly mapped on to the fine cells within the coarse block making the coarse water saturation at the same resolution at the fine scale water saturation. The similarity of the results for layer 1 may be due to the low contrast in reservoir properties which is not the case for layer 68.

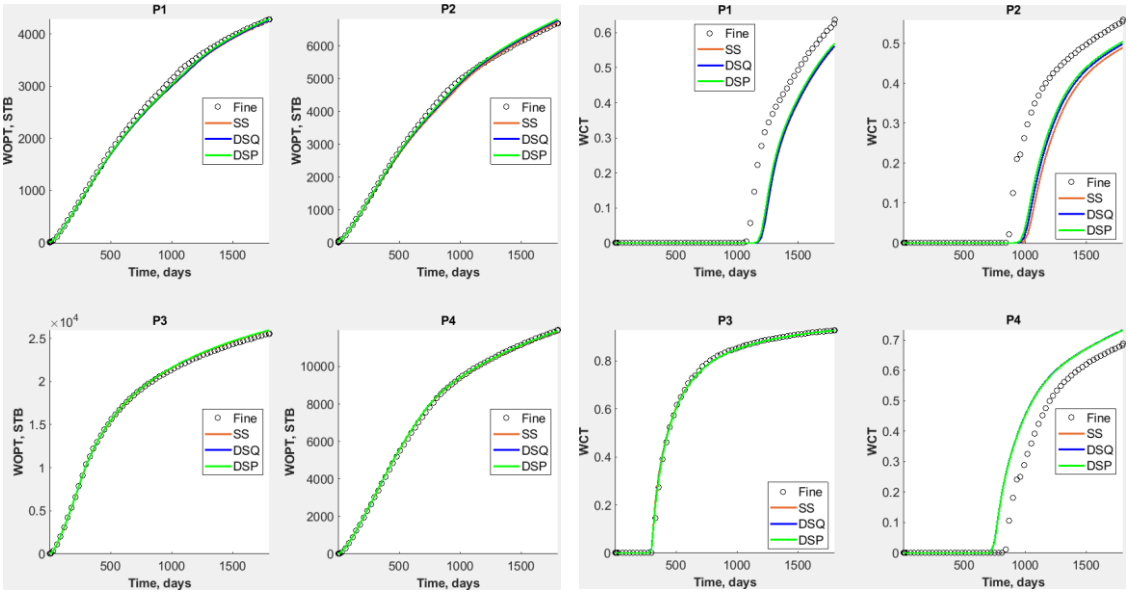

(a) Cumulative oil production **(b) Producer water cut**

Figure 4.20: SPE10 layer 1 two phase flow producer cumulative oil volumes and water cut

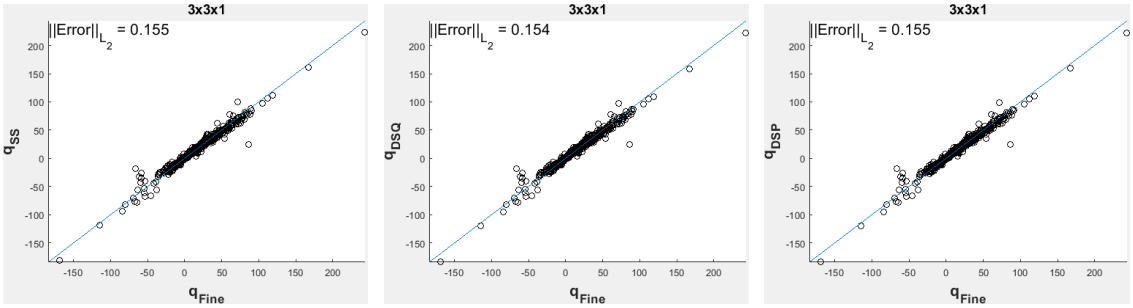

(a) Steady state **(b) DSQ** **(c) DSP**

Figure 4.21: Face flux comparisons at the end of simulation for SPE10 layer 1 two phase flow

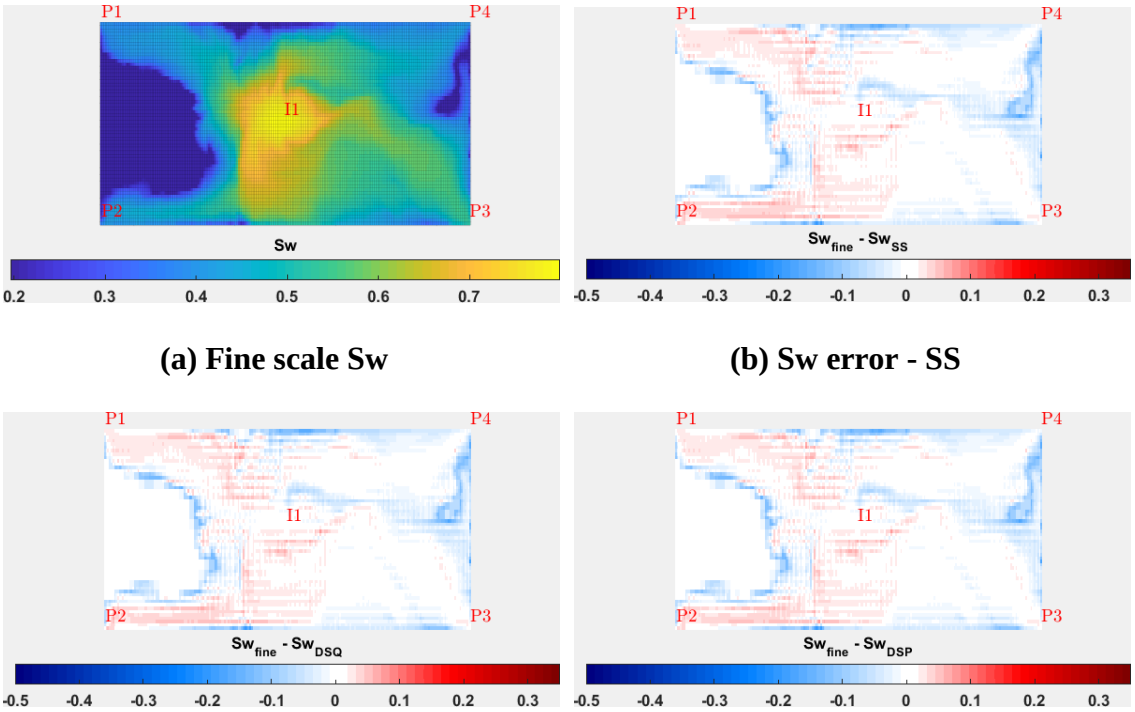

(a) Fine scale Sw **(b) Sw error - SS**

(c) Sw error - DSQ **(d) Sw error - DSP**

Figure 4.22: SPE10 layer 1 two phase flow water saturation error maps at the end of simulation

Layer 68 is cited as one of the most challenging layers of SPE10 with highly heterogeneous channelized flow features (Efendiev and Hou 2009). Figure 4.23 shows the oil volumes and water cut response for the producers. Producers P3 and P4 did not experience water breakthrough in all the models. Hence, their response is not plotted. Although the performance predictions are not as accurate as the previous case, both DSQ and DSP methods give relatively better oil volume prediction compared to steady state upscaling. In terms of the face flux comparison at the end of simulation, DSP methods has the least error followed by DSQ and steady state upscaling (Figure 4.24). The water saturation error maps also show that both DSP and DSQ upscaling methods exhibit less

error compared to steady state upscaling. The superior performance of the DS methods relative to steady state may due to the fact that the assumption of pressure equilibrium inside a coarse block is well accounted for in the DS methods and not in the steady state upscaling. However, a significant source of error for all the single phase upscaling methods may be due to multiphase issues where one single coarse pressure may not capture the fine scale water front movement. Such cases may be better handled by a multiscale simulator when there is a high velocity variance inside a coarse block.

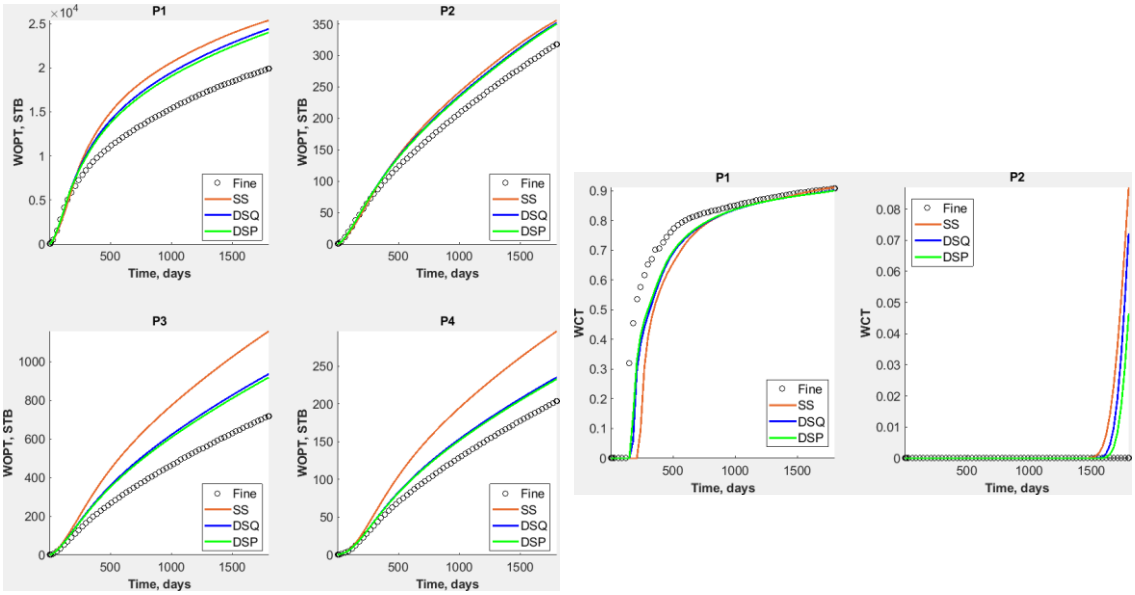

(a) Cumulative oil production **(b) Producer water cut**

Figure 4.23: SPE10 layer 68 two phase flow producer cumulative oil volumes and water cut

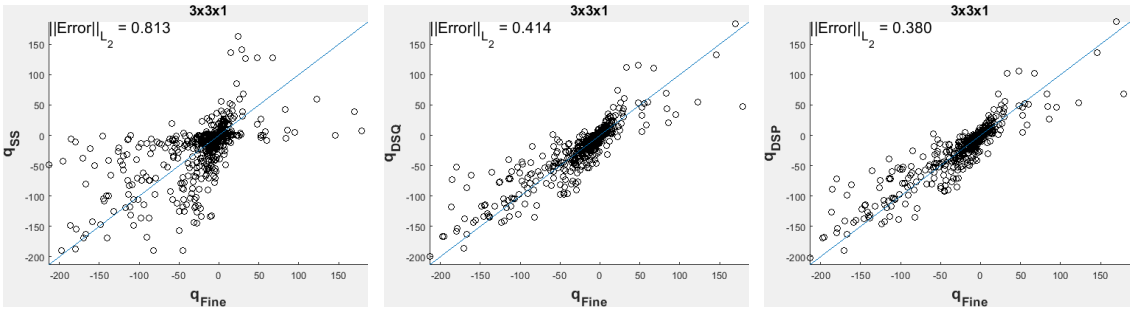

(a) Steady state **(b) DSQ** **(c) DSP**

Figure 4.24: Face flux comparisons at the end of simulation for SPE10 layer 68 two phase flow

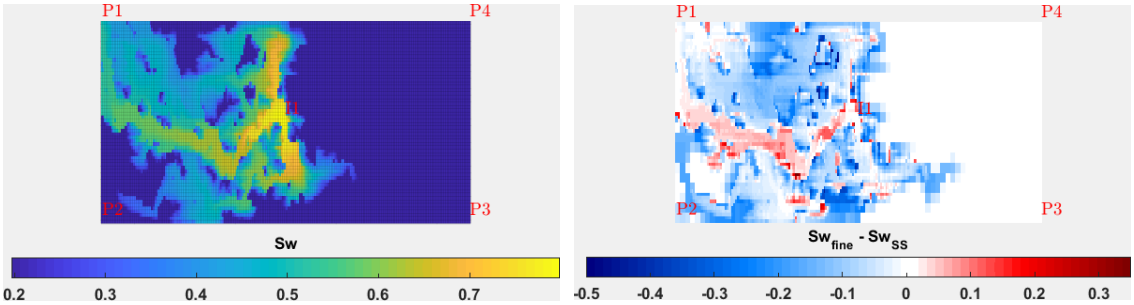

(a) Fine scale Sw **(b) Sw error - SS**

(c) Sw error - DSQ **(d) Sw error - DSP**

Figure 4.25: SPE10 layer 68 two phase flow water saturation error maps at the end of simulation

4.5.3 2D SPE10 Localization Tests

The localization tests performed in the PSS upscaling chapter are repeated here with the DS upscaling methods considering the same test case model – SPE10 layer 55. Figure 4.26 and Figure 4.27 represent the face flux comparisons for the steady state simulation using extended local, adaptive local-global, DSQ and DSP upscaling methods. Notice the error (Eq.(3.15)) for DS methods increased considerably compared to the PSS cases (Figure 3.17, Figure 3.18). This PSS threshold criteria for such a large coarsening ratio (10×10) can be very aggressive resulting in far few cells reaching PSS in a coarse block. The threshold criteria for DS methods is based on Eq.(4.17) which picks up only the well-connected sub volume to a face. For instance, see the example chosen from the current case (Figure 4.28) where the PSS threshold picks up only high permeability channel connected to the face. The downstream coarse cell has two high permeability zones separated by a low permeability baffle. The DS methods replace the barrier on the whole with a high transmissibility on either side of the downstream coarse block. The adaptive local-global method in this case would pick up the flow through the baffle using a global flow field whereas the DS methods pick up only one sub volume connected to the face. So, the DS methods effectively reduce the overall connectivity compared to an extended local or a local-global approach. A purely local method does not capture the flow tortuosity beyond the coarse blocks when coarsening to such a large factor especially in a channelized environment. However, the results indicate the DS methods have relatively less error compared to the extended local method.

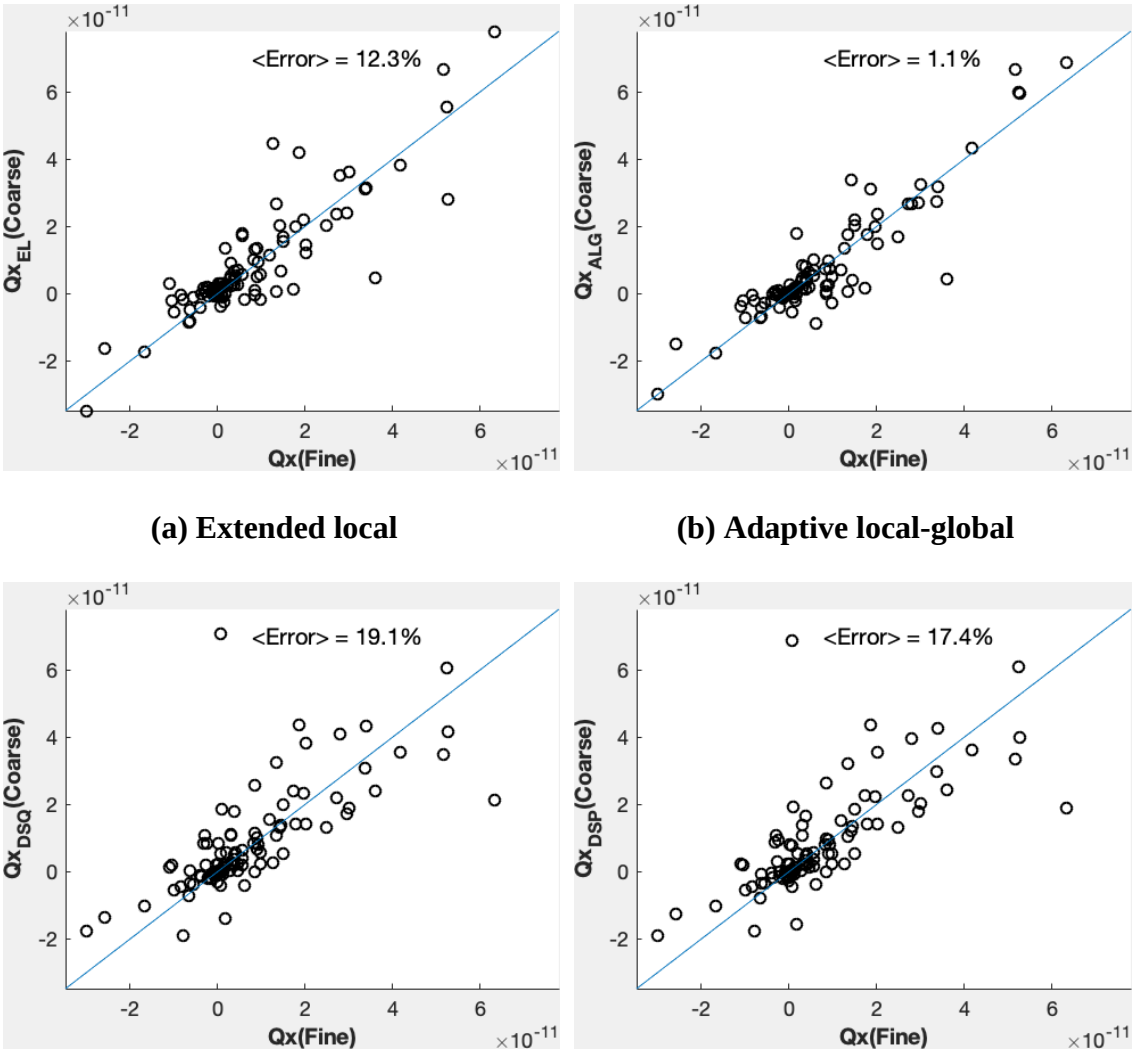

(a) Extended local **(b) Adaptive local-global**

(c) DSQ **(d) DSP**

Figure 4.26: SPE10 layer 55 X direction face fluxes with original DS cutoff

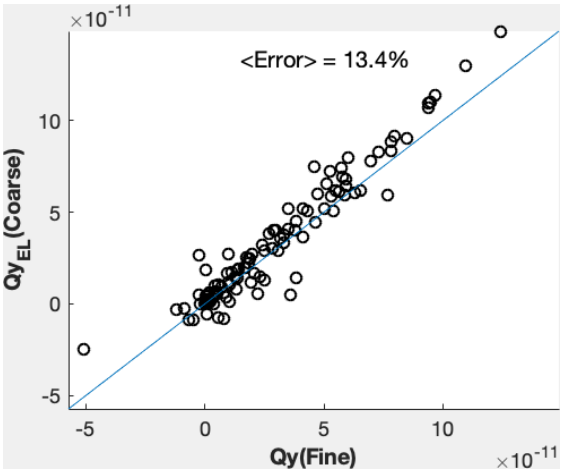

(a) Extended local

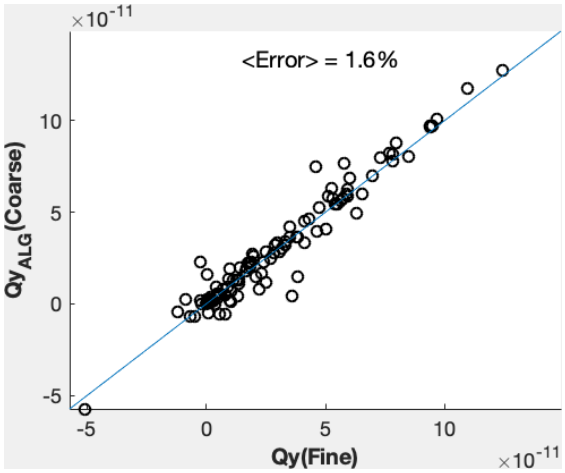

(b) Adaptive local-global

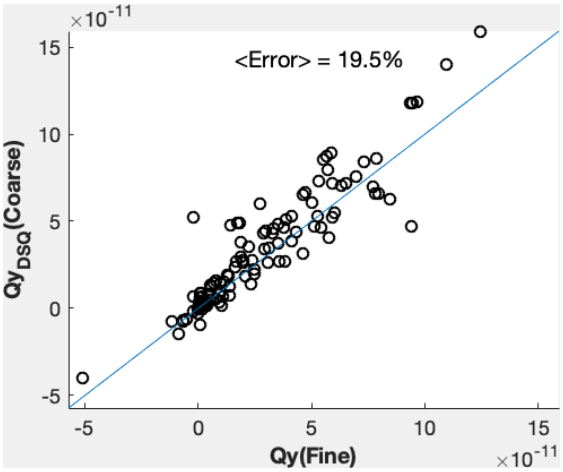

(c) DSQ

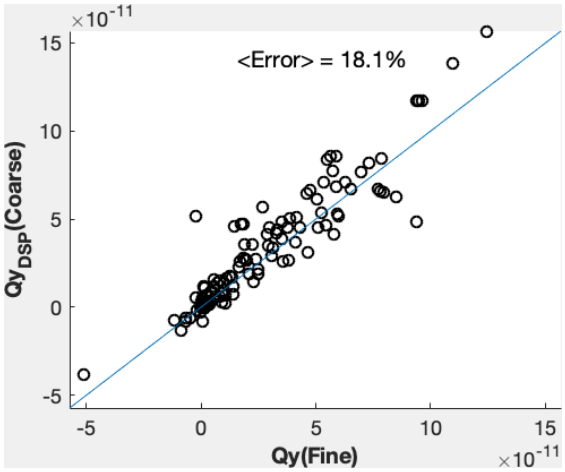

(d) DSP

Figure 4.27: SPE10 layer 55 Y direction face fluxes with original DS cutoff

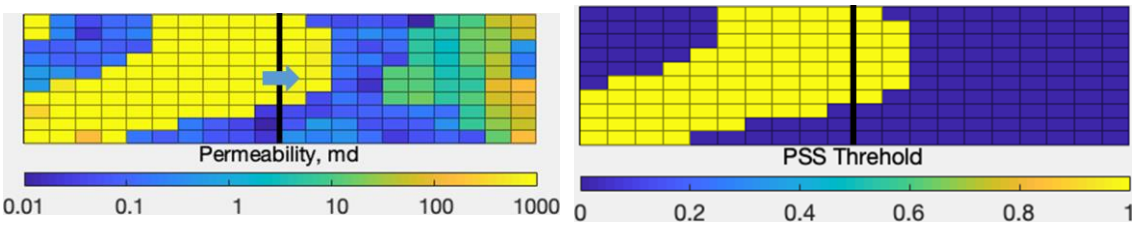

(a) Permeability **(b) Source/sink cells after cutoff**

Figure 4.28: SPE10 layer 55 10x10 coarsening example showing the impact of PSS threshold

Until now, the DS results were based on a time selection procedure described in section 4.3.1 which worked well for relatively small coarsening factors. However, the above results indicate the shortcoming of the time selection procedure in the presence of multiple sub volumes inside a coarse block. To investigate the same, a sensitivity study is performed based on different choices of thresholding. The thresholding procedure is still based on the concept of limit of detectability (LOD) at the outer boundary. However, the definition of outer boundary varies for each approach based on a reference diffusive time of flight τ_{ref}. The thresholding procedure based on τ_{ref} is given in Eq.(4.22) based on LOD.

$$e^{-\tau_i^2/4t_{LOD}} = \begin{cases} 1 & if\ e^{-\tau_i^2/\tau_{ref}^2} > 0.018 \\ 0 & otherwise \end{cases} \tag{4.22}$$

Three cases were considered as follows:

- Case 1: Based on PSS limit where $\tau_{ref} = 10\bar{\tau}$ with $\bar{\tau}$ defined using Eq.(4.14)

- Case 2: Based on LOD at the outer boundary defined by the minimum diffusive time of flight at the outer boundary cells $\left(\tau_{\min}^{b}\right)$. Here, $4t = 4t_{LOD} = \left(\tau_{\min}^{b}\right)^{2} / 4$. Therefore, $\tau_{ref} = \tau_{\min}^{b} / 2$.
- Case 3: Based on LOD at the outer boundary defined by $2\tau_{median}$. Here, τ_{median} refers to the median of the diffusive time of flights for the coarse block evaluated from the shared face.

For the sensitivity study, only the DSQ upscaling is considered. Figure 4.29 and Figure 4.30 represent the face flux comparisons after revising the thresholding criteria as per Eq.(4.22) and considering the above three approaches. Case 2 shows improved performance over case 1 but the DS method using case 3 shows relatively better performance on par with ALG upscaling. To explain this further, several local examples are considered by comparing the transmisisbilities obtained by each of the above 3 approaches.

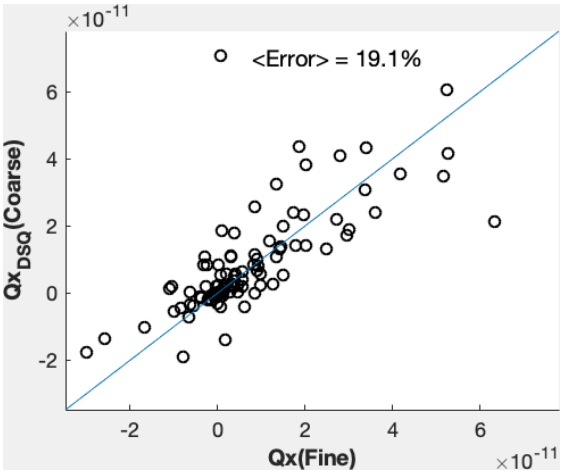

(a) Case 1

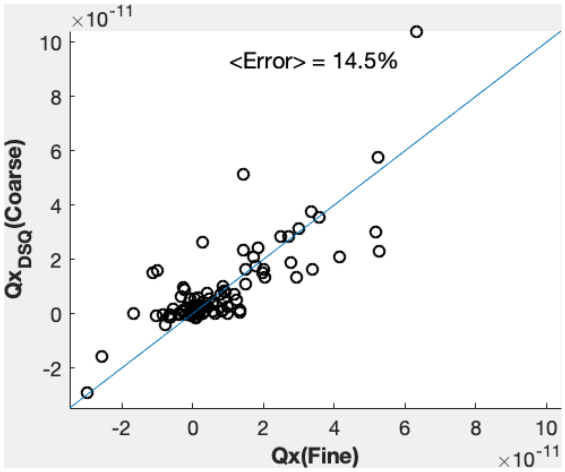

(b) Case 2

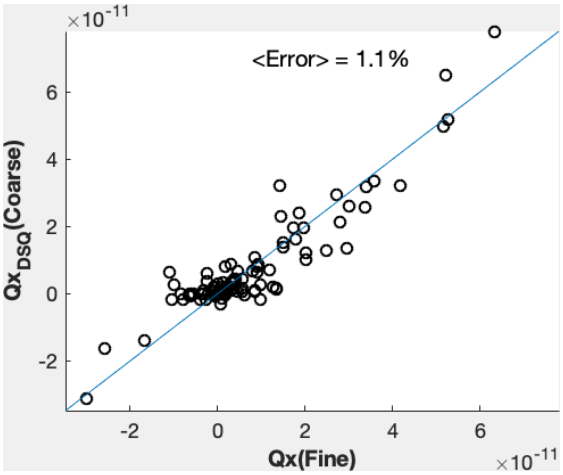

(c) Case 3

Figure 4.29: SPE10 layer 55 X direction face flux comparisons for the three cases considered in the threshold sensitivity study

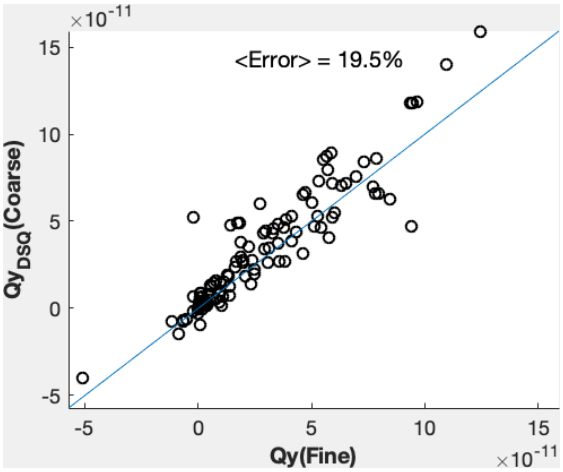

(a) Case 1

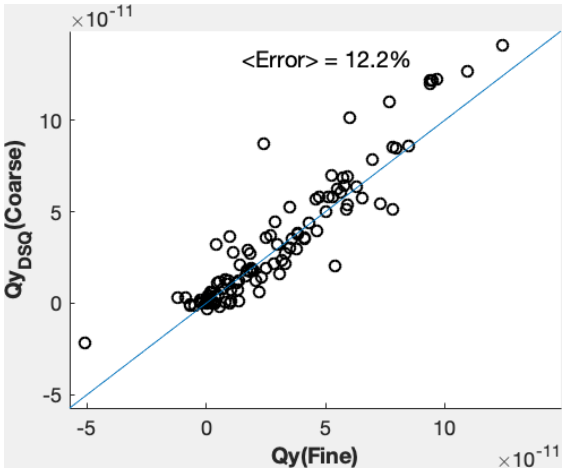

(b) Case 2

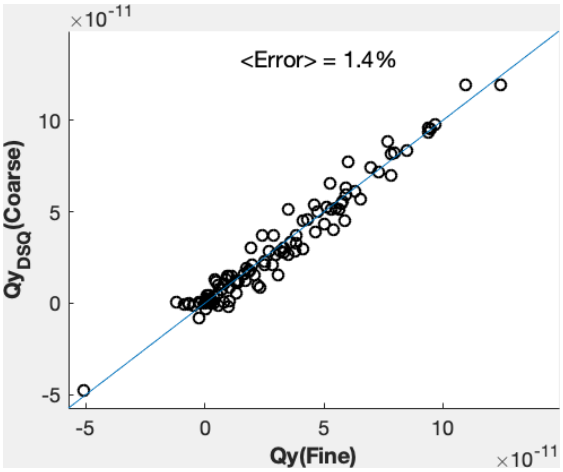

(c) Case 3

Figure 4.30: SPE10 layer 55 Y direction face flux comparisons for the three cases considered in the threshold sensitivity study

The first example is the same case considered in Figure 4.28. Figure 4.31 and Table 4.4 describe the impact of threshold for the three DS cases. Notice in Table 4.4, the largest error in face flux is shown for DSQ-1 which effectively short circuits the right coarse block giving a very high transmissibility. However, both cases 2 and 3 give comparable

transmissibilities and face flux errors. In fact case 3 and PSSQ are equivalent for this example as shown in Figure 4.31d where all the cells are tagged to PSS locally.

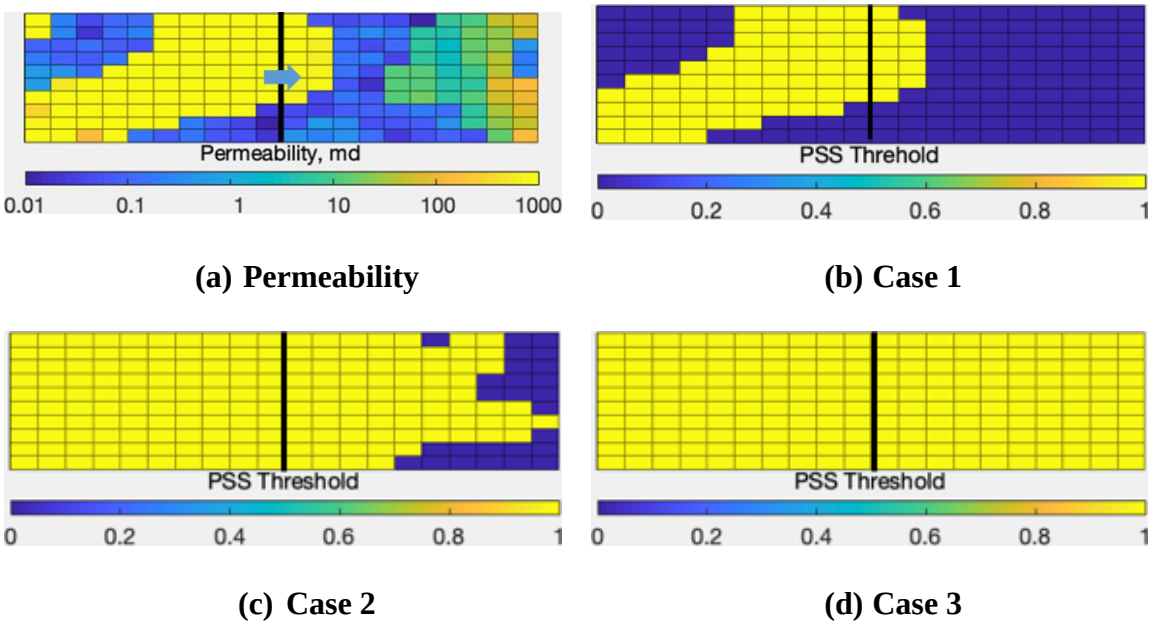

(a) Permeability **(b) Case 1**

(c) Case 2 **(d) Case 3**

Figure 4.31: Example 1 threshold sensitivity showing the source cells for each case after thresholding

Method	**T_{eff}**	**q_{face} Error (%)**
ALG	0.17	77
PSSQ	0.13	148
DSQ-1	1173	8715
DSQ-2	0.15	110
DSQ-3	0.13	148

Table 4.4: Summary of transmissibility and face flux errors for each upscaling method considered in Example 1

Figure 4.32 and Table 4.5 show the results for example 2 with permeability distribution shown in Figure 4.32a. Notice case 3 source distributions are able to reach the coarse cell boundaries but still have a sensitivity towards the low permeability volumes inside the coarse blocks which makes it different from PSS method. Case 2 just picks the minimum diffusive time of flight cell at the boundaries which gives rise to high transmissibility. In terms of the face flux errors in Table 4.5, case 3 shows the minimum error of all the DS cases.

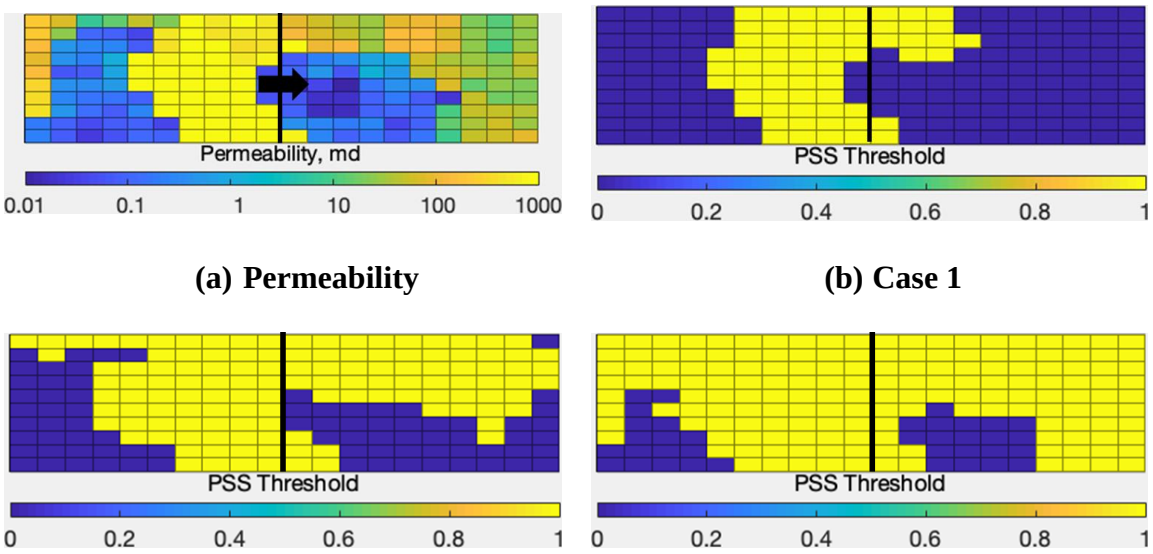

(a) Permeability **(b) Case 1**

(c) Case 2 **(d) Case 3**

Figure 4.32: Example 2 threshold sensitivity showing the source cells for each case after thresholding

Method	T_{eff}	q_{face} Error (%)
ALG	71.20	8
PSSQ	4.14	28
DSQ-1	59.50	67
DSQ-2	9.27	65
DSQ-3	5.03	23

Table 4.5: Summary of transmissibility and face flux errors for each upscaling method considered in Example 2

In example 3, the upstream coarse block has a low permeability volume towards the left (Figure 4.33a) and both case 1 and case 2 capture similar sub volumes to each PSS while case 2 tries to put sources even in the far left low permeability volume owing to the way it is defined based on the boundary τ. The face flux errors in Table 4.6 show the least error again for case 3. Even though the transmissibilities for the adaptive local global and case 1 are similar, the face flux errors are different because they are impacted by the global trend where the transmissibilities differ in other regions leading different face fluxes.

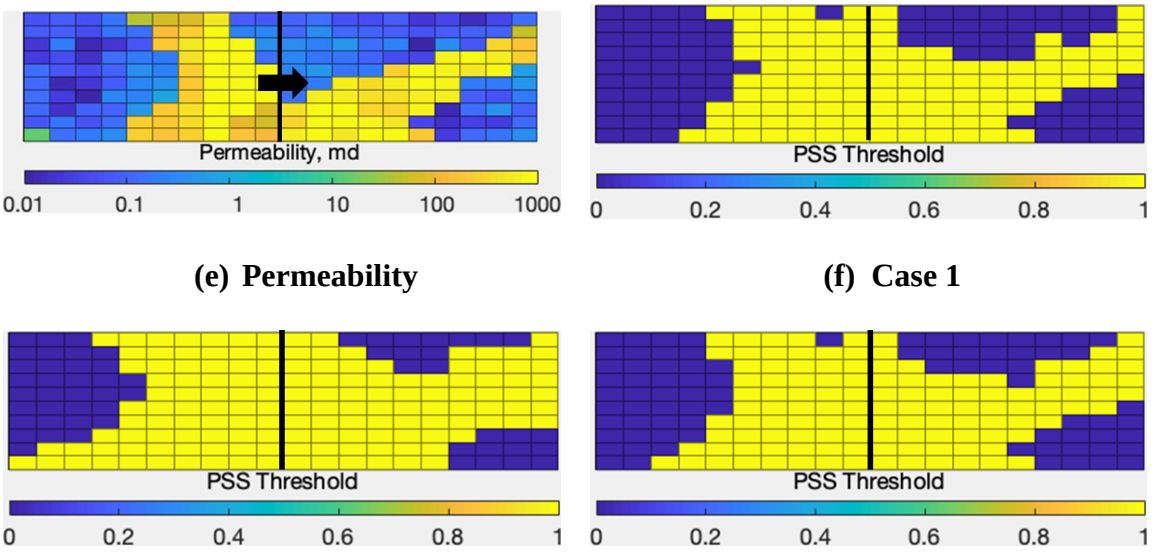

(e) Permeability **(f) Case 1**

(g) Case 2 **(h) Case 3**

Figure 4.33: Example 3 threshold sensitivity showing the source cells for each case after thresholding

Method	**T_{eff}**	**q_{face} Error (%)**
ALG	42.33	13
PSSQ	0.68	88
DSQ-1	41.20	21
DSQ-2	2.28	56
DSQ-3	24.46	2

Table 4.6: Summary of transmissibility and face flux errors for each upscaling method considered in Example 3

On the whole case 3 gives consistently better source distributions and face flux profiles. Hence, this will be the proposed way to define the transient source/sink terms for

the DS approach. In summary, the time for DS upscaling is selected based on LOD at the outer boundary defined by $2\tau_{median}$ giving Eq.(4.23).

$$\left(2\tau_{median}\right)^2 / 4t_{LOD} = 4 \tag{4.23}$$

Then, the PSS sub volume is identified based on Eq.(4.24). The thresholding procedure is summarized in Figure 4.34.

$$e^{-\tau_i^2/4_{LOD}} \Rightarrow \begin{cases} 1 & if \;\; \tau_i^2 / 4t_{LOD} < 4 \\ 0 & otherwise \end{cases} \tag{4.24}$$

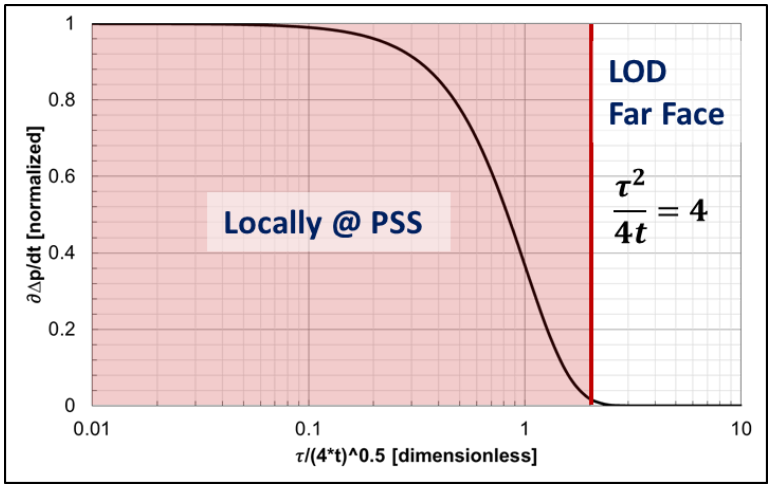

Figure 4.34: PSS threshold based LOD at far face

Figure 4.35 and Figure 4.36 show the face flux comparisons with revised DS cutoff. Clearly, the results have improved from previous case.

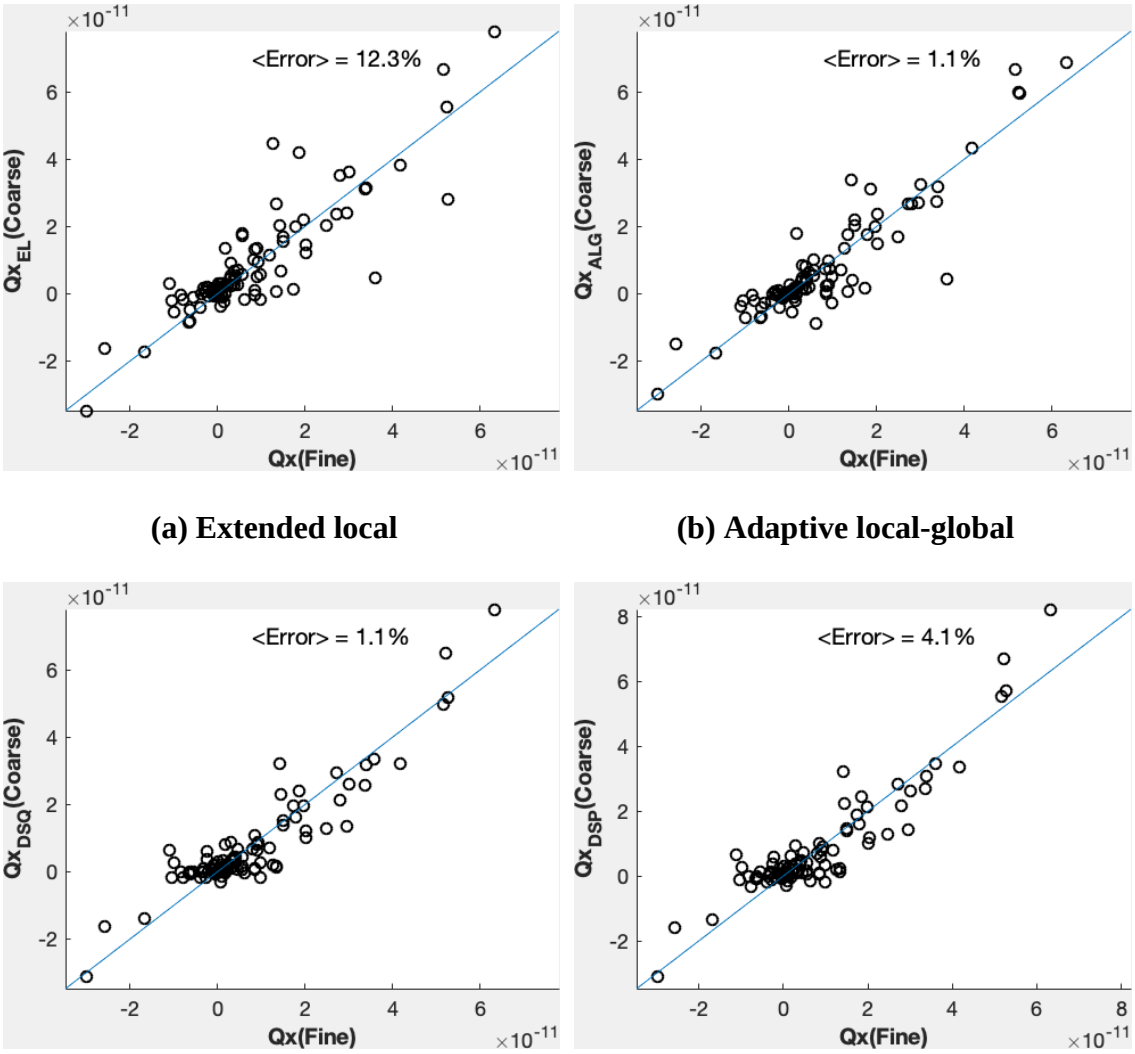

(a) Extended local **(b) Adaptive local-global**

(c) DSQ **(d) DSP**

Figure 4.35: SPE10 layer 55 X direction face fluxes with revised DS cutoff

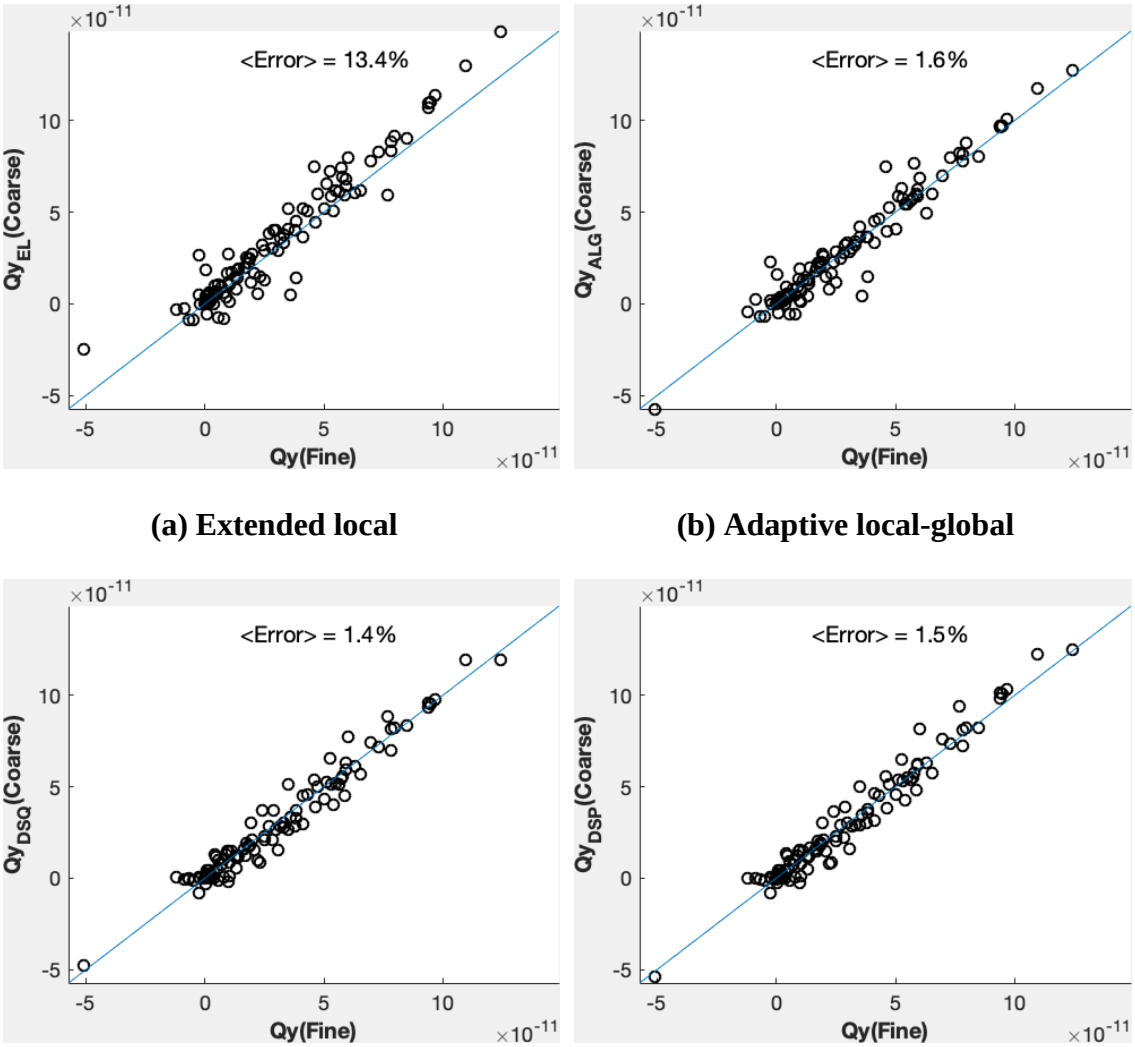

(a) Extended local **(b) Adaptive local-global**

(c) DSQ **(d) DSP**

Figure 4.36: SPE10 layer 55 Y direction face fluxes with revised DS cutoff

To test the impact of localization further, the same test case (layer 55) is now converted into a single phase oil primary depletion with 4 producers as shown in Figure 4.37. The producers are placed at $(5,5)$, $(5,175)$, $(55,215)$ and $(55,5)$ .The well bottomhole pressures were maintained at 5800 psia and the initial reservoir pressure at

6000 psia. The fluid (oil) and rock data is retained the same as the original SPE10 dataset. Simulation time is set to 5 months. For the ALG upscaling, the coarse transmissibilities are retained from the previous steady state simulation and are not recomputed for the new well configuration. This is the done to test the impact of large scale boundary conditions on the performance of the upscaling algorithm.

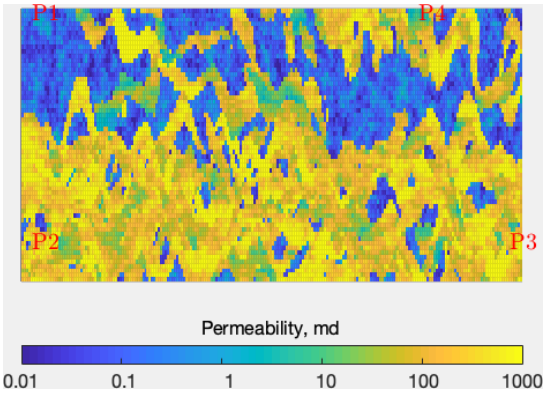

Figure 4.37: SPE10 layer 55 permeability with 4 producers

Figure 4.38 and Figure 4.39 represent the face flux comparisons (in both directions) at 1 and 5 months respectively. The errors increase with simulation time. Extended local upscaling exhibits the highest error while both the DS method perform reasonably well relative to the ALG and EL upscaling techniques. Notice, the error for ALG method is higher than both the DS methods since it is not optimized for the current well configuration. This highlights the dependence on the large scale boundary conditions for the ALG technique whereas DS upscaling does not refer to the global boundary

conditions and seems to give reasonable coarse scale descriptions as shown in the steady state and primary depletion simulation cases.

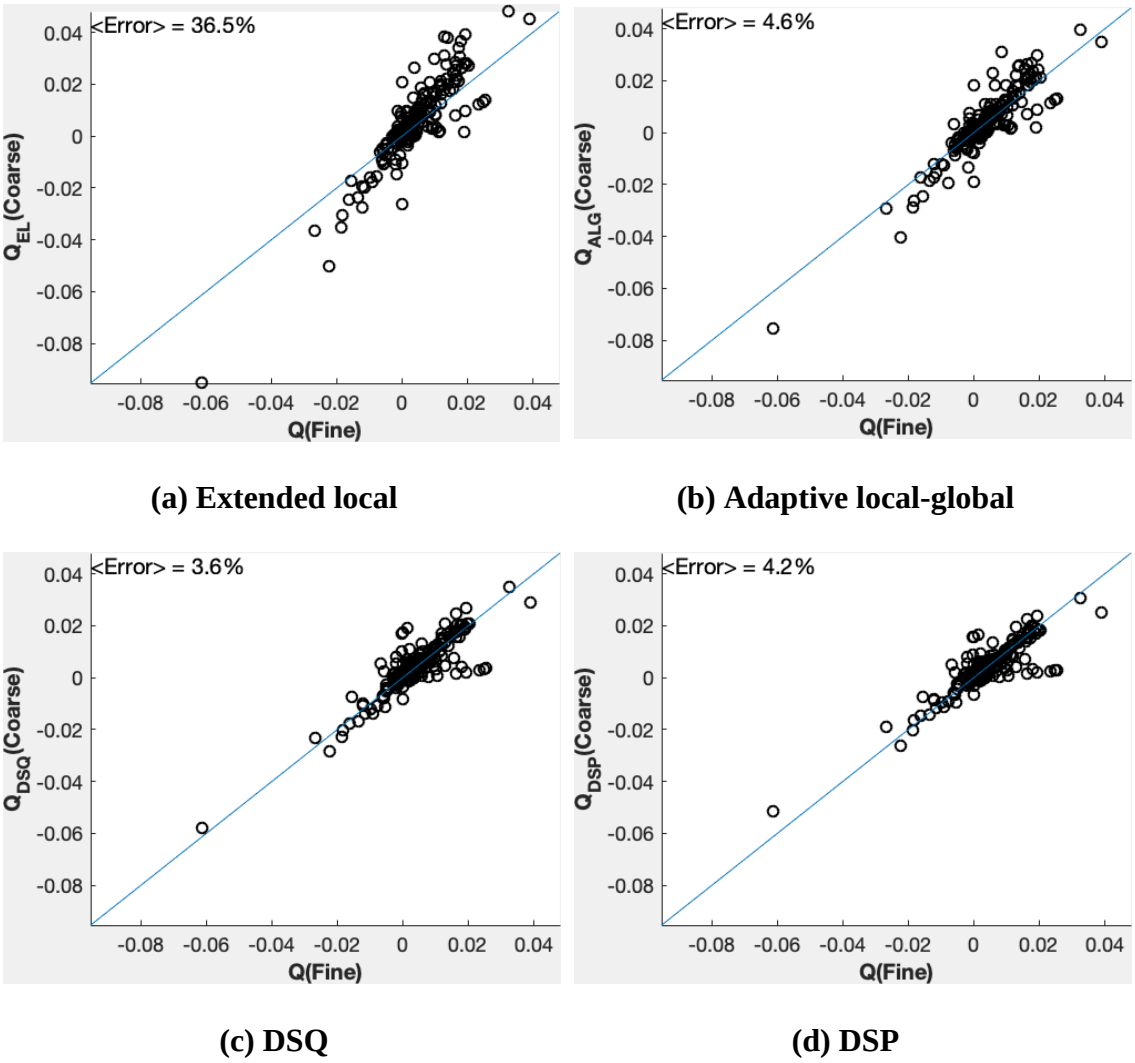

(a) Extended local **(b) Adaptive local-global**

(c) DSQ **(d) DSP**

Figure 4.38: SPE10 layer 55 primary depletion face flux comparisons at 1 month

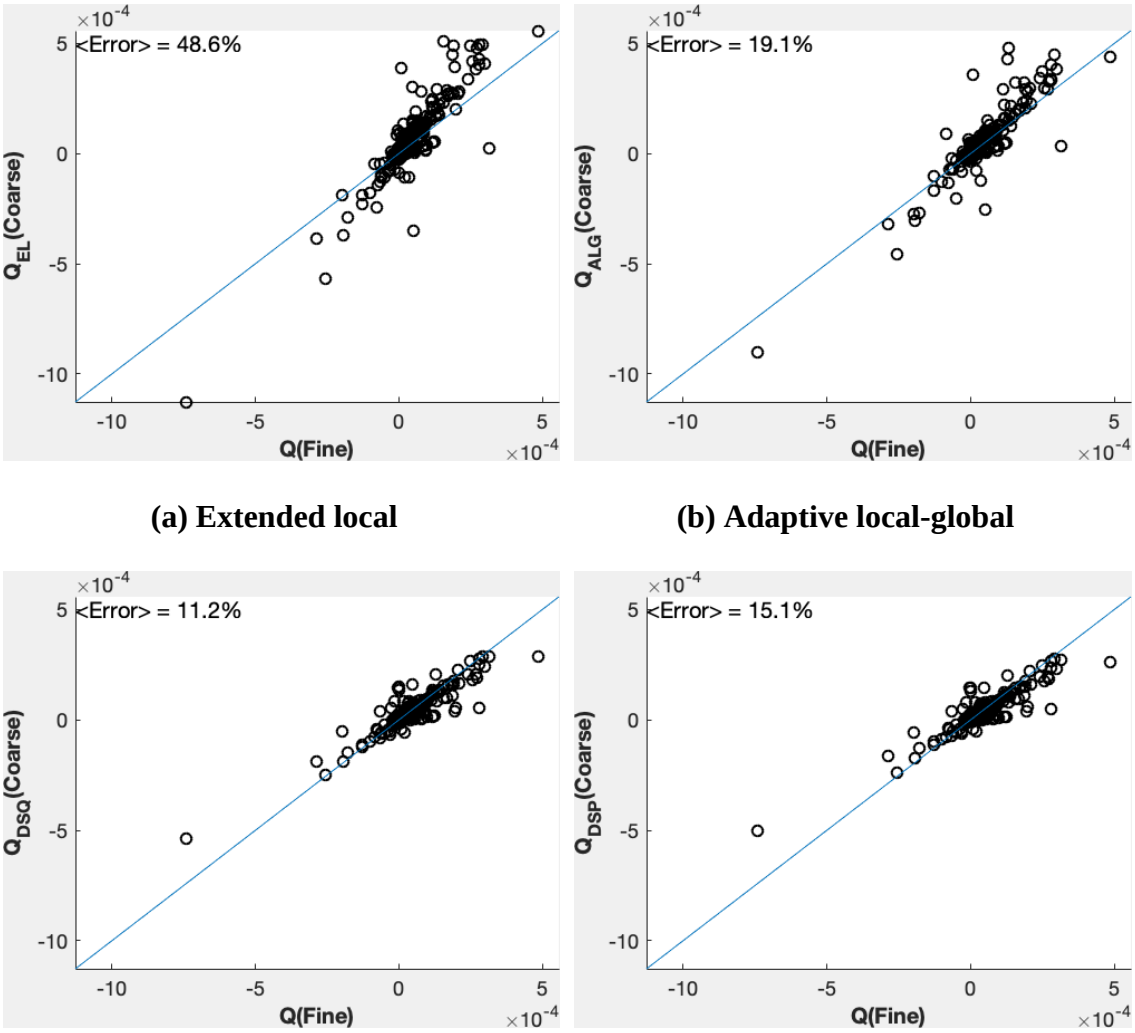

(a) Extended local **(b) Adaptive local-global**

(c) DSQ **(d) DSP**

Figure 4.39: SPE10 layer 55 primary depletion face flux comparisons at 5 months

4.5.4 3D Full Field Tight Gas Single Phase Flow

In this section, the DS upscaling techniques are applied to the tight gas simulation considered in the previous chapter (Figure 3.15). Figure 4.40 shows the cumulative gas recoveries for the 3 coarsening ratios. The DS results overlaps the PSS methods and all

the PSS, DS methods show accurate coarse well rates compared to steady state upscaling for $2\times2\times N$ and $3\times3\times N$.

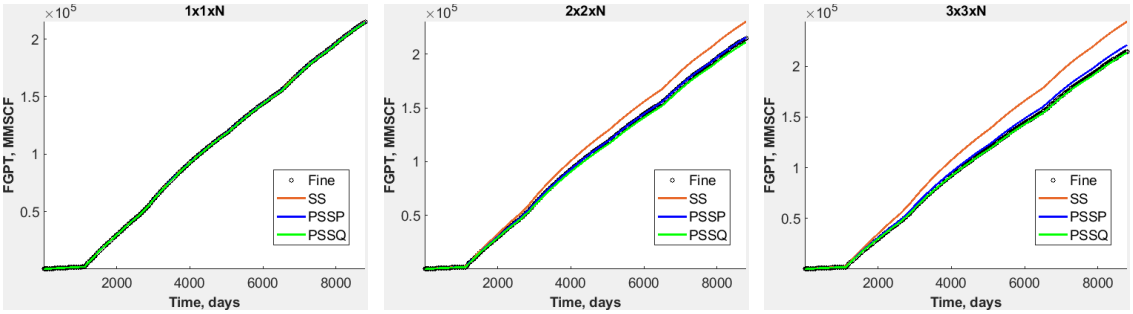

Figure 4.40: Tight gas full field recoveries

4.6 Extension to Faulted Grids

Since the PSS/DS upscaling technique is formulated by working backward from the flowing face, extension to faulted grids is natural by construction (Figure 4.41). A sector of Amellago carbonate outcrop model (Shekhar et al. 2014) is selected as a test case.

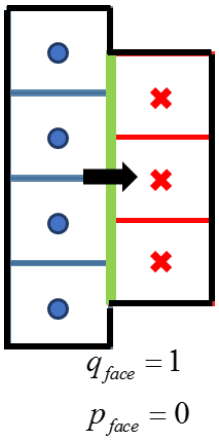

Figure 4.41: Faulted grid DSQ upscaling

There is around 9 orders of variance in permeability magnitude for the sector model and an inverted five spot well pattern is considered for steady state simulation (Figure 4.42). The model size is $42\times45\times45$ and has one fault running across the center as shown in Figure 4.42. The producers are maintained at a bottomhole pressure of 300 bars and the injector rate constraint is 2000 m^3/day . The initial reservoir pressure is set to 350 bars.

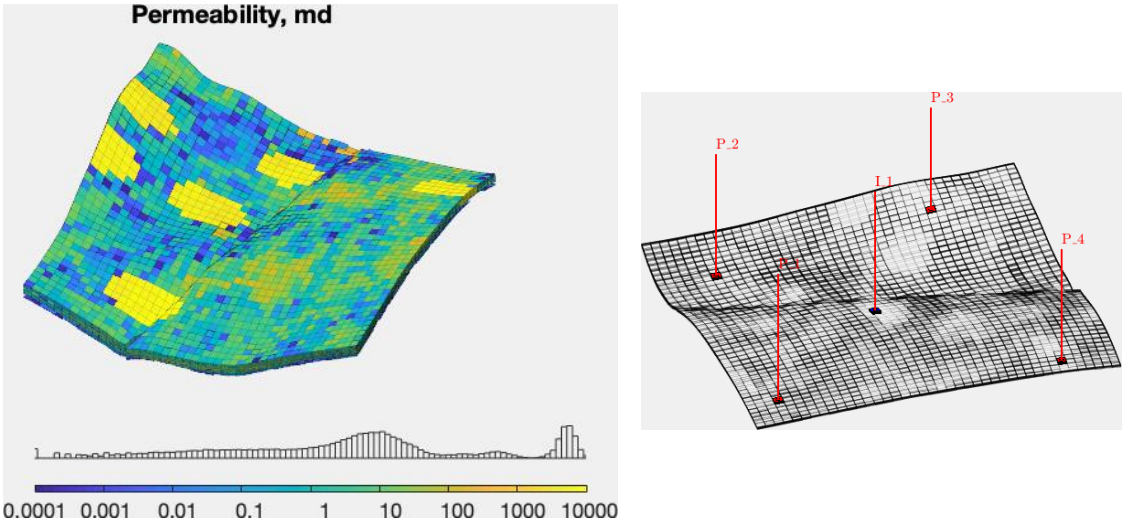

(a) Permeability **(b) Well locations**

Figure 4.42: Sector of Amellago carbonate outcrop model

For the purpose of benchmarking, cell permeability upscaling is considered as a reference. The coarsening factor is $2\times2\times3$. Figure 4.43 represents the face flux comparisons for the upscaling methods and the error is based on Eq.(3.16). Both DSQ and DSP perform well compared to SS upscaling method. Figure 4.44 shows the pressure maps

at the end of simulation which again show accurate pressure footprint for DSQ, DSP and steady state upscaling is the least accurate.

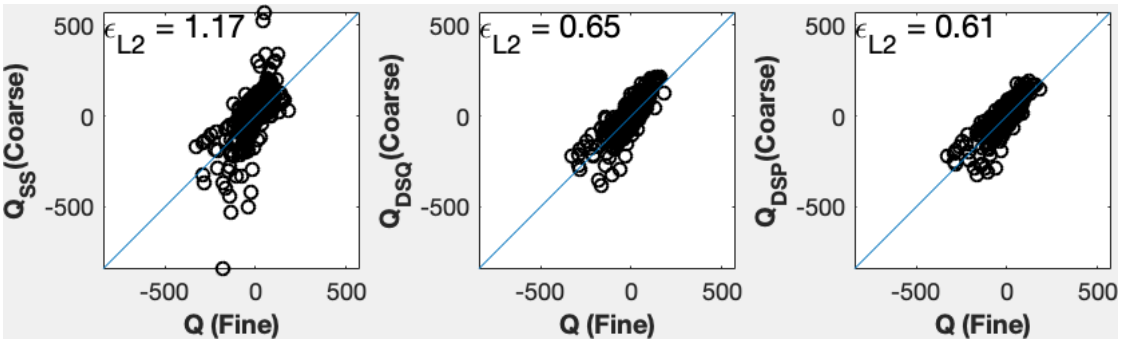

Figure 4.43: Amellago simulation steady state simulation face flux comparison

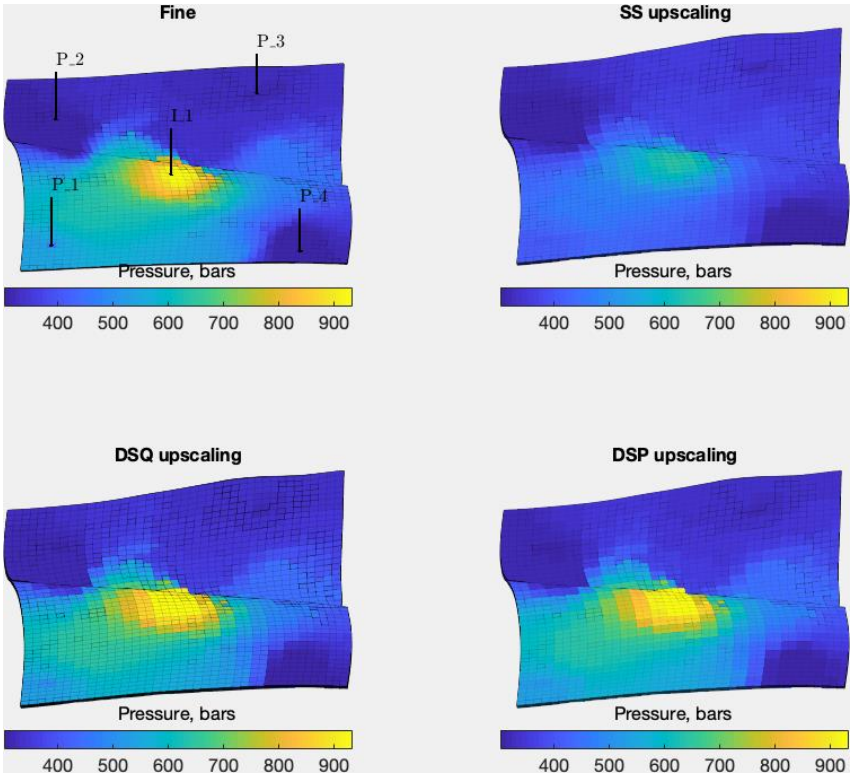

Figure 4.44: Amellago steady state simulation pressure profile

4.7 Discussion

A novel upscaling methodology was presented using pressure transient concepts which allows to distinguish between well-connected and weakly connected pay in a local upscaling calculation. The development of the method has relied upon the concepts of diffusive time of flight, drainage volume, and the approximate solution to the diffusivity equation. In contrast to the incompressible steady state algorithms, the diffuse source upscaling formulation is based upon a solution to the diffusivity equation and exposes more of the transient flow physics. It was shown that in a high contrast system, it is not necessary for the entire coarse volume to reach PSS. The DS formulation can identify the sub volume that can be sufficiently close to PSS giving results that are sensitive to local connectivity. However, if the volume is relatively homogeneous (well connected), the difference between PSS and transient solutions is negligible as seen in the time sensitivity examples.

The upscaling formulation is tested on high contrast 3D SPE10 model with single phase flow, 2D SPE10 model with two phase flow where both DSQ and DSP showed superior performance compared to steady state and PSS upscaling methods. The application of DS formulation to 2D localization tests showed that in the presence of multiple sub volumes, the original PSS threshold may not capture the fine scale flow behavior accurately. A new source/sink cutoff procedure was proposed to account for multiple sub volumes inside a coarse block. The new procedure showed improved local connectivity by still having a sensitivity towards low permeability stranded volumes. Revising the threshold showed significant improvement where the DS methods have

consistently shown reduced biases compared to those introduced by steady state incompressible upscaling boundary conditions (extended local and adaptive local-global) especially when the global boundary conditions are changed. The new thresholding procedure may be further investigated and tested on previously run 3D SPE10 cases. It seems there is a sweet spot in terms of defining the local source/sink terms that accurately capture the fine scale behavior. Therefore, the thresholding procedure needs further investigation especially for large coarsening factors.

The DS formulation is also extended to faulted systems and application of the same to a high contrast carbonate model highlighted the relative accuracy of the DS methods compared to steady state upscaling. Overall, DSQ upscaling method seems to be performing consistently well in all the cases tested in this work.

CHAPTER V

SUMMARY AND CONCLUSIONS: UPSCALING

5.1 Summary and Conclusions

A new construction of 1D transmissibility using PSS concepts was presented using the derived relation between pore volume average SS pressure drop and PSS pressure drop. Extension of 1D transmissibility construction to 3D was presented using a novel pressure averaging technique motivated by the flux continuity condition. Two different PSS averaging techniques are presented – PSSP and PSSQ. While PSSQ is a completely localized upscaling calculation, PSSP is weakly coupled to the upstream and downstream faces through non-zero local but zero total flux.

PSS methods by construction have less biases compared to incompressible steady state upscaling algorithms which are explicitly coupled to the large scale boundary conditions. This is explored by benchmarking PSS upscaling with extended local and adaptive local global upscaling methods and the results demonstrated the advantage of using PSS concepts for upscaling which does not couple to the global boundary conditions. Application to full field tight gas reservoir also showed better coarse scale descriptions compared to steady state upscaling. However, application of PSS upscaling to high contrast SPE10 model showed lower performance predictions relative to fine scale due to the assumption of pressure equilibrium inside a coarse block which is violated in the presence of weakly connected or disconnected pay.

A pressure transient diffuse source upscaling methodology based on diffusive time of flight and asymptotic pressure approximation was presented which exposes the transient physics. The formulation was shown to identify the sub volume that may reach PSS in the presence of high contrast relaxing the assumption of pressure equilibrium in a coarse volume. Application of the DS formulation to high contrast SPE10 single phase and two phase flow showed superior performance compared to steady state upscaling methods. Extension of the same formulation to faulted grids was also presented using a high contrast carbonate sector model example.

5.2 Future Research

All of the applications shown in the current work are based on two point flux approximations. However, PSS upscaling is not restricted to two point formulation. A full permeability/transmissibility tensor may be derived using PSS concepts on multi point discretization stencils which may be further explored.

A simple two-point upscaling diagnostics was presented in this work to highlight the advantage of using PSS concepts for upscaling over SS. These diagnostics may be further explored to give insight into when a two-point upscaling calculation may be inaccurate.

The choice of PSS threshold may be further investigated especially for large areal coarsening ratios when there are multiple sub volumes inside a coarse block. This is where the DS construction may be further improved by the use of adaptive gridding. For instance, if the difference between PSS and DS transmissibility is too high, it may be a favorable

place to perform adaptive coarsening or even the apriori diffusive time of flight information may be utilized to decide upon the adaptivity. Also, the face pressure constraint used to remove the local material balance errors is also another candidate where adaptive grid design will be applicable. The diffusive time of flight and drainage volume concepts may also be utilized to design adaptive layering schemes for geologic models based on apriori calculations.

It may be worthwhile to retain the areal resolution in the well blocks to the original fine scale resolution so that there is no impact of off centered wells while upscaling the well indices. Most of the cases considered in the current work have non-centered wells in the coarse blocks. Well index makes a significant impact on the performance of the upscaled models and removing the ambiguity regarding upscaling well connections may go a long way in improving the proposed upscaling algorithms in the current work.

CHAPTER VI

INTRODUCTION: MULTISCALE SIMULATION

Multiscale methods have recently garnered much attention as a robust alternative to upscaling and fine scale simulation. As discussed in Chapter 1, to make reservoir simulation practically feasible, it is customary to use some kind of upscaling procedure. Unfortunately, there is a tradeoff between loss of information and model accuracy while using these upscaling methods especially in the presence of high contrast and non-stationary correlation structures. The model error may be significant with a high level of coarsening especially when considering multiphase flow. The purpose of multiscale reservoir simulation methods is not only to capture the large scale behavior as with upscaling but to solve the problem at original fine scale resolution and keep the computational cost comparable to any upscaling procedure. This is made possible by the construction of multiscale basis functions that allow the solution to be mapped back and forth between the fine and coarse grids. The mapping is not restricted to two scales of projection (fine and coarse), the basis functions allow the solution to be projected to any number of scales (fine scale resolutions). However, the current work is restricted the two scale projection multiscale methods.

Multiscale methods involve solving pressure on the coarse computational grid and saturation changes on the original fine grid. To this end, the so called multiscale basis functions are constructed through the solutions of localized flow problems just like the case of flow based upscaling. Instead of constructing the effective transmissibilities /

permeabilities, the basis functions act as coarse properties and also enable retaining the fine scale information inside them. As is the case with flow based upscaling, the choice of boundary conditions employed to localized the flow problems and build the basis functions can have a significant impact on the accuracy of the solution. The pressure equation known hereby as the flow equation is elliptic/parabolic in nature and the saturation equation known as the transport equation is hyperbolic in nature. Both equations in their general formulation are highly nonlinear and tightly coupled. However, the pressure equation becomes elliptic and linear for incompressible flow. The motivation for solving the saturation on the finer scale is due to its highly nonlinear behavior and strong dependence on the local heterogeneity. Following Table 1.1, when there is significant velocity variance in a coarse block, a single value of averaged saturation will not be able to capture the frontal movement. Instead the changes in pressure are relatively large scale which may be resolved on a coarser mesh. This coarse information may be downscaled to the fine grid using basis functions and the downscaled information is used to solve the saturation changes.

Every multiscale method has two major steps: construction of multiscale basis functions and assembling the global system of equations. Multiscale methods separate themselves on the basis of how these basis functions are constructed. The basis functions are designed to capture the multiscale features of the solution. Multiscale methods are broadly divided into multiscale finite element and finite volume methods. A broad literature review of these methods is presented below. For a comprehensive overview of the multiscale methods, please review Efendiev and Hou 2009.

6.1 Multiscale Finite Element Method (MsFEM)

Multiscale finite element method (MsFEM) was first formulated by Hou and Wu 1997 for incompressible flow. A brief overview is given below.

Let the fine grid domain Ω be partitioned into T^h finite elements known as the coarse grid. Consider the elliptic pressure equation in domain Ω belonging to real numbers of dimension d ($\mathbb{R}^d$).

$$\nabla \cdot \left(\vec{k} \cdot \nabla p \right) = f \ in \ \Omega \in \mathbb{R}^d \tag{6.1}$$

Let x_i be the interior nodes of the mesh T^h and ϕ_i^0 be the nodal basis of the standard finite element space. The basis function ϕ_i for a coarse grid element *K* is obtained by solving the local flow problem given by

$$\nabla \cdot \left(\vec{k} \cdot \nabla \phi_i \right) = 0 \ in \ K, \phi_i = \phi_i^0 \ on \ \partial K, \forall K \in T^h \tag{6.2}$$

The multiscale basis function obtained this way coincide with the finite element basis functions on the boundary of the coarse grid block *K* and are oscillatory in the interior domain depending on the local heterogeneity. The representation of the fine scale solution via basis functions allows reducing the dimension of computation. Once the basis functions are computed for each coarse grid node, the next step is to assemble the coarse system of equations. Let p_h be the approximate solution given by Eq.(6.3) where p_i represent the approximate value of the solution at the coarse grid nodes (unknown).

$$p_h = \sum_i p_i \phi_i(x) \tag{6.3}$$

Eq.(6.3) is substituted in the original fine scale equation Eq.(6.1) and multiplied with coarse scale test functions resulting in a complete coarse dimensional system of equations. Two choices of coarse test functions exist in the literature namely Galerkin finite element and Petrov-Galerkin (Hou et al. 2004). The resulting coarse solution may be projected back on to the fine scale using Eq. (6.3) and this fine scale information may now be used to solve multiphase saturation on the original fine grid.

The choice of boundary conditions for the basis function play an important role in capturing the underlying heterogeneity. The boundary condition for the multiscale basis function should reflect the oscillation of the solution across the coarse grid boundary (Efendiev and Hou 2009). If not, there can be significant errors resulting from the resonance between the coarse grid size and the characteristic length scale of the problem. As per Hou et al. 1999, the resonance error becomes large when the two scales are close. These resonance errors may be reduced by solving one dimensional reduced problems across the boundaries like the multi scale finite volume methods which will be discussed in the next section (Jenny et al. 2003) or oversampling methods (Hou and Wu 1997; Efendiev et al. 2000). Oversampling methods tend to reduce the impact of the boundary conditions by extending the computational domain beyond the coarse grid where the problem is solved. One issue with the MsFEM is that the reconstructed fine scale solution is not conservative due to pressure basis. Chen and Hou 2003 clearly indicate that a conservative fine scale velocity is necessary for accurate modeling of multiphase flow

(transport equation). Therefore, they proposed a conservative mixed finite-element method which will be discussed now.

6.2 Multiscale Mixed Finite Element Method (MsMFEM)

In standard mixed finite element methods, one seeks an approximate solution of the pressure equation (Eq.(6.4)) written here for incompressible flow where q is the external source and λ_{rt} is the total relative fluid mobility.

$$\nabla \cdot \vec{u} = q,\ \vec{u} = -\lambda_{rt}\left(\vec{\vec{k}} \cdot \nabla p\right) in\, \Omega \tag{6.4}$$

The mixed formulation reads: find the velocity and pressure $(u, p) \in H_0^{div}(\Omega) \times L^2(\Omega)$ such that

$$\begin{aligned} &\left(\left(\lambda_{rt}\vec{\vec{k}}\right)^{-1}\vec{u}, \vec{v}\right) - \left(p, \nabla \cdot \vec{v}\right) = 0 \quad \forall v \in H_0^{div}(\Omega) \\ &\left(\nabla \cdot \vec{u}, l\right) = \left(q, l\right) \quad \forall l \in L^2(\Omega) \end{aligned} \tag{6.5}$$

Here, $H_0^{div}(\Omega) = \left\{v \in L^2(\Omega)^n : \nabla \cdot \vec{v} \in L^2(\Omega), \vec{v} \cdot \vec{n} = 0 \ on \partial\Omega\right\}$ and $L^2(\Omega)$ is the square integrable function space over Ω. Notice the permeability tensor is written in the inverse form together with the fluid mobility in Eq.(6.5). In mixed finite element methods, the solution space is restricted to subspaces $V \subset H_0^{div}(\Omega)$ *and* $W \subset L^2(\Omega)$ which follows:

$$\begin{aligned} &\left(\left(\lambda_{rt}\vec{\vec{k}}\right)^{-1}\vec{u}_h, \vec{v}_h\right) - \left(p_h, \nabla \cdot \vec{v}_h\right) = 0 \quad \forall v_h \in V \\ &\left(\nabla \cdot \vec{u}_h, l_h\right) = \left(q, l_h\right) \quad \forall l_h \in W \end{aligned} \tag{6.6}$$

The subspaces may be defined using the lowest order RT0 (Raviart and Thomas 1977) or BDM1 (Brezzi et al. 1985). While the normal component of velocity for RT0 space is constant, it is allowed to be linear for BDM1. Both have the same piecewise uniform subspace for pressure. The velocity subspace or the basis function for velocity is usually constructed per a cell interface. For RT0, one basis function per interface is required. However, for BDM1, there is one additional set of "divergence-free" basis. A brief summary of these basis is explained in Arbogast 2000.

The multiscale mixed finite element method discussed here was first formulated by Chen and Hou 2003 to account for mass conservation issues generated on the coarse mesh by the original mixed finite element method (Hou and Wu 1997). Arbogast 2002 and Arbogast and Bryant 2002 presented another version of mixed multiscale finite element approach where localization was achieved using special boundary conditions on the coarse block boundaries. The basis functions were incorporated into the coarse scale equation by means of numerical Greens functions.

The MsMFEM proposed by Chen and Hou 2003 produces mass conservative solutions on the coarse scale but not necessarily on the fine scale. This was modified by Aarnes 2004 and Aarnes et al. 2006 to generate conservative velocity field both on the coarse as well as the fine scale to simulate multiphase flow. This is done by introducing source functions to construct localized basis functions. On the coarse scale, the velocity is basis function is a generalization of the RT0 method and the pressure basis is piecewise uniform. Aarnes et al. 2008 extended the MsMFEM formulation to corner point grids and

Pal et al. 2015 validated the formulation by including the effects of compressibility, gravity and capillarity. A brief overview of the MsMFEM formulation is described below.

Consider two coarse elements E_i and E_j with $\Gamma_{ij} = \partial E_i \cap \partial E_j$ being the share interface between them. The multiscale basis associated with the interface Γ_{ij} is calculated by solving the following

$$\begin{aligned} &\vec{\psi}_{ij} = -\lambda_{rt}\vec{\vec{k}} \cdot \nabla p \\ &\nabla \cdot \vec{\psi}_{ij} = \begin{Bmatrix} w_i(x) \Big/ \int_{E_i} w_i(\xi)\, d\xi & \forall x \in E_i \\ -w_j(x) \Big/ \int_{E_j} w_j(\xi)\, d\xi & \forall x \in E_j \end{Bmatrix} \\ &\vec{\psi}_{ij} \cdot \vec{n} = 0, \quad on \;\; \partial\left(E_i \cup \Gamma_{ij} \cup E_j\right) \end{aligned} \tag{6.7}$$

Notice while solving the basis function for the interface, all other faces are maintained at no flow boundary conditions making the problem completely localized (Eq.(6.7)). The source term w_i was proposed to be equal to the trace of permeability tensor ($tr(\vec{\vec{k}})$) by Aarnes 2004. Krogstad et al. 2009 and Lie, K.-A. et al. 2012 utilized the source function scaled by local porosity to account for compressibility effects. Although MsMFEM has the advantage of working for complex unstructured geometries (Aarnes et al. 2008), inclusion of physics like compressibility, capillarity is difficult owing to the mixed form of pressure equation. For incompressible flow, fine scale pressure is irrelevant. Hence, a piecewise uniform basis would work. However, for non-elliptic parabolic form of pressure equation (for e.g.: compressible flow), the pressure information is also required on the fine scale. Although Lie, K.-A. et al. 2012 proposed basis functions for pressure, their validity is not tested on realistic models.

6.3 Multiscale Finite Volume Method (MsFVM)

The multi scale finite volume method was introduced by Jenny et al. 2003, Jenny et al. 2005 where the basis functions for pressure are constructed on a dual grid connected by the coarse cell centroids. The formulation by construction generates conservative coarse scale solutions by working from cell centers as basis nodes. The pressure is expressed as a linear combination of basis functions ϕ_i to incorporate subscale variations. The method has been tested on wide variety of problems like compressible flow (Lunati and Jenny 2006, Zhou and Tchelepi 2008 and Hajibeygi and Jenny 2009), density driven flow (Lunati and Jenny 2008, Künze and Lunati 2012), black oil flow (Lee et al. 2008), near well modeling (Wolfsteiner et al. 2006, Jenny and Lunati 2009) and fractured flow (Hajibeygi et al. 2011). To reduce the errors in the presence of strong heterogeneities, an iterative framework was proposed by Hajibeygi et al. 2008 and later extended by Hajibeygi and Jenny 2011 to include adaptivity in the computation of basis functions. The basic idea of the iterative framework is to systematically bring the fine scale residuals by means of locally computed correction functions for low frequency errors and a global smoother for high frequency errors. The MsFVM was also formulated in an algebraic manner by means of compact matrix operations using prolongation and restriction operators (Zhou and Tchelepi 2008, Lunati et al. 2011). This formulation was generalized and extended to stratigraphic grids by Møyner and Lie 2014a.

Although MsFVM ensures mass conservation on the coarse scale, the resulting fine scale solution is however not conservative. Therefore, a velocity reconstruction

procedure is performed before the fine scale velocities are passed on to a transport solver. The reconstruction procedure is done by solving the localized flow problems by using the non-conservative dual grid fluxes as boundary conditions. Kippe et al. 2008 utilized the nested gridding approach proposed by Gautier et al. 1999 to reconstruct the conservative fine scale velocities.

A brief overview of the original multiscale finite volume method is given below. As discussed above, the MsFVM works with two coarse grids: primal coarse grid and the dual grid as shown in Figure 6.1. The dual grid (A) marked by the dashed lines is encompassed by 4 primal coarse blocks. For each dual coarse grid block, a set of dual basis functions are constructed for each node in the dual grid (coarse cell centers). An elliptic problem of the form Eq.(6.8) is solved on the dual grid boundary with boundary pressure boundary conditions $p_i = \delta_{ik}\ (k = 1,4)$ just like a conventional flow based steady state upscaling method. The four solutions form the dual basis functions $\Phi^k\ (k = 1,4)$ and the pressure solution inside the dual grid is given by Eq.(6.9). This generates a multi-point stencil akin to the multi-point flux approximation (MPFA) scheme.

$$\nabla \cdot \left(\lambda_{rt} \vec{\vec{k}} \cdot \nabla p \right) = 0 \tag{6.8}$$

$$p = \sum_{k=1}^{4} p_k \Phi^k \tag{6.9}$$

Now, the flux q across the coarse blocks can be written as a linear combination (Eq.(6.10)) where q^k represent the flux contributions from corresponding dual basis functions.

$$q = \sum_{k=1}^{4} p_k q^k \tag{6.10}$$

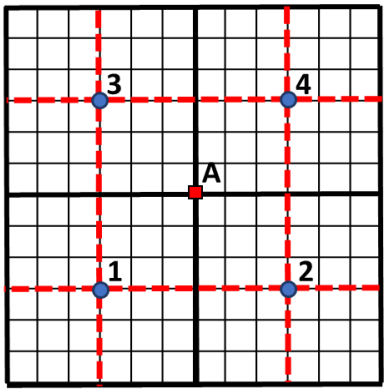

Figure 6.1: MsFVM primal (bold solid lines) and dual coarse grid (red dashed lines) on the underlying fine grid (solid lines)

The dual basis functions may be used to compute the effective transmissibilities based on the Eq.(6.10) which will be utilized in solving the coarse solution. Once the coarse solution is obtained, the fine scale solution is readily obtained using Eq.(6.9). Although the MsFVM generates conservative coarse scale velocity field, the fine scale velocities are discontinuous across the dual grid interfaces. Hence, a velocity reconstruction procedure is employed to generate a conservative fine scale velocity field. The velocities generated from dual basis may be equally distributed on the coarse grid boundary as done by the original paper by Jenny et al. 2003 or they may distributed based on intercell fine scale transmissibility as weights as done by Gautier et al. 1999. These fluxes serve as boundary conditions to solve localized flow problems that yield the required mass conservation on the fine scale.

The multiscale basis functions are usually calculated only once at the beginning. However, this may not be sufficient to reduce the fine scale residual especially in areas where the total mobility change is high. Thus, Jenny et al. 2005 introduced an adaptive criterion to re-compute basis functions only in the areas where the total mobility exceeds a particular threshold. One of the challenges for the MsFVM is the accuracy and robustness in the presence of high contrast and high anisotropy. Møyner and Lie 2014a showed that the method is not robust enough in the presence of high contrast features in a way that even the iterative schemes do not work. This may be partly due to the boundary conditions employed to localize the flow problem in the dual basis function calculations.

6.4 Multiscale Restricted Smooth Basis Method (MsRSB)

The multiscale restricted smooth basis method is considered to be the one of the most robust and accurate multiscale method based on application results to wide variety of test cases (Møyner and Lie 2016b, Møyner and Lie 2016a and Lie et al. 2017). The MsRSB method was formulated in the multiscale finite volume framework to resolve the complex challenge of unstructured grids and high contrast reservoir properties using an iterative framework. The method itself was originally inspired the multi scale two point flux approximation (MsTPFA) method formulated by Møyner and Lie 2014b. MsRSB was tested on black oil models in Møyner and Lie 2016a and a realistic reservoir simulator environment in Lie et al. 2017. It was also extended to fracture simulation in Shah et al. 2016. A brief overview of the method is presented below using incompressible flow example.

The multiscale formulation starts with the prolongation operator for pressure which maps the coarse pressure on to the fine grid (Eq.(6.11)). The prolongation operator is nothing but a matrix of basis functions obtained by solving localized flow problems as is the case with every multiscale method.

$$p_f = P p_c \tag{6.11}$$

The original fine scale system is of the form

$$A p_f = q \tag{6.12}$$

Substituting Eq. (6.11) in Eq.(6.12) and multiplying by the restriction operator (R) gives the coarse system of equations.

$$R\left(A\left(P p_c\right)\right) = \left(RAP\right) p_c = A_c p_c = Rq = q_c \tag{6.13}$$

Two choices exist for the restriction operator, the control volume restriction operator and the Galerkin operator. The Galerkin operator is just a transpose of the prolongation operator and is generally used in the multi scale finite element methods. However, since the focus of MsRSB is not on iterative performance, the control volume restriction operator is used here which is a matrix of the ones if the fine scale block belongs to a particular coarse block and zero elsewise. This corresponds to setting the coarse flux between two blocks as the summation of fluxes induced by the prolongation operator. While the MsFVM works with a dual grid to construct the prolongation operator (basis functions), MsRSB works with only with the primal coarse grid which is partitioned on the original fine grid.

The procedure for calculating the prolongation operator for MsRSB method differs from other multiscale methods in the sense that it is an iterative process which does not the solve the localized flow problems. In fact the approach used for MsRSB prolongation operator construction is more akin to the multigrid methods which employ a single step smoother to reduce local error i.e., Jacobi interpolation (Vanek et al. 1994). The initial value of the prolongation operator in the iterative process is chosen as the transpose of the restriction operator i.e., an injection matrix of ones and zeros. A local smoothing iteration is defined given by Eq.(6.14) where D is the diagonal matrix of the fine scale stiffness matrix (A) and ω is a relaxation factor set to 2/3. The iterative process ensures that the prolongation operator is algebraically smooth. The support of the basis functions increases with each itearation. To avoid this, support regions are predefined for each coarse block and the updates during the iterations are restricted within the support regions. The support regions are defined by local triangulation of the block centroids and face centroids of the coarse faces that are shared by the corresponding block. In 2D, the support region for a coarse block extends to a maximum of 9 coarse block neighbors.

$$P_j^{n+1} = P_j^n - \omega D^{-1} A P_j^n \tag{6.14}$$

After computing the prolongation operator, an iterative smoothing step may be performed on Eq.(6.13) to take care of the localized low frequency errors. As is the case with MsFVM, MsRSB method also requires flux reconstruction to generate mass conservative fine scale velocity fields. The flux reconstruction is performed by re-

computing the fine scale solution using flux boundary conditions over the coarse block edges obtained from the multiscale pressure solution.

6.5 Research Objectives: Multiscale Simulation

The motive of the current work is to extend the PSS/DS upscaling formulation developed in the previous chapters to multiscale framework. Since the PSS/DS upscaling formulation is based on flux boundary condition, the formulation closely aligns with the MsMFEM.

The multiscale work in this dissertation is divided into two sub topics dealing with incompressible and compressible flow. For the incompressible flow formulation, two different work flows are presented: Upscaling-downscaling workflow and the multiscale mixed finite element workflow. In the upscaling-downscaling workflow, the coarse problem is solved using the effective transmissibilities obtained from the pressure averaging procedure formulated in the upscaling section and the multiscale workflow is the same as the MsMFEM but the proposed method differs in the calculation of basis functions. For the compressible flow, only the upscaling-downscaling workflow is tested and the complete multiscale formulation for compressible flow is motivated for future research. The proposed multiscale method is tested on 2D and 3D cases of SPE10 synthetic reservoir model and benchmarked against the MsMFEM proposed by Aarnes 2004 for incompressible flow.

CHAPTER VII

MULTISCALE DIFFUSE SOURCE METHOD

7.1 Multiscale Diffuse Source (MsDS) Method – Incompressible Flow

In this section, the multiscale diffuse source method is presented for two phase (oil, water) incompressible flow in the absence of gravity and capillarity. The governing equations are formulated in terms of total velocity ($\vec{u}$) for flow and fractional flow ($f_w = \lambda_w / \lambda_{rt}$) formulation for transport. The flow equation is written in terms of total relative mobility ($\lambda_{rt} = \lambda_o + \lambda_w = k_{ro}/\mu_o + k_{rw}/\mu_w$) and total velocity as shown below. Here, q is the total external source (well rates)

$$\vec{u} = -\lambda_{rt}\vec{\vec{k}} \cdot \nabla p, \quad \nabla \cdot \vec{u} = q \tag{7.1}$$

The transport equation is expressed in terms of water saturation (S_w).

$$\phi \frac{\partial S_w}{\partial t} + \nabla \cdot f_w \vec{u} = q_w \tag{7.2}$$

Notice for solving water saturation using Eq.(7.2), only the fine scale velocity is required. Hence, the pressure information is immaterial for incompressible transport in the absence of gravity and capillarity. The transport equation is solved on the fine scale using two-point upstream weighted mobility discretization (Brenier and Jaffre 1991) which guarantees monotonicity in saturation movement. The time dependence of the quantities may be handled using the well-known IMPES (Implicit pressure, explicit saturation) formulation or sequential implicit (Watts 1986, Tchelepi et al. 2007) schemes. The focus

of the multiscale work is however on the flow equation which will be discussed further. Two different workflows are proposed for solving Eq. (7.1) on the coarse grid and Eq. (7.2) on the original fine grid.

7.1.1 Upscaling-Downscaling Workflow

In the upscaling-downscaling workflow the flow problem is solved on the coarse grid using effective single phase transmissibilities obtained from the diffuse source upscaling method. The flow problem is of the form Eq.(7.3) where A_c contains the coarse transmissibility matrix and well source/sink matrix depending on the well boundary conditions. Flow from well to well cell is handled using the diffuse source-P upscaled well index described in the upscaling chapter 4.

$$A_c p_c = q_c \tag{7.3}$$

The single phase coarse transmissibilities are multiplied by total mobilities which are evaluated based on pore volume averaged coarse saturation and the single point upstream weighted pressure scheme. Once the coarse system of equations is solved using a two-point flux approximation (TPFA) scheme (Aziz and Settari 1979), the coarse fluxes are downscaled using the DSQ formulation. To achieve this, basis functions are constructed and stored while performing the upscaling calculation. The procedure for assembling the basis matrix is outlined below.

Let n_f, N_f be the number of active (each face has at least 2 neighbors) fine and coarse faces respectively. The flux basis matrix Ψ of size $n_f \times N_f$ is obtained by solving

the localized DS upscaling calculations as described in Figure 4.11. One slight difference for downscaling exercise here is that no additional face pressure constraint is imposed on the coarse face as is the case with Figure 4.11. With the face pressure as isobar, the coarse flux is continuous. However, the fine scale flux need not be continuous across the face. Therefore, instead of imposing an additional isobar constraint on the face pressure which also acts as a gauge condition, the pore volume averaged fine scale pressure equal to coarse cell pressure is used as the gauge condition. This removes the discontinuity in fine scale flux across the coarse face which results due to the constant pressure condition. While Aarnes 2004 utilized the trace of permeability tensor in the source/sink terms, the current formulation uses the source/sink terms proportional to $\phi\Theta\left(\tau_{LOD}(t)-\tau\right)$. Figure 7.1 describes the downscaling formulation for DSQ method as an example. Notice, the coarse face pressure is no longer an isobar.

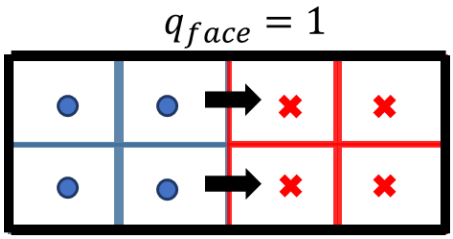

Figure 7.1: DSQ downscaling

Each column of Ψ represents a basis function solution for a particular coarse face. The solution is nothing but the local fine scale face fluxes stored in a column as per the global fine scale face numbers. It can be constructed while performing the upscaling

calculation. Once the basis matrix Ψ is assembled and the coarse solution is available from Eq.(7.3), the coarse face fluxes (q_c) are downscaled to fine scale fluxes (q_f) using superposition principle by multiplying the coarse fluxes with the basis matrix (Eq.(7.4)). The well fluxes are also downscaled using the same principle.

$$q_f = \Psi q_c \tag{7.4}$$

The downscaled flux field is fed into the transport solver (Eq.(7.2)) to solve for fine scale saturations. Since, the flow problem is incompressible, the basis functions calculated using DS formulation do not always guarantee mass conservation on the fine scale due to finite time transient cutoff in the source/sink terms (Figure 7.2). Mass conservation on the fine scale is a necessary requirement when solving for saturations which was clearly documented by Chen and Hou 2003. Therefore, the downscaling exercise is performed using PSS basis functions ($e^{-\tau^2/4t} = 1$) even though the transmissibilities are calculated using the transient PSS-DS upscaling method with thresholding based on Eq.(4.24). The superposition of PSS basis gives back the steady state profile on the fine scale as demonstrated earlier in the PSS upscaling chapter. In order to account for the steep pressure gradients in low permeability cells due to finite PSS source terms, an additional thresholding is proposed for downscaling the coarse flux. The thresholding is based on the average cell $\bar{\tau}^{cell}$ which is based on the arithmetic average of the directional cell diffusive time of flights as shown in Eq.(7.5). Once the $\bar{\tau}^{cell}$ is defined, a thresholding procedure is applied per a coarse cell using Eq.(4.14) and Eq.(4.17). Notice, there is no need to trace the τ from any seed point. Instead, the individual cell diffusive

time of flights are used in this thresholding procedure. Effectively, the relatively low permeability cells in a coarse block are forced to steady state using this procedure. This way, the advantage of using a transient formulation is still retained.

$$\bar{\tau}^{cell} = \frac{\tau_x^{cell} + \tau_y^{cell} + \tau_z^{cell}}{3} \tag{7.5}$$

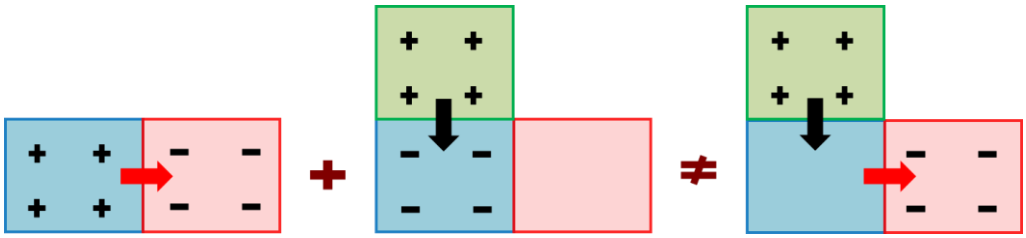

Figure 7.2: Mass conservation issue for incompressible DS downscaling

Two different choices for DS upscaling-downscaling are available – DSQ and DSP based on the work done in chapter 4. However, DSP method has the issue of flux continuity at all the coarse faces due to the leaky flux condition imposed at the upstream and downstream faces while solving the localized flow problems. This may require special treatment i.e., the projecting the discontinuous velocity field on to a different velocity basis to obtain a continuous mass conservative velocity field on the fine scale. Therefore, only DSQ downscaling method is explored in the current work.

7.1.2 Multiscale Diffuse Source (MsDS) Workflow

In this section, the new multiscale formulation is presented using the multiscale mixed finite element method framework. The formulation is very much similar to the one

proposed by Aarnes 2004,Aarnes et al. 2006. Instead of TPFA discretization, mimetic finite difference method (Brezzi et al. 2005) is utilized making it generally applicable to complex grids (see Aarnes 2004) . The mimetic discretization of the mixed form of the diffusivity equation (Eq.(6.5)) in matrix form reads as Eq.(7.6) where q_f represents outward the fine scale face fluxes, B is the inverse of the half-cell transmissibility matrix obtained from mimetic discretization and C is the gradient operator which maps the properties from cell centers to cell faces (e.g.: pressure gradient).

$$\begin{bmatrix} B & C \\ C^T & 0 \end{bmatrix} \begin{bmatrix} q_f \\ -p \end{bmatrix} = \begin{bmatrix} 0 \\ q \end{bmatrix} \tag{7.6}$$

The multiscale formulation begins with the following approximations for fine scale flux and pressure.

$$q_f = \Psi q_c + \tilde{q}, \quad p = \Phi p_c + \tilde{p} \tag{7.7}$$

Here, q_f, q_c, p, p_c represent the fine and coarse face fluxes, fine and coarse cell pressures respectively. $\tilde{q}, \tilde{p}$ are the fine scale residuals leftover after the multiscale approximations. Φ is the pressure basis matrix which for incompressible flow is replaced with simple prolongation operator I that maps a uniform coarse pressure into each fine cell that represent the coarse block. The size of I is number of fine cells by number of coarse cells ($n_c \times N_c$). The flux basis matrix Ψ is obtained using the same procedure mentioned in the upscaling-downscaling section and Figure 7.3 summarizes the same calculation.

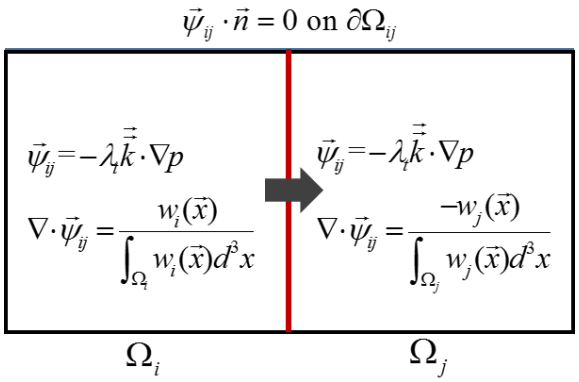

Figure 7.3: Calculation of flux basis for MsMFEM/MsDS method

Substituting Eq.(7.7) in Eq. (7.6) and neglecting the flux residual $\tilde{q}$ gives rise to Eq.(7.8).

$$\begin{bmatrix} B\Psi & CI \\ C^T\Psi & 0 \end{bmatrix} \begin{bmatrix} q_c \\ -p_c \end{bmatrix} = \begin{bmatrix} C\tilde{p} \\ q \end{bmatrix} \tag{7.8}$$

Now, to restrict the solution to the coarse space, Galerkin restriction operator ($R = diag\left(\Psi^T, I^T\right)$) is multiplied to the above equation and the pressure residual is set to zero by utilizing the gauge condition as pore volume averaged coarse pressure set to zero. The final coarse system of equations reads:

$$\begin{bmatrix} \Psi^T B\Psi & I^T CI \\ I^T C^T \Psi & 0 \end{bmatrix} \begin{bmatrix} q_c \\ -p_c \end{bmatrix} = \begin{bmatrix} 0 \\ I^T q \end{bmatrix} \tag{7.9}$$

Once the coarse solution is obtained, the fine scale solution may be reconstructed using Eq. (7.7). For the current study, the basis functions are evaluated only once initially. However, an adaptive criterion (Jenny et al. 2005) may be employed to re-compute basis functions in the regions where mobility changes are appreciable. Again for incompressible

flow, the reconstruction is performed using PSS basis function instead of DS basis to honor the divergence free velocity field in the absence of external source/sinks.

7.1.3 Numerical Experiments

The multiscale workflows described above are tested on SPE10 synthetic reservoir model. The proposed methods are benchmarked against the MsMFEM proposed by Aarnes 2004, Aarnes et al. 2006. All of the multiscale work proposed here is non iterative. Therefore, the multiscale solutions are only an approximation to the fine scale flow field and there is will still be a finite residual leftover. In order to account for this leftover residuals, an iterative procedure may be employed as proposed by Lunati et al. 2011, Lie, K.-A. et al. 2012 so that the multiscale solutions converge exactly to the fine scale solution.

2D SPE10 Two Phase Flow

The multiscale methods proposed above were first tested on SPE10 top layer which has fairly continuous permeability distribution and the cross plot of permeability and porosity also show a clear linear trend on semi log scale (Figure 7.4). An injector-producer pair is placed at the corners as shown in Figure 7.4a. The coarsening ratio is 5×10 and the simulation time is 1 year. The producer is maintained at a constant bottomhole pressure of 100 bars and the injector is set to a rate constraint of 0.0027 pore volume injected (PVI) per day which results in a voidage replacement ratio of 1. The fluid viscosities for both oil and water are set to 1 cp and the Corey relative permeability exponent for oil and water is

2 (quadratic relative permeabilities). The fine scale simulation is performed using the usual two point discretization.

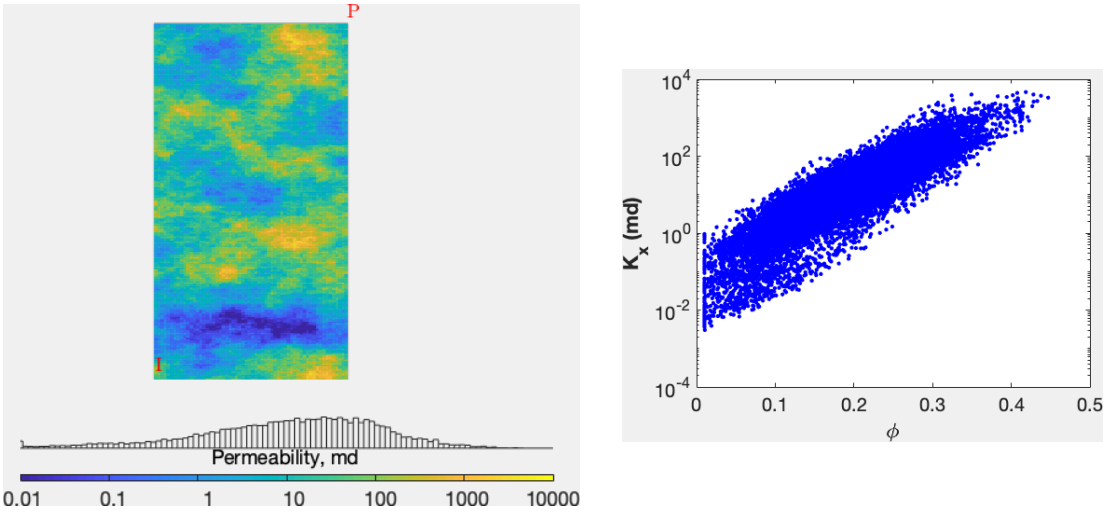

(a) Permeability **(b) Permeability vs porosity**

Figure 7.4: SPE10 layer 1 properties used for multiscale simulation

Figure 7.5a and Figure 7.6a represent the reconstructed velocity and water saturation profiles at the end of simulation and the corresponding errors relative to the fine scale simulation respectively. The velocity visualized here is the total cell velocity plotted using $\log_{10}|v|$ to highlight the variability. The velocity and water saturation errors are also plotted as a function of time step in Figure 7.5b and Figure 7.6b respectively. The velocity error $(e(v))$ and the saturation errors $(e(S))$ are calculated based on the L^2 norm given by Eq.(7.10).

$$e(v) = \frac{\left\| v_{ref} - v \right\|_{L^2}}{\left\| v_{ref} \right\|_{L^2}}, \quad e(S) = \frac{\left\| S_{ref} - S \right\|_{L^2}}{\left\| S_{ref} \right\|_{L^2}} \tag{7.10}$$

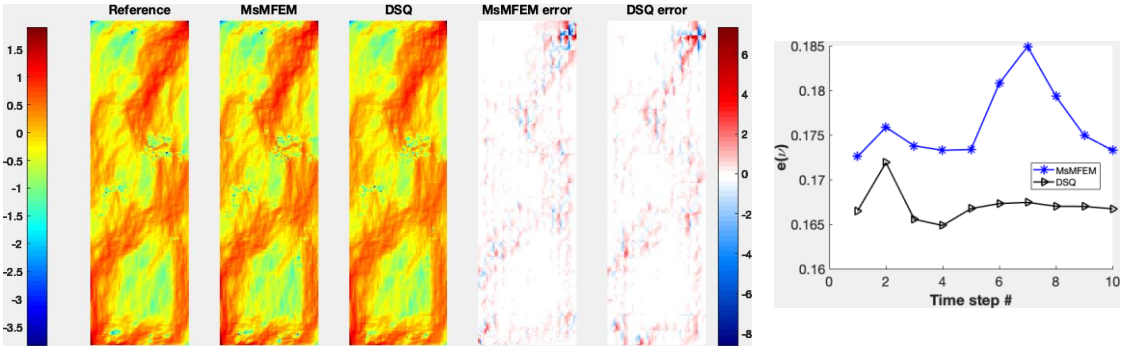

(a) Velocity profile **(b) Velocity error**

Figure 7.5: SPE10 layer 1 reconstructed fine scale velocity profiles at 1 PVI and the velocity error plot for MsMFEM and DSQ methods

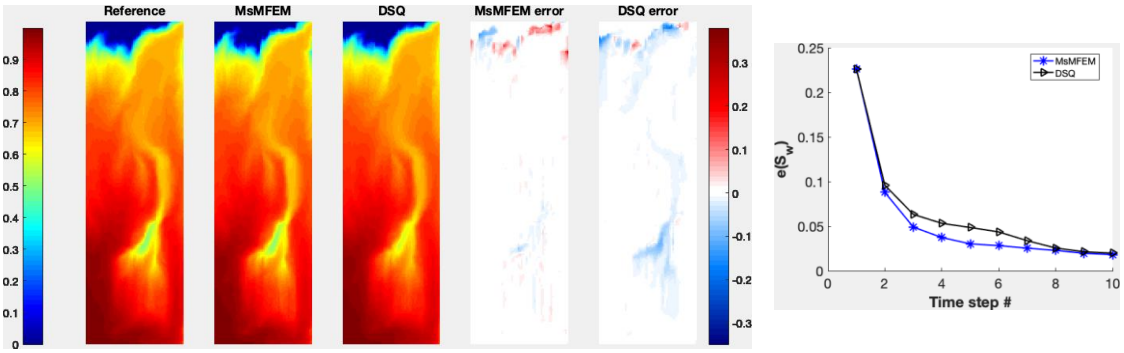

(a) Water saturation (Sw) profile **(b) Sw error**

Figure 7.6: SPE10 layer 1 water saturation profiles at 1 PVI and the Sw error plot for MsMFEM and DSQ methods

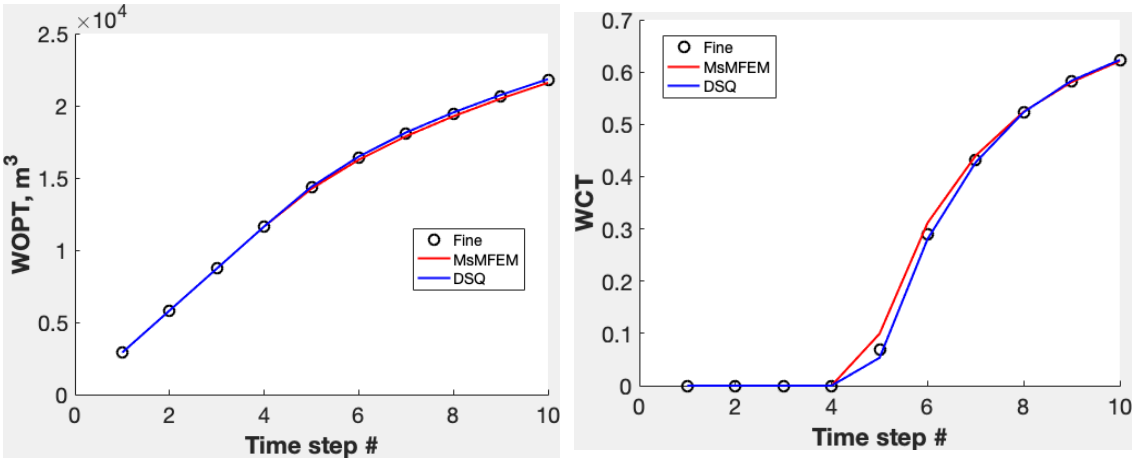

Figure 7.7: SPE10 layer 1 cumulative oil production and water cut for MsMFEM and DSQ methods

The cumulative oil production and producer water cut are similar for both the methods (Figure 7.7) with DSQ giving slightly accurate predictions. The overall results indicate that the DSQ upscaling-downscaling workflow gives slightly better velocity profiles but MsMFEM gives slightly better water saturation profile. However, the MsDS workflow seems to give slightly accurate velocity and water saturation profiles relative to MsMFEM which is evident in Figure 7.8 and Figure 7.9. The well rates and water cut also show the same performance for MsDS as DSQ method both of which are slightly accurate than MsMFEM (Figure 7.10). The similarity of performance for MsMFEM and MsDS is expected for a fairly continuous low contrast example such as the current one.

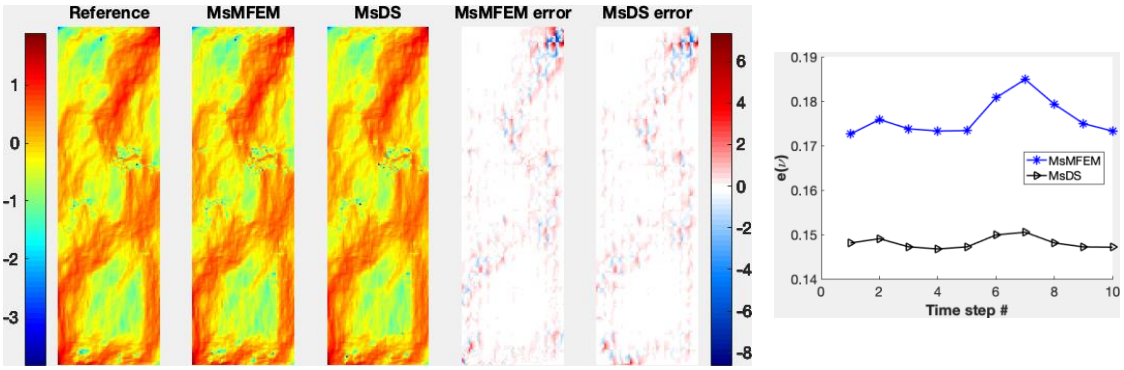

(a) Velocity profile **(b) Velocity error**

Figure 7.8: SPE10 layer 1 reconstructed fine scale velocity profiles at 1 PVI and the velocity error plot for MsMFEM and MsDS methods

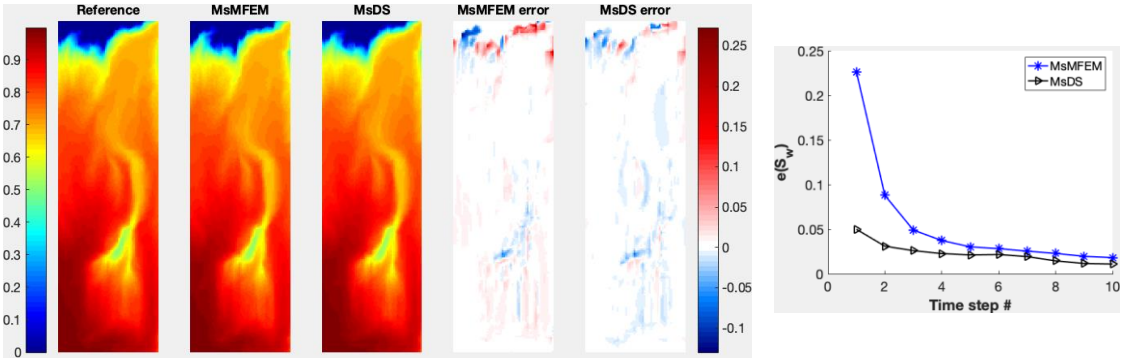

(a) Water saturation (Sw) profile **(b) Sw error**

Figure 7.9: SPE10 layer 1 water saturation profiles at 1 PVI and the Sw error plot for MsMFEM and MsDS methods

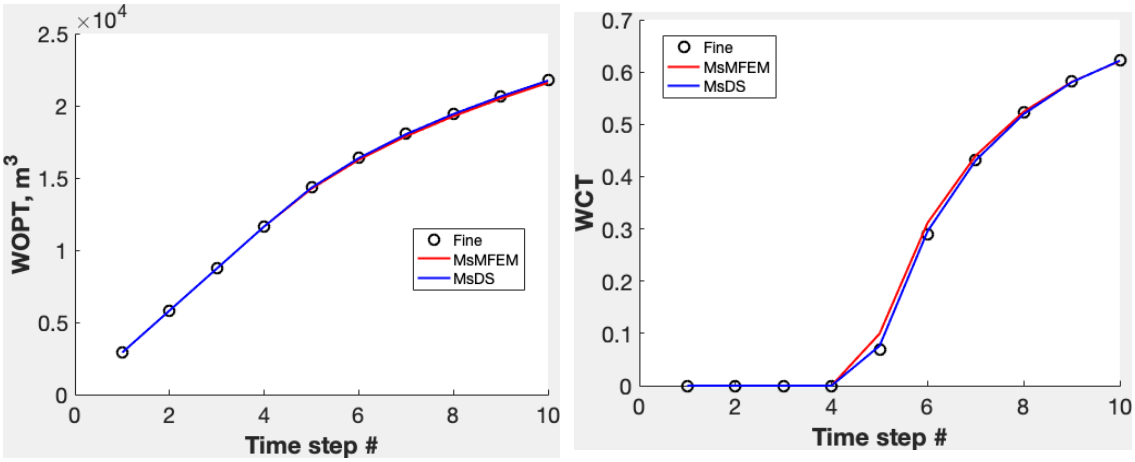

Figure 7.10: SPE10 layer 1 cumulative oil production and water cut for MsMFEM and MsDS methods

Now, the multiscale methods are tested on a high contrast channelized layer 68 of the SPE10 model (Figure 7.11). The permeability histogram in Figure 7.11a shows a bimodal distribution which is also evident in the two different clusters in the cross plot of permeability and porosity in semi log scale (Figure 7.11b). The clusters correspond to channel and non-channel features. The simulation input data is the same as the previous case with an injector-producer pair at the corners.

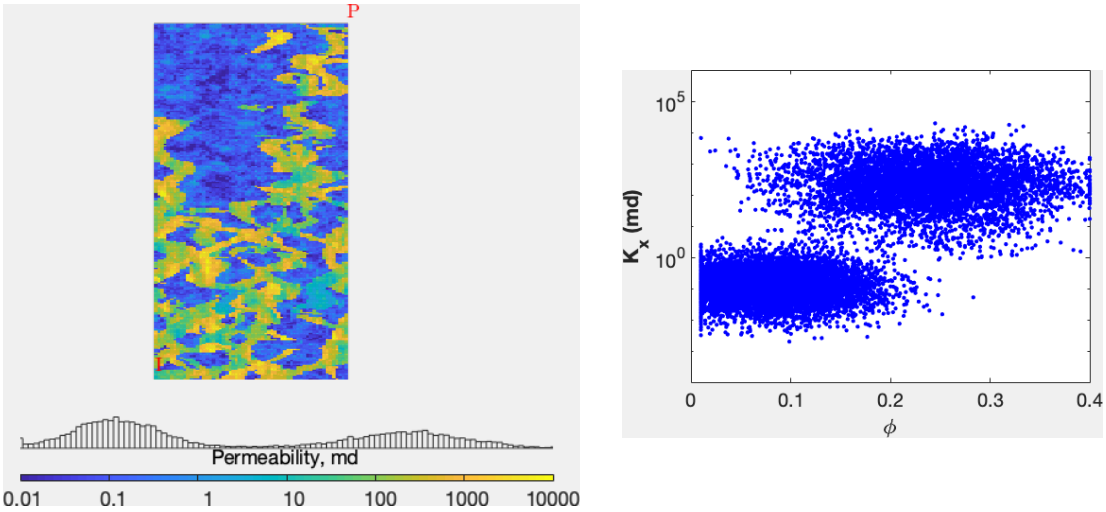

(a) Permeability **(b) Permeability vs porosity**

Figure 7.11: SPE10 layer 68 properties used for multiscale simulation

Figure 7.12 and Figure 7.13 show the velocity and water saturation profiles and their corresponding errors for the MsMFEM and DSQ methods. Both the reconstructed velocity and water saturation profiles show lower error for DSQ over MsMFEM. However, the cumulative oil production and the water cut profiles show better performance for MsMFEM over DSQ method (Figure 7.14). This indicates the source of error is the well index upscaling as the wells are located in the corners of the coarse block.

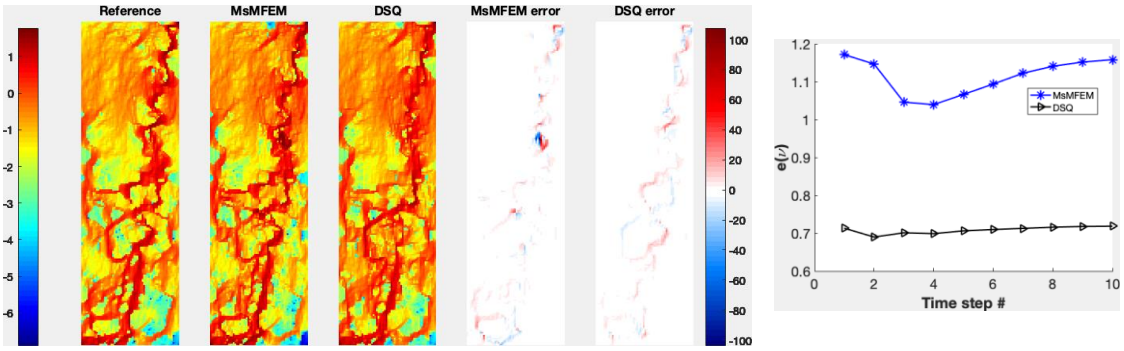

(a) Velocity profile **(b) Velocity error**

Figure 7.12: SPE10 layer 68 reconstructed fine scale velocity profiles at 1 PVI and the velocity error plot for MsMFEM and DSQ methods

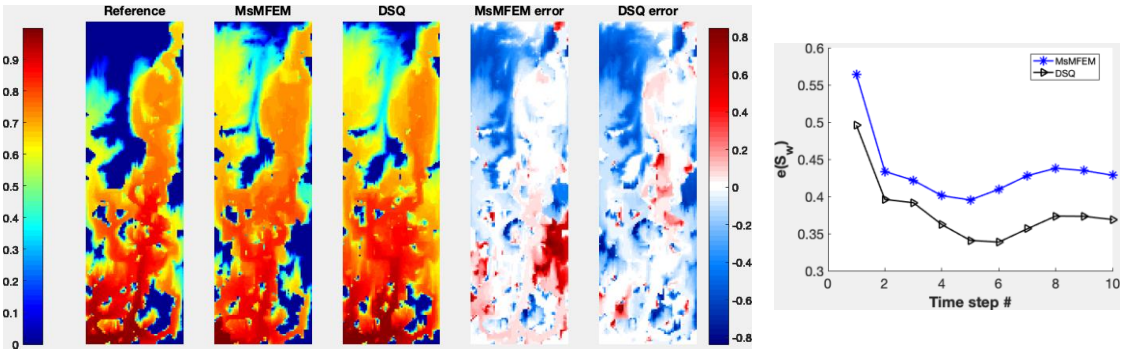

(a) Water saturation (Sw) profile **(b) Sw error**

Figure 7.13: SPE10 layer 68 water saturation profiles at 1 PVI and the Sw error plot for MsMFEM and DSQ methods

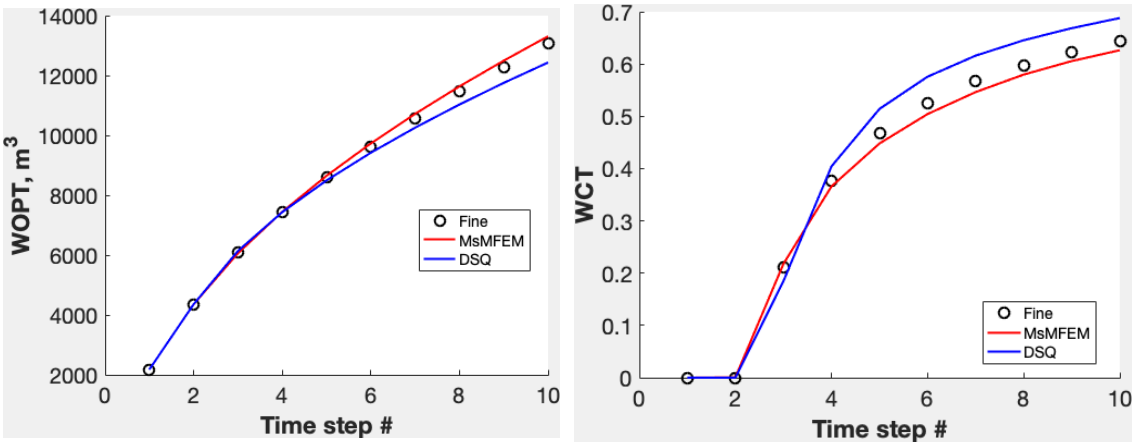

Figure 7.14: SPE10 layer 68 cumulative oil production and water cut for MsMFEM and DSQ methods

The MsDS method shows a much better performance than both DSQ and MsMFEM methods as shown in Figure 7.15 and Figure 7.16 for velocity and water saturation profile respectively. The spatial footprint of saturation error is very different for MsDS compared to MsMFEM. MsMFEM overestimates the water saturation in the low permeability zone towards the top left of the model whereas MsDS shows relatively less discrepancy. Both the well rates and the water cut show similar performance for MsDS and MsMFEM (Figure 7.17).

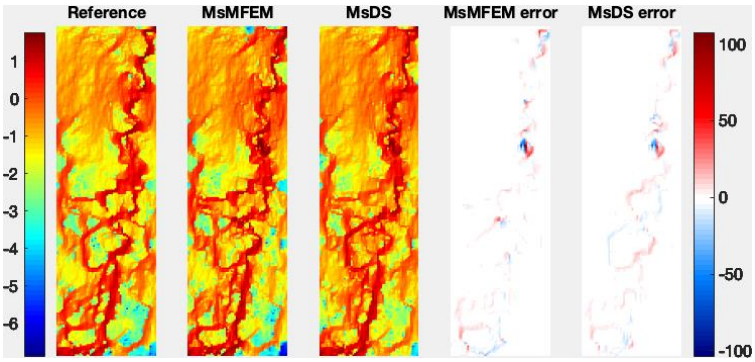

(a) Velocity profile **(b) Velocity error**

Figure 7.15: SPE10 layer 68 reconstructed fine scale velocity profiles at 1 PVI and the velocity error plot for MsMFEM and MsDS methods

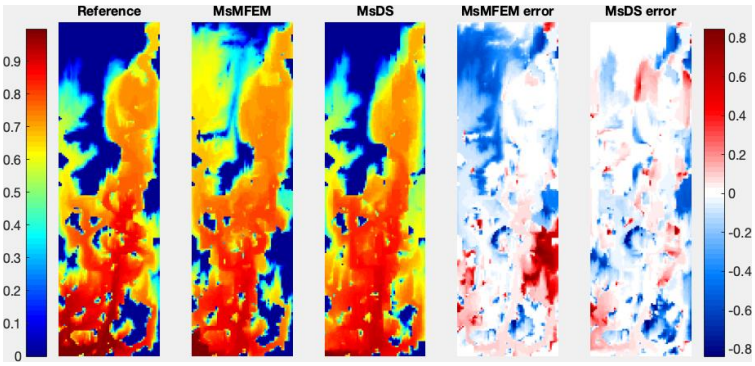

(a) Water saturation (Sw) profile **(b) Sw error**

Figure 7.16: SPE10 layer 68 water saturation profiles at 1 PVI and the Sw error plot for MsMFEM and MsDS methods

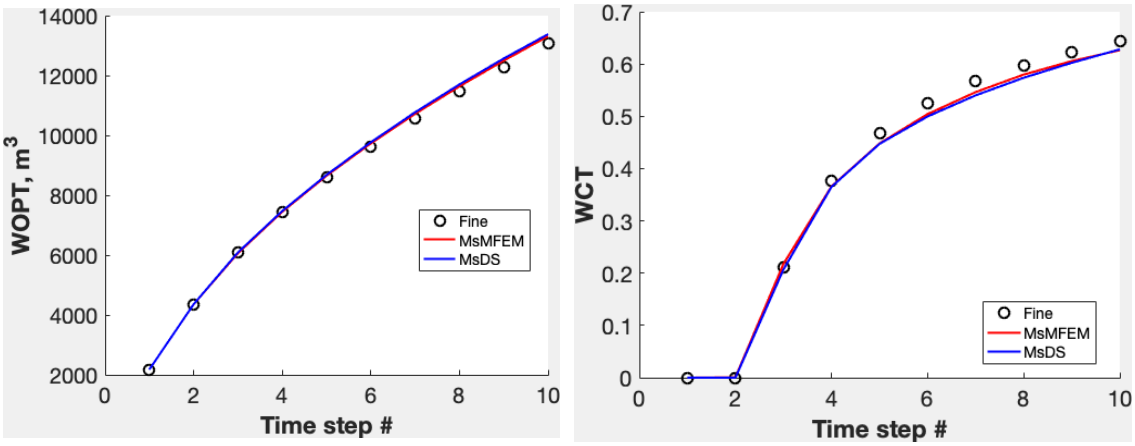

Figure 7.17: SPE10 layer 68 cumulative oil production and water cut for MsMFEM and MsDS methods

Overall, all the three methods that are tested show similar performance relative to the fine scale simulation. All the methods utilize source distributions to compute the basis functions. While MsMFEM responds to permeability, the MsDS and DSQ methods relies on the ratio of k/ϕ to generate the source functions. The source functions utilized in MsDS and DSQ methods are a direct consequence of the diffusivity equation which exploit the transient physics rather than the empirical source functions used in the current version of MsMFEM.

3D SPE10 Two Phase Flow

Two cases are considered for the 3D SPE10 model – the Tarbert formation (layers 1-35) and the Upper Ness (layers 36-85). The zones are described in Figure 3.13 and the permeability distribution is given in Figure 7.18. The simulation input data is the same as the above section. The coarsening ratio is $5\times10\times5$.

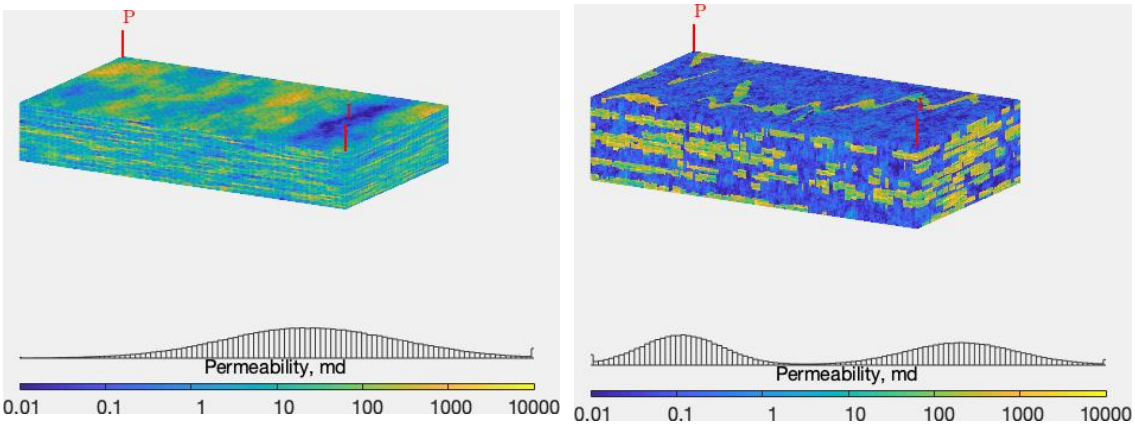

(a) Tarbert **(b) Upper Ness**

Figure 7.18: SPE10 permeability distributions for the two geologic zones

Figure 7.19 and Figure 7.20 represent the velocity and saturation profiles at the end of simulation for the DSQ method respectively for the Tarbert formation. The results for DSQ show higher accuracy over MsMFEM for velocity profile. However, the saturation error for MsMFEM is lower than DSQ although the difference is small which is evident from the velocity and saturation error plots in Figure 7.19 and Figure 7.20 respectively. The well rates and water cut profiles also show comparable predictions for both the multiscale methods (Figure 7.21).

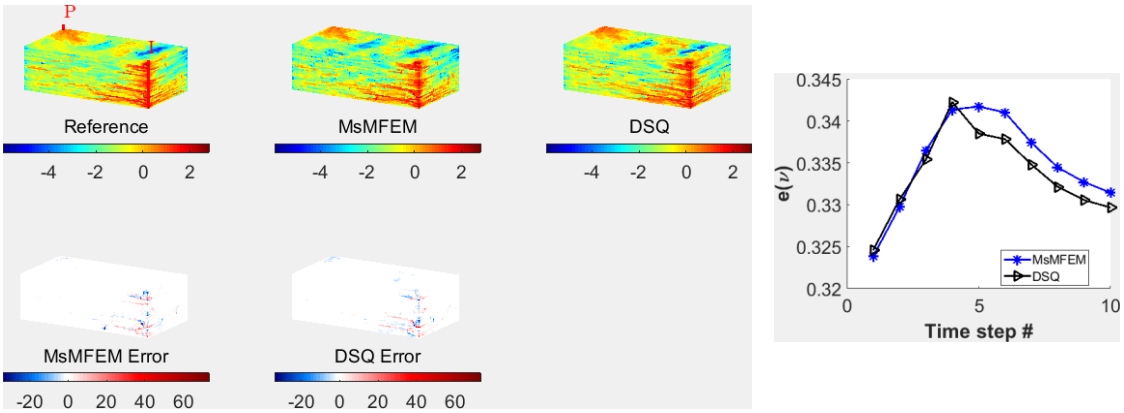

(a) Velocity profile **(b) Velocity error**

Figure 7.19: SPE10 Tarbert formation reconstructed fine scale velocity profiles at 1 PVI and the velocity error plot for MsMFEM and DSQ methods

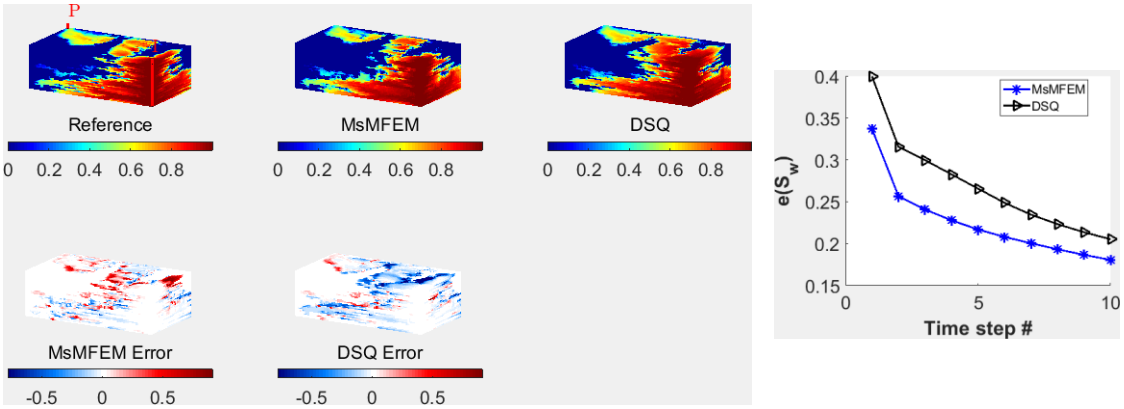

(a) Water saturation (Sw) profile **(b) Sw error**

Figure 7.20: SPE10 Tarbert formation water saturation profiles at 1 PVI and the Sw error plot for MsMFEM and DSQ methods

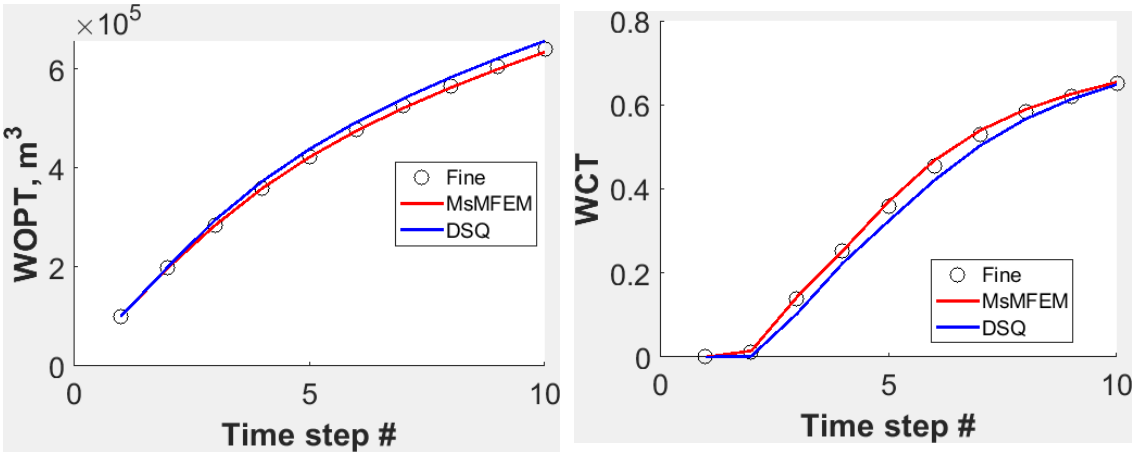

Figure 7.21: SPE10 Tarbert formation cumulative oil production and water cut for MsMFEM and DSQ methods

As seen in the 2D examples, MsDS shows slightly better performance over DSQ as seen in the velocity and water saturation profiles for the Tarbert formation simulation (Figure 7.22 and Figure 7.23). Both the velocity and water saturation errors are now comparable to MsMFEM and the well rates, water cut profiles also show an excellent match to the fine scale performance (Figure 7.24).

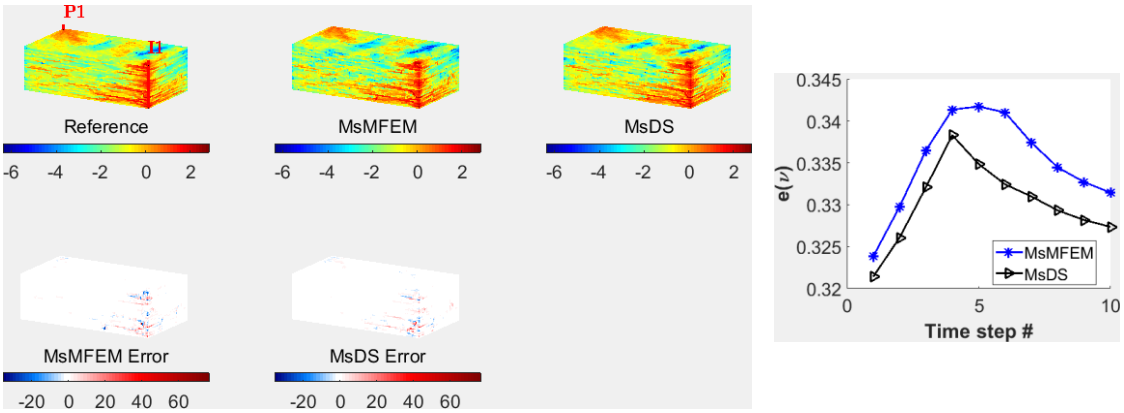

(a) Velocity profile **(b) Velocity error**

Figure 7.22: SPE10 Tarbert formation reconstructed fine scale velocity profiles at 1 PVI and the velocity error plot for MsMFEM and MsDS methods

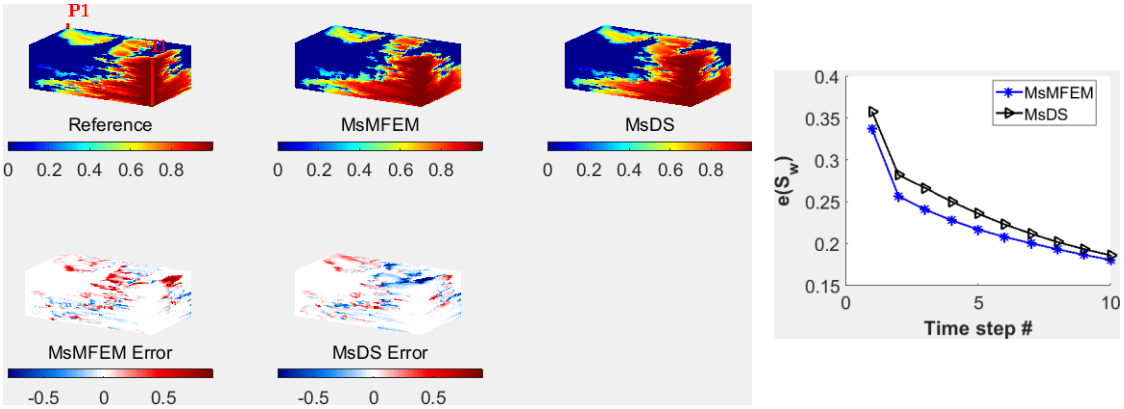

(a) Water saturation (Sw) profile **(b) Sw error**

Figure 7.23: SPE10 Tarbert formation water saturation profiles at 1 PVI and the Sw error plot for MsMFEM and MsDS methods

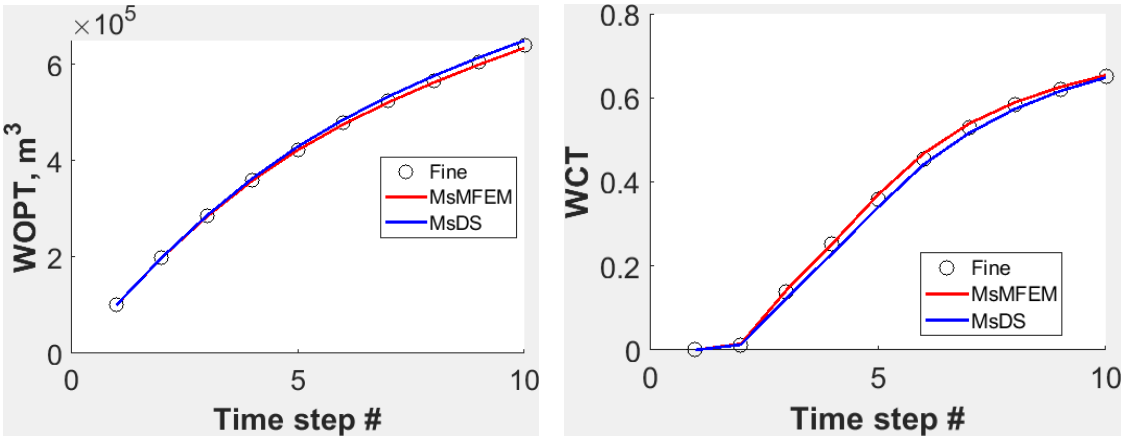

Figure 7.24: SPE10 Tarbert formation cumulative oil production and water cut for MsMFEM and MsDS methods

Now, the multiscale methods are tested on the Upper Ness formation which is the highly channelized fluvial unit in the lower section of the SPE10 model. Figure 7.25 and Figure 7.26 show the velocity and water saturation profiles for the DSQ method respectively. The DSQ method shows a higher error in velocity profiles which also shows up on the water saturation profile at the same places. However, the well rates show good agreement with the fine scale solution for both the multiscale methods (Figure 7.27).

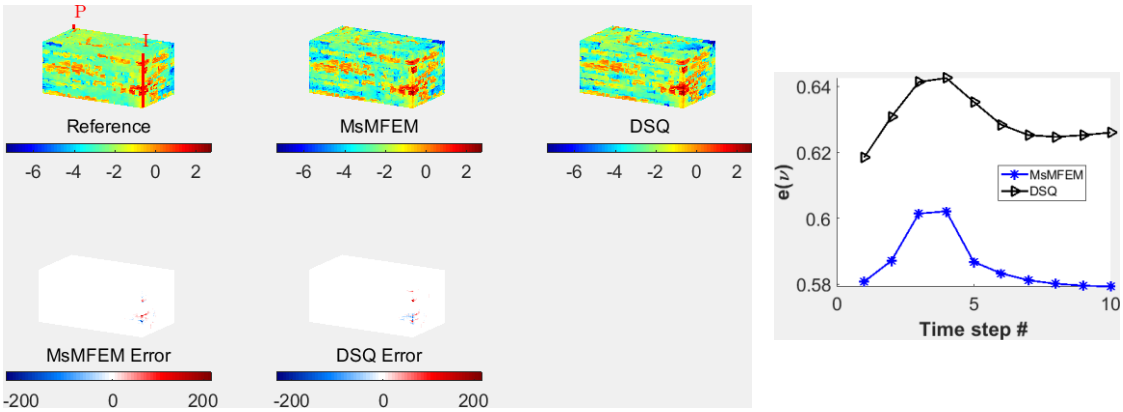

(a) Velocity profile **(b) Velocity error**

Figure 7.25: SPE10 Upper Ness formation reconstructed fine scale velocity profiles at 1 PVI and the velocity error plot for MsMFEM and DSQ methods

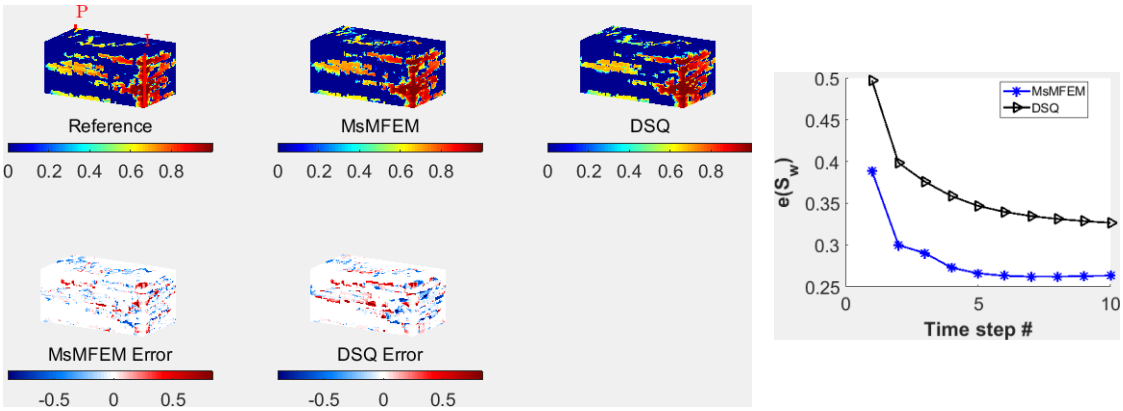

(a) Water saturation (Sw) profile **(b) Sw error**

Figure 7.26: SPE10 Upper Ness formation water saturation profiles at 1 PVI and the Sw error plot for MsMFEM and DSQ methods

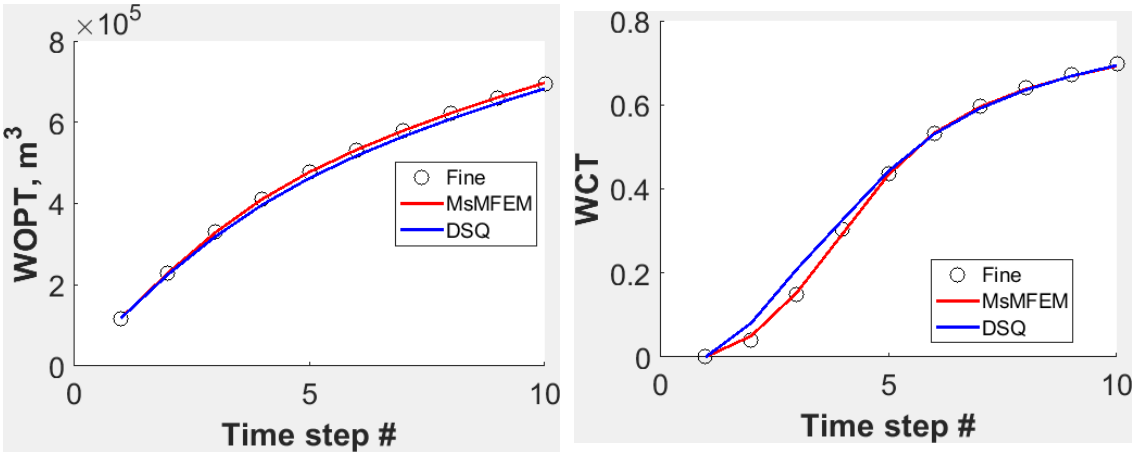

Figure 7.27: SPE10 Upper Ness formation cumulative oil production and water cut for MsMFEM and DSQ methods

The performance of MsDS is again better than DSQ as shown in Figure 7.28, Figure 7.29 and Figure 7.30. The 3D water saturation error and the well rate, water cut prediction of MsDS is relatively closer to the fine scale performance than DSQ. The MsMFEM seems to performing consistently well for all the cases tested here.

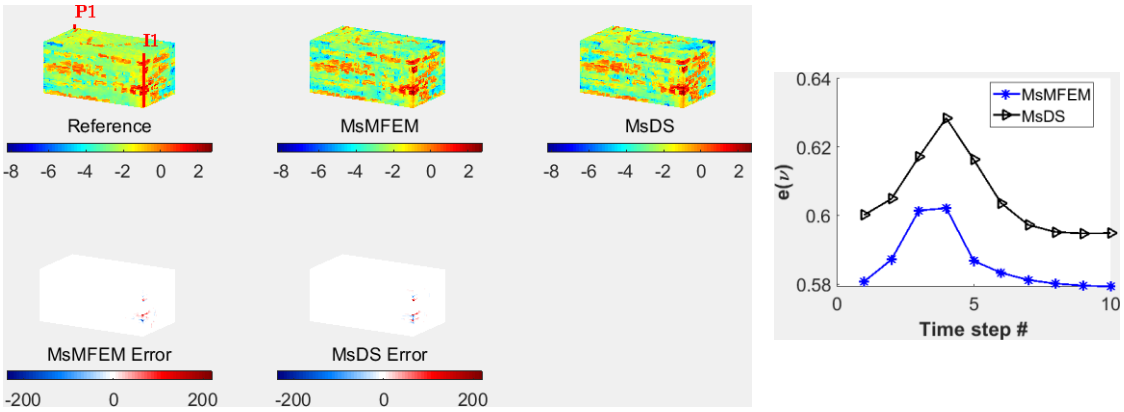

(a) Velocity profile **(b) Velocity error**

Figure 7.28: SPE10 Upper Ness formation reconstructed fine scale velocity profiles at 1 PVI and the velocity error plot for MsMFEM and MsDS methods

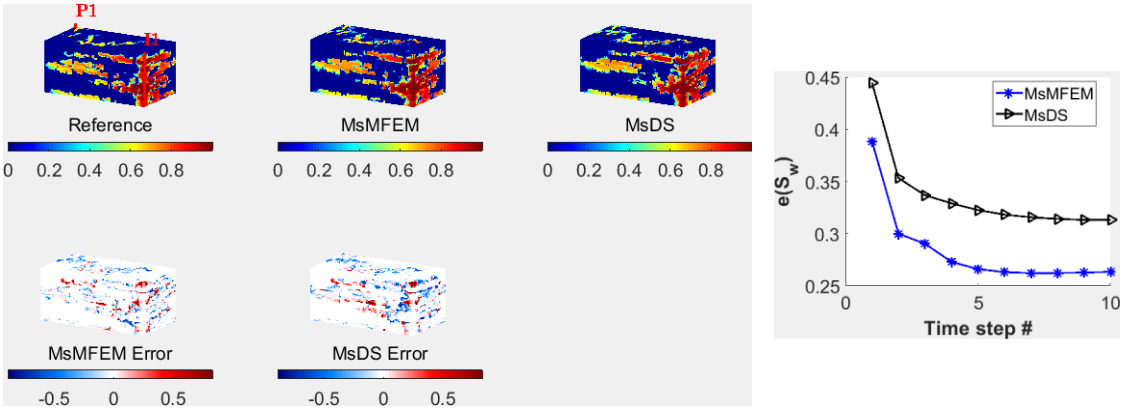

(a) Water saturation (Sw) profile **(b) Sw error**

Figure 7.29: SPE10 Upper Ness formation water saturation profiles at 1 PVI and the Sw error plot for MsMFEM and MsDS methods

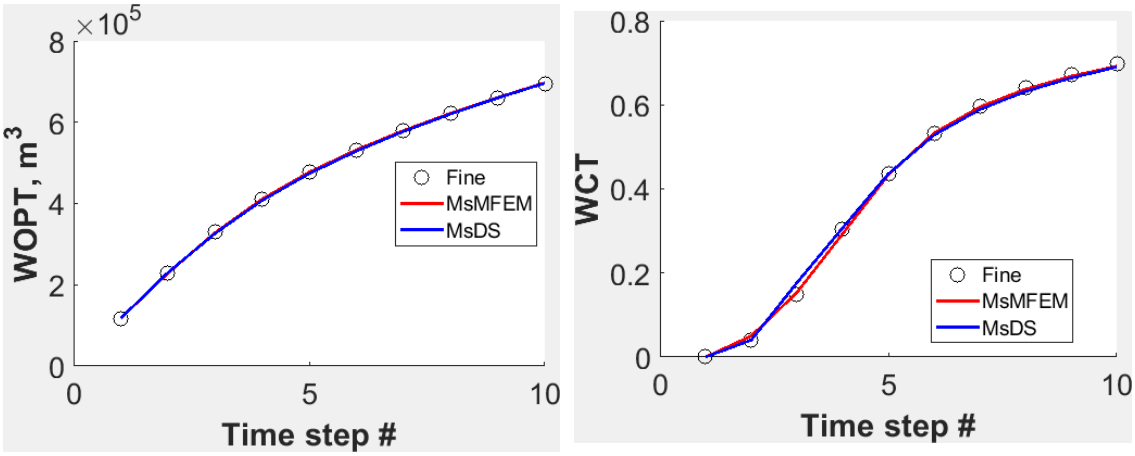

Figure 7.30: SPE10 Upper Ness formation cumulative oil production and water cut for MsMFEM and MsDS methods

Overall, MsMFEM which relies on source distributions based on permeability gives the most accurate multiscale description for the 3D cases. This may be due permeability alone giving better source distributions for incompressible flow compared to porosity on which the DSQ and MsDS methods rely on. In fact, the incompressible flow formulation is independent of porosity and it shows up only while solving the transport. Nevertheless, the performance of transient MsDS is very much comparable to MsMFEM even though for incompressible flow.

7.2 Multiscale Diffuse Source (MsDS) Method – Compressible Flow

The governing flow and transport equations for compressible flow are written in terms of total velocity and water saturation given by Eq.(7.11) and Eq.(7.12) respectively. Here, c_o, c_w, f_o, f_w represent the oil, water compressibilities and fractional flows respectively, $b_w = 1/B_w$ is the inverse of the formation volume factor of water.

$$\nabla \cdot \vec{u} + \left(c_o f_0 + c_w f_w\right)\vec{u} \cdot \nabla p + \phi \mu c_t \frac{\partial p}{\partial t} = q_{total} \tag{7.11}$$

$$\nabla \cdot f_w \vec{u} + c_w f_w \nabla p \cdot \vec{u} + \phi \frac{\partial S_w}{\partial t} + \phi S_w (c_w + c_o) \frac{\partial p}{\partial t} = \frac{q_w}{b_w} \tag{7.12}$$

Notice in Eq.(7.12), the transport solution depends both on velocity as well as pressure unlike the incompressible flow case (Eq.(7.2)). Hence, for the application of MsDS method to compressible, subscale variation in pressure also must be specified making it a challenging problem. Krogstad et al. 2009 and Lie, K.-A. et al. 2012 proposed the pressure basis of the form Eq.(7.13) so that flux and pressure basis scale similarly. Here, $\Lambda = diag\left(\lambda_i^0 / \lambda_i\right)$ is a diagonal matrix of the ratio of initial to current mobility so that the average mobility change is accounted. Here, Φ is the pressure basis matrix per each shared coarse face of the size, number of fine cells by number of coarse faces $\left(n_c \times N_f\right)$. This pressure downscaling approach does not guarantee pressure continuity on the fine scale.

$$p = Ip_c + \Lambda \Phi q_c \tag{7.13}$$

Herein, the upscaling-downscaling workflow proposed in the previous section is utilized for multiscale compressible flow application. The fine scale velocities are reconstructed using Eq. (7.4) and three variants of pressure downscaling are tested: retain the same formulation as incompressible flow, use Eq. (7.13) to downscale the coarse pressures using pressure basis matrix and the last one based on treating the coarse cell pressure as the pore volume average of the fine scale pressure as explained below. The

fine scale pressure of cell ℓ is written in terms of a constant c and the superposition of pressure drops with respect to a gauge pressure weighted by the face flux (Eq.(7.14)).

$$p_\ell = c + \sum_{i \in faces_\ell} \Delta_i p_\ell \tag{7.14}$$

Eq.(7.14) is then integrated over the coarse block giving an equation for the constant c (Eq.(7.15)).

$$\sum_\ell p_\ell PV_\ell = p_c \sum_\ell PV_\ell = c \sum_\ell PV_\ell + \sum_\ell PV_\ell \sum_{i \in faces_\ell} \Delta_i p_\ell$$
$$c = p_c - \frac{\sum_\ell PV_\ell \sum_{i \in faces_\ell} \Delta_i p_\ell}{\sum_\ell PV_\ell} \tag{7.15}$$

The final equation for pressure downscaling now reads:

$$p_\ell = p_c + \sum_{i \in faces_\ell} \Delta_i p_\ell - \frac{\sum_\ell PV_\ell \sum_{i \in faces_\ell} \Delta_i p_\ell}{\sum_\ell PV_\ell} \tag{7.16}$$

Eq.(7.16) is similar to Eq. (7.13) with one additional term which represent the pore volume average of the pressure drops computed from the basis functions.

7.2.1 Numerical Experiments

The compressible flow formulation is tested on 2D examples taken from the lower and upper geologic units of the SPE10 model (Figure 7.31). The well configurations and the fluid, rock data are left to the default values of the SPE10 data set. The model has one central water injector maintained at a rate constraint of 5000 bbl/day and four corner

producers at a constant bottomhole pressure of 4000 psia. The initial reservoir pressure is 6000 psia. The coarsening ratio is 5×10 and the simulation time is 5 years.

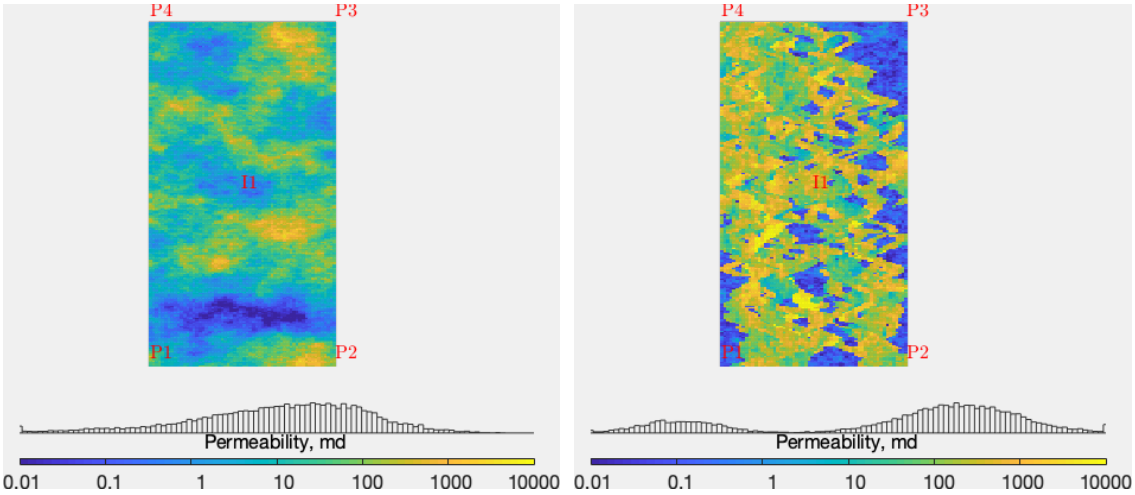

(a) Layer 1 **(b) Layer 85**

Figure 7.31: SPE10 permeability map for layers 1, 85 with one central injector and four producers

The pressure downscaling based on Eq. (7.13) and Eq. (7.16) resulted in numerical instabilities when solving the transport. Therefore, the pressure downscaling was done by simply resampling the coarse pressure uniformly on to the fine scale. The DSQ upscaling approach is used as another reference for the MsDS compressible flow formulation.

Figure 7.32, Figure 7.33 and Figure 7.34 represent the reconstructed fine scale velocity profile, water saturation profile and the cumulative oil volumes, producer water cuts for SPE10 layer 1 respectively. The saturation resolution for MsDS clearly improved from the coarse scale as seen in Figure 7.33. However, there seems to be only slight

improvement in well rates and water cut compared to the DSQ upscaling approach (Figure 7.34). Both the upscaling and the multiscale methods show early water breakthrough relative to fine scale for producers P1 and P4.

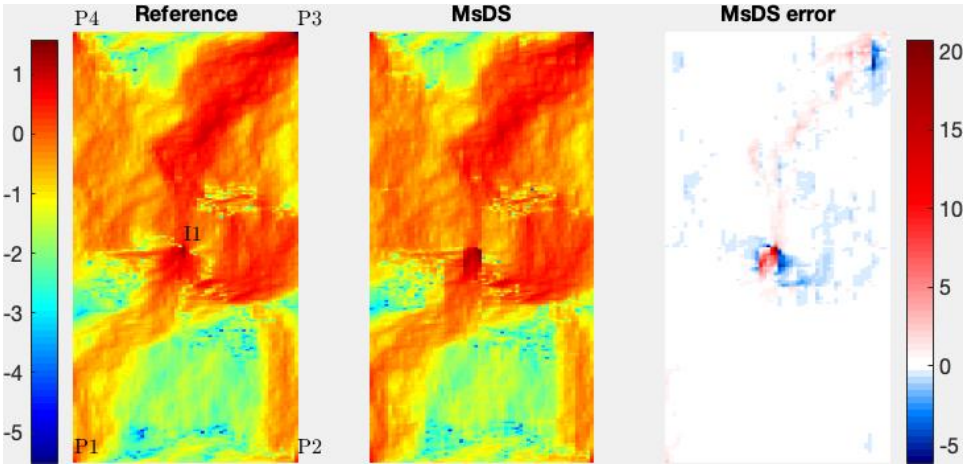

Figure 7.32: SPE10 layer 1 reconstructed fine scale velocity after 5 years for slightly compressible flow

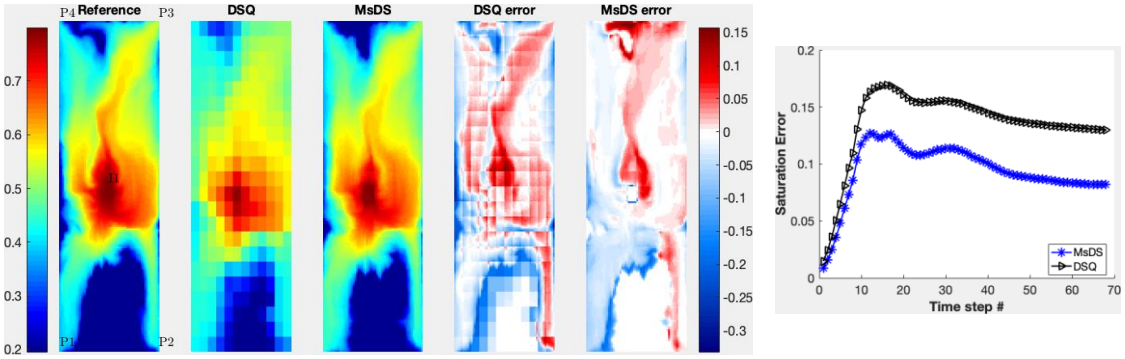

(a) Water saturation (Sw) profile **(b) Sw error**

Figure 7.33: SPE10 layer 1 water saturation profiles after 5 years and the Sw error plot for DSQ upscaling and MsDS methods

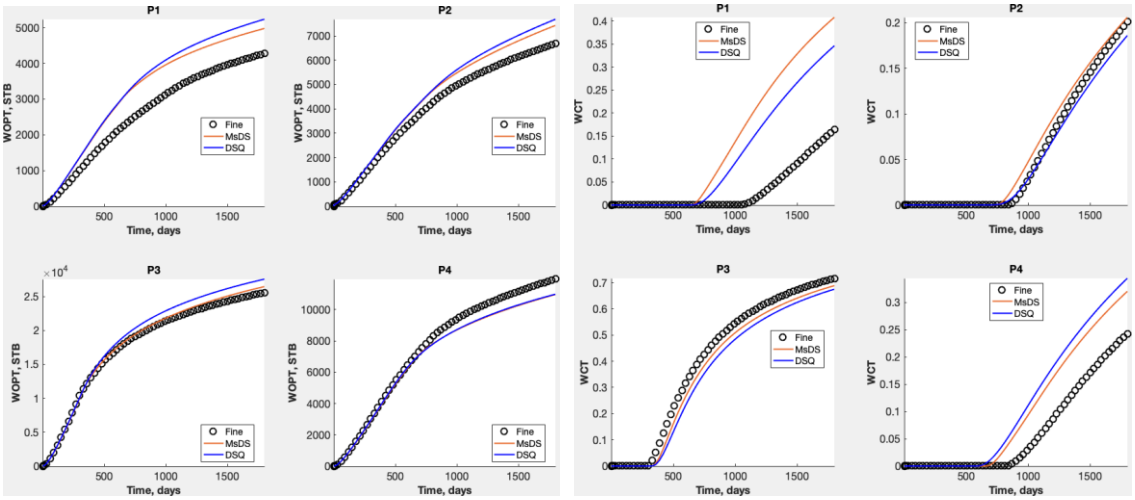

(a) Cumulative oil production **(b) Producer water cut**

Figure 7.34: SPE10 layer 1 cumulative oil volumes and water cut for slightly compressible flow

Figure 7.35, Figure 7.36 and Figure 7.37 represent the reconstructed fine scale velocity profile, water saturation profile and the cumulative oil volumes, producer water cuts for SPE10 layer 85 respectively. For the high contrast channelized layer 85, MsDS formulation shows improvement over the DSQ upscaling method not only with respect to the saturation profile (Figure 7.36) but also the well rates and water cut plots shown in Figure 7.37. The water cut plots for producers P1 and P3 are omitted as they did not experience water breakthrough by the end of simulation (Figure 7.37b).

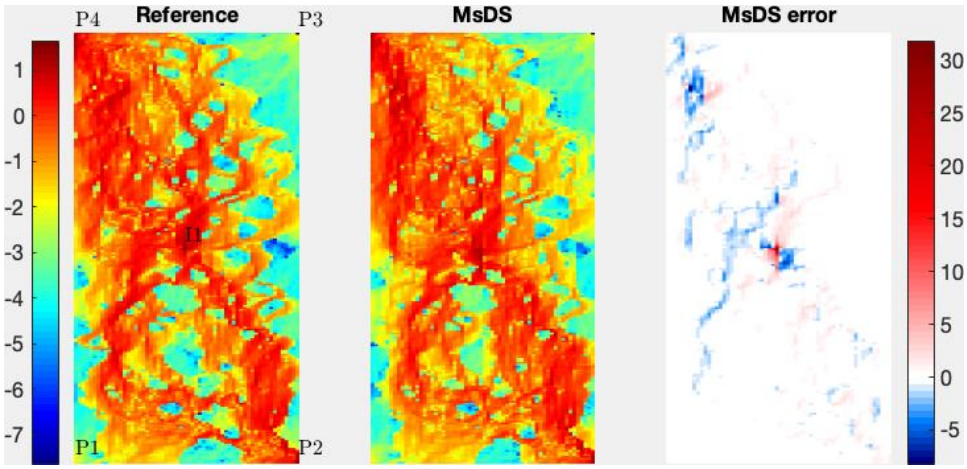

Figure 7.35: SPE10 layer 85 reconstructed fine scale velocity after 5 years for slightly compressible flow

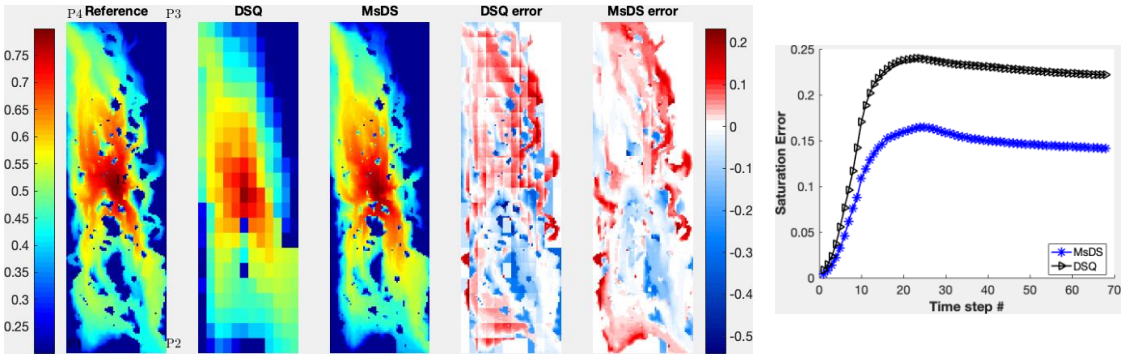

(a) Water saturation (Sw) profile **(b) Sw error**

Figure 7.36: SPE10 layer 85 water saturation profiles after 5 years and the Sw error plot for DSQ upscaling and MsDS methods

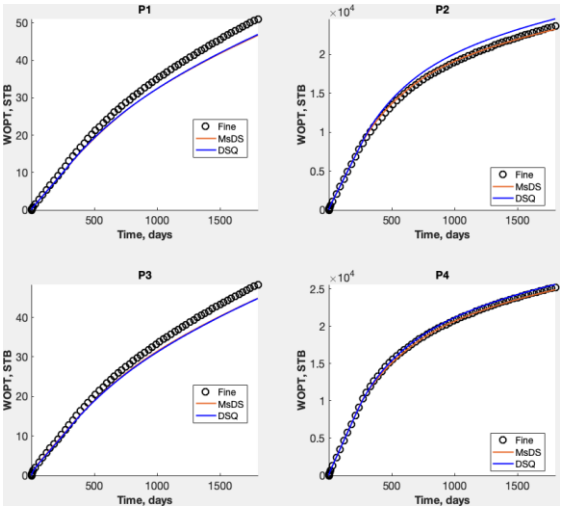

(a) Cumulative oil production

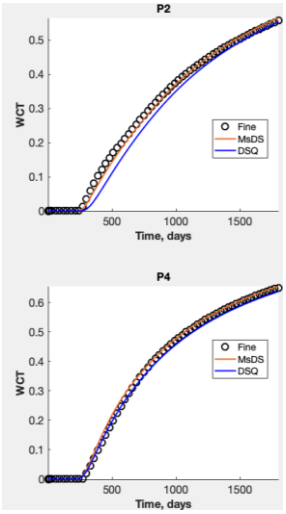

(b) Producer water cut

Figure 7.37: SPE10 layer 85 cumulative oil volumes and water cut for slightly compressible flow

7.3 Discussion

The PSS/DS upscaling formulation is extended to multiscale framework in this chapter. Two variants of the multiscale formulation were proposed for incompressible flow – the upscaling-downscaling workflow and the multiscale diffuse source workflow. The use of transient DS formulation for incompressible flow does not guarantee flux continuity on the fine scale. Therefore, the downscaling work for incompressible flow was performed using PSS basis functions even though the coarse solution is based on the transient basis functions. The applications to 2D and 3D SPE10 cases showed that the multiscale diffuse source formulation gives better reconstruction on the fine scale compared to the upscaling-downscaling workflow. All the test cases show the multiscale workflow results comparable to the benchmarked MsMFEM where the source

distributions are based on the cell permeability as opposed to the porosity for DSQ and MsDS. The multiscale framework proposed here is only an approximation to the fine scale problem and does not necessarily converge to the fine scale solution. In order to converge to the fine scale solution, an iterative framework may be employed.

The application of the proposed multiscale framework to compressible flow requires the subscale variation of pressure also to be specified along with the velocity. For incompressible flow, the pressure is immaterial as the saturations depend only on the fine scale velocities. Therefore, the extra computational effort for specifying the pressure basis is avoided by specifying a piecewise uniform basis. In the current work, the pressure basis for compressible flow is retained to be the same as the incompressible flow since the proposed alternatives failed to converge while solving the saturations. This is still a first attempt in extending the mixed multiscale framework to compressible flow. Further research is required to make the algorithm stable and more applicable to realistic cases with complex physics.

CHAPTER VIII

SUMMARY AND CONCLUSIONS: MULTISCALE SIMULATION

8.1 Summary and Conclusions

A new multiscale framework is proposed using pressure transient diffuse source basis functions. The formulation is tested with incompressible and slightly compressible flow using SPE10 model.

For incompressible flow, two workflows were evaluated:

- Upscaling-downscaling workflow where coarse transmissibilities are calculated using DSQ upscaling and the downscaling is performed using the basis functions computed while upscaling.
- Multiscale diffuse source workflow (MsDS) where the coarse set of equations are directly formulated using the basis functions.

The numerical experiments on SPE10 model showed similar performance for both MsDS and the benchmarked MsMFEM while the DSQ upscaling-downscaling formulation showed slightly less accurate performance.

For compressible flow, a first attempt was made to formulate the multiscale framework where the subscale pressure variation was neglected and the upscaling-downscaling formulation was used. The results showed only a slight improvement compared to DSQ upscaling approach although the saturations were resolved on a higher resolution using the multiscale approach.

8.2 Future Research

The multiscale formulation for incompressible flow was tested on simplistic grid geometries in the current work. However, the mixed formulation allows a natural extension to more general unstructured grids since the basis functions are completely localized and are constructed for a shared face. Unlike the multiscale finite volume method, there is no need to work with a dual grid and define the coarse cell centers. Therefore, the multiscale diffuse source formulation may be tested on complex grids.

The compressible flow formulation experienced numerical instabilities due to discontinuous pressures on the fine scale. This area may be further explored by modifying the formulation so that the subscale variation in pressure is also included. A different pressure basis may be specified other than the piece wise uniform basis utilized in the current work. It would be even more beneficial if the entire framework is based solely on pressure rather than the mixed framework of velocity and pressure. An approach which combines the geometric adaptability of the mixed methods and the robustness of finite volume methods in complex physical scenarios is the ideal one which combines the best of both approaches. The current work is purely based on the mixed framework. However, it is more advantageous to have a formulation based on pressure basis as demonstrated by Møyner and Lie 2016a for the multiscale restricted smooth basis method which is inspired from the multigrid literature.

NOMENCLATURE

Property	Description	Unit of Measure	Conversion to SI
Symbols			
A	Cross sectional area	ft^2	$(0.3048)^2\ m^2$
c_t	Total compressibility	$1/psi$	$(1/6894.76)/Pa$
DX	Length of grid block in x direction	ft	$0.3048\ m$
DY	Length of grid block in y direction	ft	$0.3048\ m$
f_w	Fractional flow of water	$[1]$	
h	Thickness	ft	$0.3048\ m$
I	Injection matrix		
k	Permeability	mD	$9.869233\times10^{-16} m^2$
k_{eff}	Effective permeability	mD	$9.869233\times10^{-16} m^2$
k_r	Relative permeability	$[1]$	
$\vec{n}$	Normal vector	ft^2	$(0.3048)^2\ m^2$
p	Pressure	psi	$6.89476\times10^3 Pa$

Property	Description	Unit of Measure	Conversion to SI
p_f	Face pressure	psi	$6.89476\times10^3 Pa$
$\bar{p}$	Average pressure	psi	$6.89476\times10^3 Pa$
$\langle p \rangle$	Bulk volume averaged pressure	psi	$6.89476\times10^3 Pa$
p_{wf}	Bottomhole pressure	psi	$6.89476\times10^3 Pa$
p_i	Pressure in grid block i	psi	$6.89476\times10^3 Pa$
p_o	Well cell pressure	psi	$6.89476\times10^3 Pa$
PV_i	Pore volume of grid block i	ft^3	$(0.3048)^3 m^3$
P	Prolongation operator		
q	Flux	ft^3/day	$\left((0.3048)^3/24\right)m^3/hr$
$\hat{q}$	Normalized flux	$[1]$	
q_w	Well flux	ft^3/day	$\left((0.3048)^3/24\right)m^3/hr$
q_{face}	Total face flux	ft^3/day	$\left((0.3048)^3/24\right)m^3/hr$
q_{PSS}	Pseudo steady state flux	ft^3/day	$\left((0.3048)^3/24\right)m^3/hr$
q_{SS}	Steady state flux	ft^3/day	$\left((0.3048)^3/24\right)m^3/hr$

Property	Description	Unit of Measure	Conversion to SI
r	Radial distance	ft	$0.3048\,m$
r_o	Equivalent grid block radius	ft	$0.3048\,m$
r_w	Wellbore radius	ft	$0.3048\,m$
R	Restriction operator		
S_w	Water saturation	$[1]$	
t	Time	hr	hr
t_{Char}	Characteristic time	hr	hr
t_{LOD}	Time at the limit of detectability	hr	hr
t_{PSS}	Time to reach pseudo steady state	hr	hr
T	Intercell transmissibility	$mD \cdot ft$	$(9.869233)(0.3048)\times 10^{-16} m^3$
T^{Cell}	Cell transmissibility	$mD \cdot ft$	$(9.869233)(0.3048)\times 10^{-16} m^3$
T^{Half}	Half cell transmissibility	$mD \cdot ft$	$(9.869233)(0.3048)\times 10^{-16} m^3$

Property	Description	Unit of Measure	Conversion to SI
T^{eff}	Effective transmissibility	$mD \cdot ft$	$(9.869233)(0.3048)\times 10^{-16} m^3$
T_ℓ	Intercell transmissibility in the direction ℓ	$mD \cdot ft$	$(9.869233)(0.3048)\times 10^{-16} m^3$
$\vec{u}$	Darcy velocity vector	ft/day	$(0.3048/24)\, m/hr$
u_r	Darcy velocity in the radial direction	ft/day	$(0.3048/24)\, m/hr$
u_θ	Darcy velocity in the azimuthal direction	ft/day	$(0.3048/24)\, m/hr$
V_p	Pore volume	ft^3	$(0.3048)^3\, m^3$
$V(t)$	Transient drainage volume	ft^3	$(0.3048)^3\, m^3$
WI	Well index	$mD \cdot ft$	$(9.869233)(0.3048)\times 10^{-16} m^3$
WI^{eff}	Effective coarse well index	$mD \cdot ft$	$(9.869233)(0.3048)\times 10^{-16} m^3$
x_c	1D cell center location	ft	$0.3048\, m$

Property	Description	Unit of Measure	Conversion to SI
Greek			
α	Hydraulic diffusivity	ft^2/hr	$(0.3048)^2\ m^2/hr$
$\Delta\bar{p}_{SS}$	Pore volume averaged steady state pressure drop	psi	$6.89476\times10^3 Pa$
Δp_{DS}	Diffuse source pressure drop	psi	$6.89476\times10^3 Pa$
Δp_{PSS}	Pseudo steady state pressure drop	psi	$6.89476\times10^3 Pa$
ϕ	Porosity	$[1]$	
ϕ_i	Pressure basis		
Φ	Dual grid pressure basis		
ω	Frequency domain		
Ω	Domain of interest		
μ	Fluid viscosity	cp	$10^{-3} Pa\cdot\sec$
λ_{rt}	Total relative mobility ratio	cp^{-1}	$10^3\left(Pa\cdot\sec\right)^{-1}$
Λ	Mobility ratio matrix		
ψ	Flux basis		
Ψ	Flux basis matrix		
τ	Diffusive time of flight	$\sqrt{hr}$	$\sqrt{hr}$

Property	Description	Unit of Measure	Conversion to SI
τ_e	Diffusive time of flight to the edge	$\sqrt{hr}$	$\sqrt{hr}$
τ_j	Diffusive time of flight of cell j	$\sqrt{hr}$	$\sqrt{hr}$
$\bar{\tau}$	Average diffusive time of flight	$\sqrt{hr}$	$\sqrt{hr}$
$\tau_{\min}$	Minimum diffusive time of flight	$\sqrt{hr}$	$\sqrt{hr}$
θ	Azimuthal angle	*radians*	*radians*

Abbreviations

1D	One dimensional
2D	Two dimensional
3D	Three dimensional
ALG	Adaptive local global
APSS	Approximate Pseudo Steady State
DOI	Depth of Investigation
DS	Diffuse Source
EL	Extended Local
FGPT	Field Gas Production Total

FMM	Fast Marching Method
FOPT	Field Oil Production Total
LOD	Limit of Detectability
MMSCF	Million Standard Cubic Feet
MsDS	Multiscale Diffuse Source
MsFEM	Multiscale Finite Element Method
MsFVM	Multiscale Finite Volume Method
MsMFEM	Multiscale Mixed Finite Element Method
MsRSB	Multiscale Restricted Smooth Basis
PSS	Pseudo Steady State
SS	Steady State
STB	Stock Tank Barrel
WCT	Water Cut
WOPT	Well Oil Production Total

REFERENCES

Aarnes, J.E. 2004. On the Use of a Mixed Multiscale Finite Element Method for Greaterflexibility and Increased Speed or Improved Accuracy in Reservoir Simulation. *Multiscale Modeling & Simulation* **2** (3): 421-439. DOI: https://doi.org/10.1137/030600655

Aarnes, J.E., Krogstad, S., and Lie, K.-A. 2006. A Hierarchical Multiscale Method for Two-Phase Flow Based Upon Mixed Finite Elements and Nonuniform Coarse Grids. *Multiscale Modeling & Simulation* **5** (2): 337-363. DOI: 10.1137/050634566

Aarnes, J.E., Krogstad, S., and Lie, K.-A. 2008. Multiscale Mixed/Mimetic Methods on Corner-Point Grids. *Computational Geosciences* **12** (3): 297-315. DOI: 10.1007/s10596-007-9072-8

Alpak, F.O. 2015. Quasiglobal Multiphase Upscaling of Reservoir Models with Nonlocal Stratigraphic Heterogeneities. *SPE Journal*. DOI: 10.2118/170245-PA

Alpak, F.O., Pal, M., and Lie, K.-A. 2012. A Multiscale Adaptive Local-Global Method for Modeling Flow in Stratigraphically Complex Reservoirs. *SPE Journal*. DOI: 10.2118/140403-PA

Arbogast, T. 2000. Numerical Subgrid Upscaling of Two-Phase Flow in Porous Media. In:35-49. Berlin, Heidelberg: Springer Berlin Heidelberg.ISBN 978-3-540-45467-0.

Arbogast, T. 2002. Implementation of a Locally Conservative Numerical Subgrid Upscaling Scheme for Two-Phase Darcy Flow. *Computational Geosciences* **6** (3): 453-481. DOI: 10.1023/a:1021295215383

Arbogast, T. and Bryant, S.L. 2002. A Two-Scale Numerical Subgrid Technique for Waterflood Simulations. *SPE Journal* **7** (04): 446-457. DOI: 10.2118/81909-PA

Aziz, K. and Settari, A. 1979. *Petroleum Reservoir Simulation*: Chapman & Hall. Original edition. ISBN 0853347875.

Bøe, Ø. 1994. Analysis of an Upscaling Method Based on Conservation of Dissipation. *Transport in Porous Media* **17** (1): 77-86. DOI: 10.1007/bf00624051

Brenier, Y. and Jaffre, J. 1991. Upstream Differencing for Multiphase Flow in Reservoir Simulation. *SIAM Journal on Numerical Analysis* **28** (3): 685-696. DOI: https://doi.org/10.1137/0728036

Brezzi, F., Douglas, J., and Marini, L.D. 1985. Two Families of Mixed Finite Elements for Second Order Elliptic Problems. *Numerische Mathematik* **47** (2): 217-235. DOI: 10.1007/bf01389710

Brezzi, F., Lipnikov, K., and Simoncini, V. 2005. A Family of Mimetic Finite Difference Methods on Polygonal and Polyhedral Meshes. *Mathematical Models and Methods in Applied Sciences* **15** (10): 1533-1551. DOI: 10.1142/s0218202505000832

Cardwell, W.T. and Parsons, R.L. 1945. Average Permeabilities of Heterogeneous Oil Sands. *Transactions of the American Institute of Mining and Metallurgical Engineers*. DOI: 10.2118/945034-G

Chen, Y. and Durlofsky, L.J. 2006. Adaptive Local–Global Upscaling for General Flow Scenarios in Heterogeneous Formations. *Transport in Porous Media* **62** (2): 157-185. DOI: 10.1007/s11242-005-0619-7

Chen, Y., Durlofsky, L.J., Gerritsen, M. et al. 2003. A Coupled Local–Global Upscaling Approach for Simulating Flow in Highly Heterogeneous Formations. *Advances in Water Resources* **26** (10): 1041-1060. DOI: https://doi.org/10.1016/S0309-1708(03)00101-5

Chen, Z. and Hou, T.Y. 2003. A Mixed Multiscale Finite Element Method for Elliptic Problems with Oscillating Coefficients. *Mathematics of Computation* **72** (242): 541-576.

Christie, M.A. 1996. Upscaling for Reservoir Simulation. *Journal of Petroleum Technology*. DOI: 10.2118/37324-JPT

Christie, M.A. and Blunt, M.J. 2001. Tenth Spe Comparative Solution Project: A Comparison of Upscaling Techniques. *SPE Reservoir Evaluation & Engineering*. DOI: 10.2118/72469-PA

Dagan, G. 2012. *Flow and Transport in Porous Formations*: Springer Science & Business Media. Original edition. ISBN 364275015X.

Deutsch, C. 1989. Calculating Effective Absolute Permeability in Sandstone/Shale Sequences. *SPE Formation Evaluation* **4** (03): 343-348. DOI: 10.2118/17264-PA

Dijkstra, E.W. 1959. A Note on Two Problems in Connexion with Graphs. *Numerische Mathematik* **1** (1): 269-271. DOI: 10.1007/bf01386390

Ding, Y. 1995. Scaling-up in the Vicinity of Wells in Heterogeneous Field.*SPE Reservoir Simulation Symposium, San Antonio, Texas*. 11. Society of Petroleum Engineers. DOI: 10.2118/29137-MS.

Durlofsky, L. and Chung, E. 1990. Effective Permeability of Heterogeneous Reservoir Regions. In *ECMOR II-2nd European Conference on the Mathematics of Oil Recovery*: EAGE.ISBN 2214-4609.

Durlofsky, L.J. 1991. Numerical Calculation of Equivalent Grid Block Permeability Tensors for Heterogeneous Porous Media. *Water resources research* **27** (5): 699-708. DOI: https://doi.org/10.1029/91WR00107

Durlofsky, L.J., Milliken, W.J., and Bernath, A. 2000. Scaleup in the near-Well Region. *SPE Journal*. DOI: 10.2118/61855-PA

Efendiev, Y. and Hou, T.Y. 2009. *Multiscale Finite Element Methods: Theory and Applications*: Springer Science & Business Media. Original edition. ISBN 0387094954.

Efendiev, Y.R. and Durlofsky, L.J. 2004. Accurate Subgrid Models for Two-Phase Flow in Heterogeneous Reservoirs. *SPE Journal*. DOI: 10.2118/88363-PA

Efendiev, Y.R., Hou, T.Y., and Wu, X.-H. 2000. Convergence of a Nonconforming Multiscale Finite Element Method. *SIAM Journal on Numerical Analysis* **37** (3): 888-910.

Farmer, C.L. 2002. Upscaling: A Review. *International Journal for Numerical Methods in Fluids* **40** (1 - 2): 63-78. DOI: 10.1002/fld.267

Fincham, A.E., Christensen, J.R., Barker, J.W. et al. 2004. Up-Gridding from Geological Model to Simulation Model: Review, Applications and Limitations.*SPE Annual Technical Conference and Exhibition, Houston, Texas*. 10. Society of Petroleum Engineers. DOI: 10.2118/90921-MS.

Gautier, Y., Blunt, M.J., and Christie, M.A. 1999. Nested Gridding and Streamline-Based Simulation for Fast Reservoir Performance Prediction. *Computational Geosciences* **3** (3): 295-320. DOI: 10.1023/a:1011535210857

Gomez-Hernandez, J.J. and Journel, A.G. 1994. Stochastic Characterization of Gridblock Permeabilities. *SPE Formation Evaluation* **9** (02): 93-99. DOI: 10.2118/22187-PA

Guerillot, D., Rudkiewicz, J., Ravenne, C. et al. 1990. An Integrated Model for Computer Aided Reservoir Description: From Outcrop Study to Fluid Flow Simulations. *Revue de l'Institut français du pétrole* **45** (1): 71-77.

Hajibeygi, H., Bonfigli, G., Hesse, M.A. et al. 2008. Iterative Multiscale Finite-Volume Method. *Journal of Computational Physics* **227** (19): 8604-8621. DOI: https://doi.org/10.1016/j.jcp.2008.06.013

Hajibeygi, H. and Jenny, P. 2009. Multiscale Finite-Volume Method for Parabolic Problems Arising from Compressible Multiphase Flow in Porous Media. *Journal of Computational Physics* **228** (14): 5129-5147. DOI: https://doi.org/10.1016/j.jcp.2009.04.017

Hajibeygi, H. and Jenny, P. 2011. Adaptive Iterative Multiscale Finite Volume Method. *Journal of Computational Physics* **230** (3): 628-643. DOI: https://doi.org/10.1016/j.jcp.2010.10.009

Hajibeygi, H., Karvounis, D., and Jenny, P. 2011. A Hierarchical Fracture Model for the Iterative Multiscale Finite Volume Method. *Journal of Computational Physics* **230** (24): 8729-8743. DOI: https://doi.org/10.1016/j.jcp.2011.08.021

Holden, L. and Lia, O. 1992. A Tensor Estimator for the Homogenization of Absolute Permeability. *Transport in Porous Media* **8** (1): 37-46. DOI: 10.1007/bf00616891

Holden, L. and Nielsen, B.F. 2000. Global Upscaling of Permeability in Heterogeneous Reservoirs: The Output Least Squares (Ols) Method. *Transport in Porous Media* **40** (2): 115-143. DOI: 10.1023/a:1006657515753

Hou, T.Y. and Wu, X.-H. 1997. A Multiscale Finite Element Method for Elliptic Problems in Composite Materials and Porous Media. *Journal of Computational Physics* **134** (1): 169-189. DOI: https://doi.org/10.1006/jcph.1997.5682

Hou, T.Y., Wu, X.-H., and Cai, Z. 1999. Convergence of a Multiscale Finite Element Method for Elliptic Problems with Rapidly Oscillating Coefficients. *Math. Comput.* **68** (227): 913-943. DOI: 10.1090/s0025-5718-99-01077-7

Hou, T.Y., Wu, X.-H., and Zhang, Y. 2004. Removing the Cell Resonance Error in the Multiscale Finite Element Method Via a Petrov-Galerkin Formulation. *Commun. Math. Sci.* **2** (2): 185-205.

Jenny, P., Lee, S.H., and Tchelepi, H.A. 2003. Multi-Scale Finite-Volume Method for Elliptic Problems in Subsurface Flow Simulation. *Journal of Computational Physics* **187** (1): 47-67. DOI: https://doi.org/10.1016/S0021-9991(03)00075-5

Jenny, P., Lee, S.H., and Tchelepi, H.A. 2005. Adaptive Multiscale Finite-Volume Method for Multiphase Flow and Transport in Porous Media. *Multiscale Modeling & Simulation* **3** (1): 50-64. DOI: https://doi.org/10.1137/030600795

Jenny, P. and Lunati, I. 2009. Modeling Complex Wells with the Multi-Scale Finite-Volume Method. *Journal of Computational Physics* **228** (3): 687-702. DOI: https://doi.org/10.1016/j.jcp.2008.09.026

Karimi‐Fard, M., Gong, B., and Durlofsky, L.J. 2006. Generation of Coarse‐Scale Continuum Flow Models from Detailed Fracture Characterizations. *Water resources research* **42** (10). DOI: https://doi.org/10.1029/2006WR005015

Kasap, E. and Lake, L.W. 1990. Calculating the Effective Permeability Tensor of a Gridblock. *SPE Formation Evaluation* **5** (02): 192-200. DOI: 10.2118/18434-PA

King, M.J. 2007. Upgridding and Upscaling: Current Trends and Future Directions. In: Society of Petroleum Engineers. DOI: 10.2118/112810-DL.

King, M.J., MacDonald, D.G., Todd, S.P. et al. 1998. Application of Novel Upscaling Approaches to the Magnus and Andrew Reservoirs.*European Petroleum Conference, The Hague, Netherlands*. Society of Petroleum Engineers. DOI: 10.2118/50643-MS.

King, M.J. and Mansfield, M. 1999. Flow Simulation of Geologic Models. *SPE Reservoir Evaluation & Engineering* **2** (04): 351-367. DOI: 10.2118/57469-PA

King, M.J., Wang, Z., and Datta-Gupta, A. 2016. Asymptotic Solutions of the Diffusivity Equation and Their Applications.*SPE Europec featured at 78th EAGE Conference and Exhibition, Vienna, Austria*. Society of Petroleum Engineers. DOI: 10.2118/180149-MS.

King, P.R. 1989. The Use of Renormalization for Calculating Effective Permeability. *Transport in Porous Media* **4** (1): 37-58. DOI: 10.1007/bf00134741

Kippe, V., Aarnes, J.E., and Lie, K.-A. 2008. A Comparison of Multiscale Methods for Elliptic Problems in Porous Media Flow. *Computational Geosciences* **12** (3): 377-398. DOI: 10.1007/s10596-007-9074-6

Krogstad, S., Lie, K.-A., Møyner, O. et al. 2015. Mrst-Ad – an Open-Source Framework for Rapid Prototyping and Evaluation of Reservoir Simulation Problems.*SPE Reservoir Simulation Symposium, Houston, Texas, USA*. Society of Petroleum Engineers. DOI: 10.2118/173317-MS.

Krogstad, S., Lie, K.-A., Nilsen, H.M. et al. 2009. A Multiscale Mixed Finite Element Solver for Three Phase Black Oil Flow.*SPE Reservoir Simulation Symposium, The Woodlands, Texas*. Society of Petroleum Engineers. DOI: 10.2118/118993-MS.

Kulkarni, K.N., Datta-Gupta, A., and Vasco, D.W. 2001. A Streamline Approach for Integrating Transient Pressure Data into High-Resolution Reservoir Models. *SPE Journal*. DOI: 10.2118/74135-PA

Künze, R. and Lunati, I. 2012. An Adaptive Multiscale Method for Density-Driven Instabilities. *Journal of Computational Physics* **231** (17): 5557-5570. DOI: https://doi.org/10.1016/j.jcp.2012.02.025

Lee, J. 1982. *Well Testing*: New York: Society of Petroleum Engineers. Original edition. ISBN 0895203170.

Lee, S.H., Wolfsteiner, C., and Tchelepi, H.A. 2008. Multiscale Finite-Volume Formulation for Multiphase Flow in Porous Media: Black Oil Formulation of Compressible, Three-Phase Flow with Gravity. *Computational Geosciences* **12** (3): 351-366. DOI: 10.1007/s10596-007-9069-3

Lie, K.-A. 2014. *An Introduction to Reservoir Simulation Using Matlab: User Guide for the Matlab Reservoir Simulation Toolbox (Mrst)*. Sintef Ict, Norway Original edition. ISBN.

Lie, K.-A., Krogstad, S., and Skaflestad, B. 2012. Mixed Multiscale Methods for Compressible Flow. In *ECMOR XIII-13th European Conference on the Mathematics of Oil Recovery*.ISBN 2214-4609.

Lie, K.-A., Møyner, O., Natvig, J.R. et al. 2017. Successful Application of Multiscale Methods in a Real Reservoir Simulator Environment. *Computational Geosciences* **21** (5): 981-998. DOI: 10.1007/s10596-017-9627-2

Lie, K.A., Krogstad, S., Ligaarden, I.S. et al. 2012. Open-Source Matlab Implementation of Consistent Discretisations on Complex Grids. *Computational Geosciences* **16** (2): 297-322. DOI: 10.1007/s10596-011-9244-4

Lunati, I., Bernard, D., Giudici, M. et al. 2001. A Numerical Comparison between Two Upscaling Techniques: Non-Local Inverse Based Scaling and Simplified Renormalization. *Advances in Water Resources* **24** (8): 913-929. DOI: https://doi.org/10.1016/S0309-1708(01)00008-2

Lunati, I. and Jenny, P. 2006. Multiscale Finite-Volume Method for Compressible Multiphase Flow in Porous Media. *Journal of Computational Physics* **216** (2): 616-636. DOI: https://doi.org/10.1016/j.jcp.2006.01.001

Lunati, I. and Jenny, P. 2008. Multiscale Finite-Volume Method for Density-Driven Flow in Porous Media. *Computational Geosciences* **12** (3): 337-350. DOI: 10.1007/s10596-007-9071-9

Lunati, I., Tyagi, M., and Lee, S.H. 2011. An Iterative Multiscale Finite Volume Algorithm Converging to the Exact Solution. *Journal of Computational Physics* **230** (5): 1849-1864. DOI: https://doi.org/10.1016/j.jcp.2010.11.036

Matthews, C.S., Brons, F., and Hazebroek, P. 1954. A Method for Determination of Average Pressure in a Bounded Reservoir. In: Society of Petroleum Engineers. DOI: 10.2118/296-G.

Møyner, O. and Lie, K.-A. 2014a. The Multiscale Finite-Volume Method on Stratigraphic Grids. *SPE Journal* **19** (05): 816-831. DOI: 10.2118/163649-PA

Møyner, O. and Lie, K.-A. 2014b. A Multiscale Two-Point Flux-Approximation Method. *J. Comput. Phys.* **275**: 273-293. DOI: 10.1016/j.jcp.2014.07.003

Møyner, O. and Lie, K.-A. 2016a. A Multiscale Restriction-Smoothed Basis Method for Compressible Black-Oil Models. *SPE Journal* **21** (06): 2079-2096. DOI: 10.2118/173265-PA

Møyner, O. and Lie, K.-A. 2016b. A Multiscale Restriction-Smoothed Basis Method for High Contrast Porous Media Represented on Unstructured Grids. *Journal of Computational Physics* **304**: 46-71. DOI: https://doi.org/10.1016/j.jcp.2015.10.010

Nunna, K. 2017. Application of Pressure Transient Concepts for Improved Upscaling of Geologic Models.*SPE Annual Technical Conference and Exhibition, San Antonio, Texas, USA*. 19. Society of Petroleum Engineers. DOI: 10.2118/189293-STU.

Nunna, K. and King, M.J. 2017. Dynamic Downscaling and Upscaling in High Contrast Systems.*SPE Reservoir Simulation Conference, Montgomery, Texas, USA*. Society of Petroleum Engineers. DOI: 10.2118/182689-MS.

Nunna, K., Liu, C., and King, M.J. 2018. Application of Diffuse Source Basis Functions to Multiscale Simulation. In *ECMOR XVI-16th European Conference on the Mathematics of Oil Recovery*.ISBN 2214-4609.

Nunna, K., Zhou, P., and King, M.J. 2015. Novel Diffuse Source Pressure Transient Upscaling.*SPE Reservoir Simulation Symposium, Houston, Texas, USA*. Society of Petroleum Engineers. DOI: 10.2118/173293-MS.

Nunna, K.C. 2014. Diffuse Source Transmissibility Upscaling. Master's Thesis, Texas A&M University. Available electronically from http : / /hdl .handle .net /1969 .1 /153898.

Pal, M., Lamine, S., Lie, K.A. et al. 2015. Validation of the Multiscale Mixed Finite ‐ Element Method. *International Journal for Numerical Methods in Fluids* **77** (4): 206-223. DOI: https://doi.org/10.1002/fld.3978

Peaceman, D.W. 1978. Interpretation of Well-Block Pressures in Numerical Reservoir Simulation(Includes Associated Paper 6988). *SPE Journal*. DOI: 10.2118/6893-PA

Peaceman, D.W. 1983. Interpretation of Well-Block Pressures in Numerical Reservoir Simulation with Nonsquare Grid Blocks and Anisotropic Permeability. *SPE Journal*. DOI: 10.2118/10528-PA

Peaceman, D.W. 1990. Interpretation of Wellblock Pressures in Numerical Reservoir Simulation: Part 3 -- Off-Center and Multiple Wells within a Wellblock. *SPE Reservoir Engineering* **5** (02): 227-232. DOI: 10.2118/16976-PA

Pedrosa, O.A., Jr. and Aziz, K. 1986. Use of a Hybrid Grid in Reservoir Simulation. *SPE Reservoir Engineering*. DOI: 10.2118/13507-PA

Raviart, P. and Thomas, J. 1977. A Mixed Finite Element Method for 2-Nd Order Elliptic Problems. *Mathematical aspects of finite element methods*: 292-315.

Rozon, B.J. 1989. A Generalized Finite Volume Discretization Method for Reservoir Simulation.*SPE Symposium on Reservoir Simulation, Houston, Texas*. 14. Society of Petroleum Engineers. DOI: 10.2118/18414-MS.

Sethian, J.A. 1996. A Fast Marching Level Set Method for Monotonically Advancing Fronts. *Proceedings of the National Academy of Sciences of the United States of America* **93** (4): 1591-1595.

Shah, S., Møyner, O., Tene, M. et al. 2016. The Multiscale Restriction Smoothed Basis Method for Fractured Porous Media (F-Msrsb). *Journal of Computational Physics* **318**: 36-57. DOI: https://doi.org/10.1016/j.jcp.2016.05.001

Shekhar, R., Sahni, I., Benson, G. et al. 2014. Modelling and Simulation of a Jurassic Carbonate Ramp Outcrop, Amellago, High Atlas Mountains, Morocco. *Petroleum Geoscience* **20** (1): 109-123. DOI: 10.1144/petgeo2013-010

Stewart, W. 1968. The Variational Method in Engineering, Rs Schechter, Mcgraw ‐ Hill, Inc., New York (1967), 287 Pages, $13.50. *AIChE Journal* **14** (3): 371-521.

Sun, J. and Schechter, D. 2015. Optimization-Based Unstructured Meshing Algorithms for Simulation of Hydraulically and Naturally Fractured Reservoirs with Variable Distribution of Fracture Aperture, Spacing, Length, and Strike. *SPE Reservoir Evaluation & Engineering* **18** (04): 463-480. DOI: 10.2118/170703-PA

Tchelepi, H.A., Jenny, P., Lee, S.H. et al. 2007. Adaptive Multiscale Finite-Volume Framework for Reservoir Simulation. *SPE Journal*. DOI: 10.2118/93395-PA

Vanek, P., Mandel, J., and Brezina, M. 1994. *Algebraic Multigrid on Unstructured Meshes*. University of Colorado at Denver.

Vasco, D. and Datta‐Gupta, A. 1999. Asymptotic Solutions for Solute Transport: A Formalism for Tracer Tomography. *Water Resources Research* **35** (1): 1-16. DOI: 10.1029/98WR02742

Virieux, J., Flores‐Luna, C., and Gibert, D. 1994. Asymptotic Theory for Diffusive Electromagnetic Imaging. *Geophysical Journal International* **119** (3): 857-868. DOI: 10.1029/98WR02742

Wang, Z., Li, C., and King, M. 2017. Validation and Extension of Asymptotic Solutions of Diffusivity Equation and Their Applications to Synthetic Cases.*SPE Reservoir Simulation Conference, Montgomery, Texas, USA*. Society of Petroleum Engineers. DOI: 10.2118/182716-MS.

Warren, J.E. and Price, H.S. 1961. Flow in Heterogeneous Porous Media. *SPE Journal* **1** (03): 153-169. DOI: 10.2118/1579-G

Watts, J.W. 1986. A Compositional Formulation of the Pressure and Saturation Equations. *SPE Journal*. DOI: 10.2118/12244-PA

Wen, X.-H., Durlofsky, L.J., and Chen, Y. 2006. Efficient 3d Implementation of Local-Global Upscaling for Reservoir Simulation. *SPE Journal*. DOI: 10.2118/92965-PA

Wen, X.H., Durlofsky, L.J., and Edwards, M.G. 2003. Use of Border Regions for Improved Permeability Upscaling. *Mathematical Geology* **35** (5): 521-547. DOI: 10.1023/a:1026230617943

White, C.D. and Horne, R.N. 1987. Computing Absolute Transmissibility in the Presence of Fine-Scale Heterogeneity.*SPE Symposium on Reservoir Simulation, San Antonio, Texas*. Society of Petroleum Engineers. DOI: 10.2118/16011-MS.

Wolfsteiner, C., Lee, S.H., and Tchelepi, H.A. 2006. Well Modeling in the Multiscale Finite Volume Method for Subsurface Flow Simulation. *Multiscale Modeling & Simulation* **5** (3): 900-917.

Wu, X.-H., Efendiev, Y., and Hou, T.Y. 2002. Analysis of Upscaling Absolute Permeability. *Discrete and Continuous Dynamical Systems Series B* **2** (2): 185-204. DOI: 10.3934/dcdsb.2002.2.185

Zhou, H. and Tchelepi, H.A. 2008. Operator-Based Multiscale Method for Compressible Flow. *SPE Journal* **13** (02): 267-273. DOI: 10.2118/106254-PA

Zhou, Y. and King, M.J. 2011. Improved Upscaling for Flow Simulation of Tight Gas Reservoir Models.*SPE Annual Technical Conference and Exhibition*, *Denver, Colorado, USA*. Society of Petroleum Engineers. DOI: 10.2118/147355-MS.